ISSN: 3023 -8951

CHAOS AND FRACTALS

VOLUME 3, ISSUE 1, JANUARY 2026

AN INTERDISCIPLINARY JOURNAL OF NONLINEAR SCIENCE

ADBA

https://journals.adbascientific.com/chf

ISSN: 3023-8951

Chaos and Fractals

Volume: 3 – Issue No: 1 (January 2026)

EDITORIAL BOARD

Editor-in-Chief

Dr. Akif Akgül, Hitit University, TURKIYE, akifakgul@hitit.edu.tr

Associate Editors

Dr. Miguel A.F. Sanjuán, Universidad Rey Juan Carlos, SPAIN, miguel.sanjuan@urjc.es
Dr. René Lozı, University Cote d'Azur, FRANCE, rene.lozi@univ-cotedazur.fr
Dr. Martin Bohner, Missouri University of Science and Technology, USA, bohner@mst.edu

Editorial Board Members

Dr. Esteban Tlelo-Cuautle, Instituto Nacional de Astrofísica, MEXICO, etlelo@inaoep.mx
Dr. Abdurrahim Toktas, Ankara University, TURKIYE, toktasa@ankara.edu.tr
Dr. Denis Butusov, Saint Petersburg State Electrotechnical University, RUSSIA, butusovdn@mail.ru
Dr. Ahmet Zengin, Sakarya University, TURKIYE, azengin@sakarya.edu.tr
Dr. Jun Ma, Lanzhou university of Technology, CHINA, hyperchaos@163.com
Dr. Yunus Babacan, Erzincan Binali Yıldırım University, TURKIYE, ybabacan@erzincan.edu.tr
Dr. Haris Skokos, University of Cape Town, SOUTH AFRICA, haris.skokos_at_uct.ac.za
Dr. Jordan Hristov, University of Chemical Technology and Metallurgy, BULGARIA, hristovmeister@gmail.com
Dr. Marcelo Messias, São Paulo State University, BRAZIL, marcelo.messias1@unesp.br
Dr. Jacques Kengne, Université de Dschang, CAMEROON, kengnemozart@yahoo.fr
Dr. Ugur Erkan, Ankara University, TURKIYE, ugurerkan@ankara.edu.tr
Dr. Jawad Ahmad, Prince Mohammad Bin Fahd University, SAUDI ARABIA, jawad.saj@gmail.com
Dr. Lazaros Moysis, University of Nova Gorica, SLOVENIA, lazaros.moysis@ung.si
Dr. Bilel Selmi, Université de Monastir, TUNISIA, bilel.selmi@fsm.rnu.tn
Dr. Suo Gao, Dalian Polytechnic University, CHINA, gaosuo@dlpu.edu.cn
Dr. Abdullah Yesil, Bandirma Onyedi Eylül University, TURKIYE, ayesil@bandirma.edu.tr

Editorial Advisory Board Members

Dr. Fatih Ozkaynak, Fırat University, TURKIYE, ozkaynak@firat.edu.tr
Dr. Buğra Bağcı, Hitit University, TURKIYE, bugrabagci@hitit.edu.tr
Dr. Haris Calgan, Balıkesir University, TURKIYE, haris.calgan@balikesir.edu.tr

Language Editor

Dr. Mustafa Kutlu, Sakarya University of Applied Sciences, TURKIYE, mkutlu@subu.edu.tr

Technical Coordinator

Dr. Murat Erhan Cimen, Sakarya University of Applied Sciences, TURKIYE, muratcimen@subu.edu.tr

https://journals.adbascientific.com/chf/about/editorialTeam

ISSN: 3023-8951

Chaos and Fractals

Volume: 3 – Issue No: 1 (January 2026)

CONTENTS

https://journals.adbascientific.com/chf/issue/view/16

ADBA Chaos and Fractals
Cutting-Edge Scientific Solutions

e-ISSN: 3023-8951
RESEARCH ARTICLE
Vol.3 / No.1 / 2026 / pp.1-6
https://doi.org/10.69882/adba.chf.2026011

A Study on Hindmarsh-Rose Neurons under an Electric Field

Vineetha Erathara Pious *,1 **and Stella Kooliath Antony** α,2

*Department of Physics, St. Xavier's College for Women, Aluva, Kerala, 683101, India, αDepartment of Chemistry, St. Xavier's College for Women, Aluva, Kerala, 683101, India.

ABSTRACT Today, we are at the heart of a great revolution brought about by emerging new ideas of chaos. The discovery of chaos has had a major impact on many fields of science, engineering, and mathematics. This phenomenon sheds new light on explaining the workings of the Earth's weather system, lasers, fluids, mechanical structures, earthquakes, etc. Understanding the brain and its behavior has been an active research field with various applications, including finding new solutions to cure brain diseases, designing better robots, and studying the behavior of neural networks. So far, various neural models have been developed. One such model is the Hindmarsh-Rose biological neuron model, which mimics the thalamic neurons of the brain. In this study, we analyzed the behavior of the Hindmarsh-Rose neurons under an electric field with a certain parameter. The Hindmarsh-Rose neuron model used here enables us to simulate how neurons behave in various situations, such as when they are exposed to electric fields. A program developed in MATLAB was used to perform simulations. Time response plots were obtained by varying parameters influencing the Hindmarsh-Rose neuron model. In this article, we look at how these factors change the way neurons act. Sometimes, they go from a steady firing pattern to more complex behavior, like oscillation death, which is shown by the simulations done in MATLAB software. From this article, one can understand how to improve a neural network for artificial intelligence. Additionally, how different external stimuli affect brain activity, which can lead to various neurological disorders.

KEYWORDS
Hindmarsh–Rose neuron model
Membrane potential
Synchronization
Quiescent
Coupled system

INTRODUCTION

Chaos and nonlinear dynamics have provided new theoretical and conceptual tools that allow us to capture, understand, and link together the surprisingly complex behaviors of simple systems (Hilborn 2000). The irregular and unpredictable time evolution of nonlinear systems may be termed Chaos (Baker and Gollub 1996). Chaotic behavior means erratic and almost random behavior, strongly influenced by outside noise or a system with many degrees of freedom, each doing its own thing. But these systems are deterministic. The key element in understanding this notion is nonlinearity, and the study of nonlinear behavior is nonlinear dynamics (Hilborn 2000). Many have become interested in chaos because (i) the study of chaos has provided new conceptual and theoretical tools enabling us to categorize and understand complex behavior that had confounded previous theories. (ii) Chaotic behavior seems to be universal (Hilborn 2000). The ability to transform chaotic behavior into periodic behavior would be advantageous in many day-to-day situations, such as the feasibility of using chaos control to stabilize periodic behavior from irregular heart-muscle activity (Walleczek 2000).

Manuscript received: 27 April 2025,
Revised: 12 August 2025,
Accepted: 2 September 2025.

[1]vineetha5568@gmail.com (**Corresponding author**)
[2]stellagrace2015@gmail.com

CHAOS IN THE BRAIN

In this section, we will familiarize ourselves with neurons, their functions, and all the information needed to realize a neuron model, especially the Hindmarsh-Rose neuron model.

Dynamics of a neuron

The primary building block of the central nervous system is called a neuron. The coordination between the brain and different organs is made possible with the help of these neurons through electrical impulses. Every time an input stimulus is given to a living body, the brain initiates a propagating change in the membrane potential, which brings out the response to the stimulus. This dynamic electrical excitation is called an action potential. They are characterized by sudden and transient changes of membrane potential that propagate to other neurons via a long extension called an axon.

The action potentials are created by the depolarization of the membrane (a sharp increase in the membrane potential), followed by repolarization (a slow decrease towards the resting potential). Since the action potential plays an important role in controlling the body and mind, efforts were taken to analyze its properties. The neurons are excitable because they are near a transition, called a bifurcation, from the resting phase to sustained spiking activity. Consider a neuron in its resting phase. In such a neuron, there are no changes in the membrane potential or any other state variables; hence, it is at an equilibrium point. The hyperpolarizing outward currents will balance all the inward currents, causing

depolarization. If the neurons remain quiescent despite all the small perturbations, we can conclude that the equilibrium point is stable. In the case of a neuron, small perturbations result in small departures from the equilibrium, denoted as PSP (postsynaptic potential). The neuron's intrinsic dynamics amplify larger perturbations and result in the spike response. If we inject a sufficiently strong current into the neuron, it exhibits periodic spiking activity (Izhikevich 2007).

Neuron model

The biological neuron model, also known as a spiking neuron model, is a mathematical description of the properties of certain cells within the systema nervosum that generate sharp electrical potentials across their cell wall (Gerstner *et al.* 2002). Neuron models are often divided into two categories consistent with the physical units of the model's interface.

Electrical input-output membrane voltage models – These models generate predictions of membrane output voltage as a function of electrical stimulation of the input stage (either voltage or current). The diverse models of this category differ from each other in the exact functional relationship between the input current and output voltage and the level of detail. This category includes models like the Hodgkin–Huxley model, FitzHugh–Nagumo model, Morris–Lecar model, and Hindmarsh–Rose model (Hodgkin and Huxley 1952).

Natural or pharmacological input neuron models – The models belonging to this category connect the input stimulus, which may be either pharmacological or natural, to the probability of a spike event. The input stage of those models isn't electrical but rather has either pharmacological (chemical) concentration units or physical units that characterize an external stimulus like light, sound, or other sorts of physical pressure. Moreover, the output stage portrays not an electrical voltage but the probability of a spike event.

Hindmarsh-Rose neuron model

The Hindmarsh-Rose (H-R) model for neurons was developed by J. L. Hindmarsh and R. M. Rose to study the rapid firing or bursting in neurons (Coombes *et al.* 2005; Thottil and Ignatius 2019). The Hindmarsh-Rose neuron model is a simplified model of the Hodgkin-Huxley model and a modification of the FitzHugh-Nagumo model. The HR model differs in many ways from the FHN model in terms of the topology of the phase space, threshold for spikes, the way the spike trains are created, and how bursting is shut off (Mustafa *et al.* 2013). The FitzHugh-Nagumo model simplified the Hodgkin-Huxley model for neurons, but it came with many drawbacks. The FHN model reduced the complexity of the neuron models, but bursting, which is one of the most essential characteristics of neurons, could not be observed. As this model consists of only a few parameters, it was difficult to adapt this model to neurons with specific properties. They do not give a reasonable frequency–current relationship (Hindmarsh and Rose 1982). This model could explain only the generation and propagation of action potentials with only the sodium and potassium channels. It also failed to explain the rhythm of the spike train. Therefore, more channels with slower kinetics have to be introduced to better understand the underlying mechanisms. Hence, the FHN model was modified to give the Hindmarsh-Rose model, which is a three-dimensional model for a neuron with rapid firing, bursting behavior, and chaos.

The H-R neuron model is aimed at studying the spiking-bursting behavior of the membrane potential of a single neuron. A chain of action potentials emitted by a single neuron is called a spike train; a sequence of stereotyped events that occur at regular or irregular intervals (Gerstner *et al.* 2002). The bursting behavior of the neurons, that is, the transition of a neuron from the resting phase to a recurring firing state, depends on the slow adaptation variable z(t) (Gerstner *et al.* 2002). Each burst will have a definite number of spikes unless they are in the chaotic region. In the H-R model, the relevant variable is the membrane potential x(t). There are two more variables, y(t) and z(t), that describe the transport of ions across membranes by ion channels. Therefore, the state of the system at any point in time is represented by the time-dependent state variables: x(t), y(t), and z(t). The Sodium and potassium ions are transported through fast ion channels, and their rate is measured by y(t), called the spiking variable (Hindmarsh and Rose 1984). The other ions are transported through slow channels, whose rate is measured by z(t), which is called the bursting variable (slow adaptation variable) (Hindmarsh and Rose 1984). The Hindmarsh–Rose model has the mathematical form of a system of three nonlinear ordinary differential equations with the dimensionless dynamic variables x(t), y(t), and z(t) (Hindmarsh and Rose 1984). These equations are as follows:

$$\begin{cases} \dot{x} &= y - ax^3 + bx^2 - z + I_{ext} \\ \dot{y} &= c - dx^2 - y \\ \dot{z} &= r(s(x - x_0))z \end{cases} \tag{1}$$

In these equations, x(t) represents the membrane potential, and y(t)and z(t) are recovery and adaptation variables, which account for fast and slow ion currents, respectively. 'I' represents the external stimuli or the applied current. We choose the parameters as a=1, b=3, c=1, d=5, r=0.006, and s=4 so that phenomena like bursting and spiking are observed (Storace *et al.* 2008). In the Hindmarsh-Rose model, the first two equations govern spiking.

The responses of this model to a current largely depend on the values of r and s. The slow parameter 'r' controls the speed of variation in the slow variable z(t). In the presence of spiking behavior, it governs the spiking frequency, whereas in the case of bursting, it determines the number of spikes per burst. 'x_0' is the resting potential of the system. The parameter "s" allows one to switch between the bursting and spiking behavior of the neurons and thus affects the qualitative behavior of the neurons (Storace *et al.* 2008). There are three modes of operation in the full Hindmarsh-Rose model: Quiescent, Spiking, and Bursting. The quiescent mode corresponds to the absence of stable cycles. Spiking means the continuous generation of action potentials, either regular or irregular. Bursting means that action potentials arrive in clear bursts at regular or irregular periods (Lange 2006).

Synchronization

Synchronization of chaos refers to a process where two or more chaotic systems (either equivalent or nonequivalent) adjust a given property of their motion to a common behavior due to a coupling or to a forcing (periodical or noisy) (Boccaletti *et al.* 2002). It is a complex, dynamic process and not a state. Chaotic systems are very sensitive to initial conditions and are difficult to predict. Chaotic systems with positive Lyapunov exponents resist synchronization. Two identical independent chaotic systems starting at nearly the same initial points quickly diverge with respect to time. When the Lyapunov exponents become negative, the systems start synchronizing (Boccaletti *et al.* 2002). If the trajectories of two chaotic systems are given by, say, 'x' and 'y', then they are said to be synchronized if x-y = 0.

Coupled Systems: Based on the way the coupling is done, unidirectional or bidirectional (mutual) coupling is possible. In the case of unidirectional coupling, a global system is formed by two sub-systems that realize a drive–response (or master-slave) configuration. This implies that one subsystem evolves freely and drives the evolution of the other (Boccaletti *et al.* 2002). Typical examples are communication with chaos. In bidirectional coupling, both subsystems are connected, and the coupling factor causes a synchronization of the rhythms between the systems. This situation typically occurs in nonlinear optics, e.g., coupled laser systems with feedback (Boccaletti *et al.* 2002). In other words, when the evolution of one of the coupled systems is unaltered by the coupling, the resulting configuration is called unidirectional coupling or drive–response coupling. Conversely, bidirectional coupling takes place when both systems are linked in a manner that results in them impacting each other's behavior.

Different types of synchronization: Complete synchronization- Coupled identical systems display complete synchronization with a strong coupling strength. Here, the synchronization appears as the equality of the state variables while evolving in time. It is also known as identical or conventional synchronization (Pyragas 1996). It was first discovered and is the simplest form of synchronization in chaotic systems. This mechanism was first shown to occur when two identical chaotic systems are coupled unidirectionally, provided that the conditional Lyapunov exponents of the subsystem to be synchronized are all negative (Boccaletti *et al.* 2002).

Generalized synchronization- This type of synchronization is observed when the coupled systems are completely different. The driven (slave) and the driving (master) systems can be represented by a one-to-one mapping given by y(t)=x(t). Thus, y(t) can be determined if the evolution of the drive system is known. Once the two systems get synchronized, the difference in trajectories, with respect to time, reduces to zero (Boccaletti *et al.* 2002).

Phase synchronization- This was first observed in the Rössler system and can be simulated by a very weak external force. If m and n are integers and α and β represent the phases belonging to two different systems, then m*α-n*β=C, where C is a constant, representing the phase synchronization relationship between the two systems. This means that phase synchronization occurs when either the phases change in the same way or a constant ratio exists between the two systems. So, perfect phase synchronization between two coupled oscillators will occur when the chaotic oscillators are phase coherent. It is achieved at very low coupling strengths (Boccaletti *et al.* 2002).

Lag synchronization- It is displayed by non-identical systems with a larger coupling strength. Lag synchronization lies between phase synchronization and complete synchronization. In lag synchronization, the states of two oscillators are nearly identical, but one system lags in time behind the other. With a slight increase in the coupling strength, complete synchronization can be achieved (Boccaletti *et al.* 2002).

Anti-synchronization- It occurs when the state variables of both the driving and driven systems are the same in magnitude but opposite in sign. In this case, the relationship between the slave, y (t), and the master, x(t) (Boccaletti *et al.* 2002), is given by y (t) = -(x (t)).

DYNAMICS OF HINDMARSH-ROSE MODEL

Electrical activities in the H-R neuron under an Electric field

A neuron contains many charged ions such as calcium, potassium, and sodium. Some of these ions are transported within the cell, while others pass through the membrane channel to form transmembrane currents. As a result, fluctuation of membrane potential occurs, and the membrane can be regarded as a charged surface with a certain uniform distribution of charges because charged ions continue to supply the flow of current (Ma *et al.* 2018).

Therefore, the surface of the cell or the membrane can be considered as a large plate with charges, and thus an electric field is induced. Suppose that the membrane holds size S, charge number q, surface charge density σ (=q/S), then the intensity of the electric field close to the membrane (Ma *et al.* 2018) can be calculated by:

$$E = \frac{q}{2\varepsilon_1 S} = \frac{\sigma}{2\varepsilon_1} \tag{2}$$

$$\Delta V = k_1 E = E\sqrt{S} \tag{3}$$

where parameter ε_1 denotes the dielectric constant which is associated with the intrinsic property of the media, k_1 is the radius size when the cell is regarded as a ball shape, and ΔV represents the voltage between plates or the membrane potential of the cell. A biological neuron model should consider the effect of ion channels, which decide the propagation of ions and the membrane potential as well (Ma *et al.* 2018). However, the involvement of field variable E can well describe the distribution of ions and the change of membrane potential induced by the exchange and transport of ions in the cell (Ma *et al.* 2018).

Therefore, an electric field can be used as a new variable to estimate the change in the membrane potential of the neuron. The improved four-variable Hindmarsh–Rose neuron model can be built, including the effect of electric field as follows:

$$\begin{cases} \frac{dx_1}{dt} &= x_2 - ax_1^3 + bx_1^2 - x_3 + I_{\text{ext}} \\ \frac{dx_2}{dt} &= c - dx_1^2 - x_2 + k_1 E \\ \frac{dx_3}{dt} &= r(s(x_1 - x_0) - x_3) \\ \frac{dE}{dt} &= k_2 x_2 + E_{\text{ext}} \end{cases} \tag{4}$$

The variables x_1, x_2, and x_3 describe the membrane potential, the recovery variable for fast currents associated with potassium and sodium ions, and the adaptation current dependent on the slow current for calcium ions, respectively. Therefore, the effect of the electric field is considered by adding k_1E to modulate the second variable y, rather than the third variable z, because the fast current is sensitive to the change of polarized and induced electric field. E_{ext} represents the external electric field, which can be a periodical modulation or noise-like radiation as well. k_2 is a constant that describes the polarization, and $I_{ext}$is the external forcing current.

Simulation results of the H-R neuron under an Electric field

Time series behavior under external non-periodic current: A variety of modes in electrical activities can be triggered by varying the external non-periodic field as I_{ext}=0.5mA, 3mA, 26mA, respectively, and the parameter values chosen as a=1, b=3, c=1, d=5, r=0.006, s=4, x_0=-1.6, k_1=0.0001, k_2=15, E=0.5. Here, the external electric field E_{ext} is taken to be a periodical modulation, given by $E_{ext} = B_1\sin(\omega_1 t) + B_2\cos(\omega_2 t)$, where B_1, B_2 are the intensities while ω_1, ω_2 are the angular frequencies of the external electric field, respectively.

Time series behavior under external periodic current: Different electric modes of time series of the membrane potential of a neuron due to external periodic current are obtained by applying a periodic current I_{ext}=ASin(ωt). The parameter values are selected as

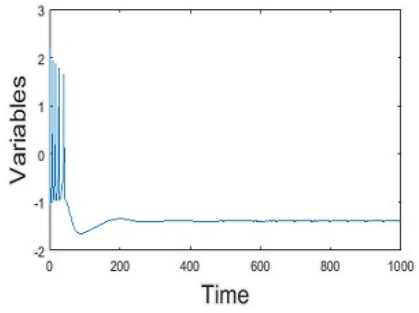

(a)

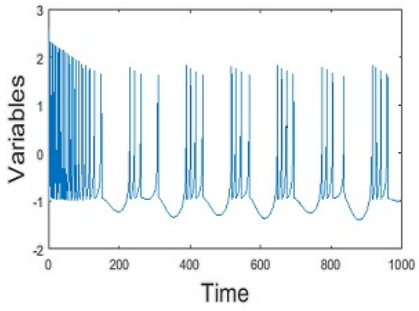

(b)

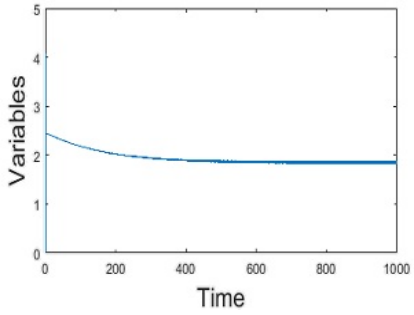

(c)

Figure 1 Time series for membrane potential x_1 are shown at different non-periodic currents (a)I_{ext}=0.5mA (b)I_{ext}=3mA, and (c)I_{ext}=26mA. The quiescent states for the spiking activities are observed at a very low external current (I_{ext}=0.5mA). As we increase I_{ext} to 3mA, we can see the periodic bursting behavior of the neuron. The system settles down to oscillation suppression only after applying a very high external current.

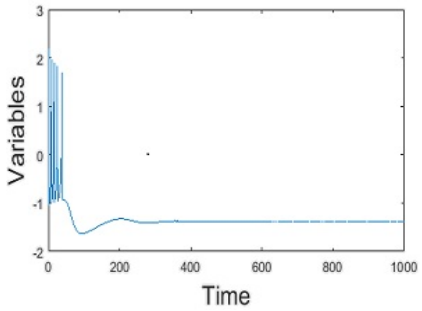

(a)

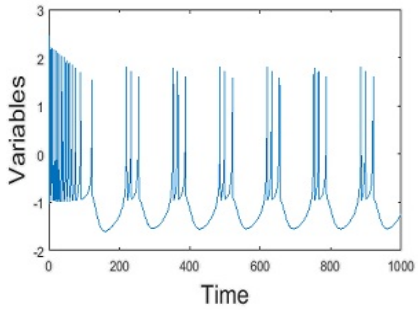

(b)

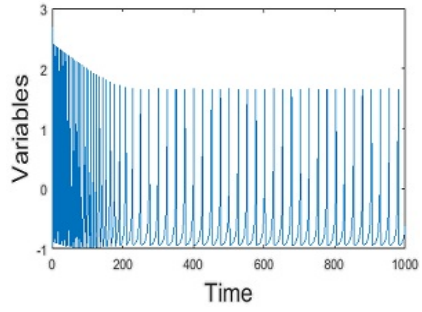

(c)

Figure 2 Influence of periodic current on membrane potential is shown in figure for (a) A =7, ω=0.15, (b) A =15, ω=0.15, and (c) A=25, ω=0.15, respectively. From the figure, the quiescent states in the first figure change to quiescent states with sustained bursting along with an increase in the periodic current (A = 15, ω= 0.15). The quiescent states change to tonic spiking as the amplitude of the external periodic current is very high (A=25, ω =0.15).

a=1, b=3, c=1, d=5, r=0.006, s=4, x_0=-1.6, k_1=0.0001, k_2=15, E=0.5, B_1=50, B_2=0.5, ω_1=5.5, ω_2=3.5 and t=1. Here, the different modes are obtained by varying the amplitude of the current while the angular frequency is fixed.

Electrical activities in a Synchronized H-R neuron under an Electric field and noise

$$\begin{cases} \frac{dx_1}{dt} &= x_2 - ax_1^3 + bx_1^2 - x_3 + I_{\text{ext}} + g(x_5 - x_1) \\ \frac{dx_2}{dt} &= c - dx_1^2 - x_2 + k_1 E \\ \frac{dx_3}{dt} &= r(s(x_1 - x_0) - x_3) \\ \frac{dE}{dt} &= k_2 x_2 + E_{\text{ext}} \end{cases} \tag{5}$$

$$\begin{cases} \frac{dx_4}{dt} &= x_6 - ax_5^3 + bx_5^2 - x_7 + I_{\text{ext}} + g(x_1 - x_5) \\ \frac{dx_5}{dt} &= c - dx_5^2 - x_6 + k_1 E \\ \frac{dx_6}{dt} &= r(s(x_5 - x_0) - x_7) \\ \frac{dE}{dt} &= k_2 x_6 + E_{\text{ext}} \end{cases} \tag{6}$$

Where x_1, x_2, and x_3 represent the membrane potential, slow current, and adaptation current of the first neuron, respectively. Similarly, x_4, x_5, and x_6 represent the corresponding variables of the second neuron. I_{ext} is the external forcing current. The parameter values are selected as a = 1, b =3, c =1, d =5, r =0.006, s =4, x_0 =-1.6. The term g represents the coupling intensity between the neurons (Pyragas 1996). k_1 is the radius size, E_{ext} is the external

electrical field, and k_2 describes the polarization.

Simulation results of the Synchronized H-R neuron under an Electric field and noise

Time series behavior under the Electric field: Time series for membrane potentials for the two coupled neurons for different external forcing currents, (a) I_{ext}=1.5mA, (b) I_{ext}=3mA, and (c) I_{ext}=5mA.

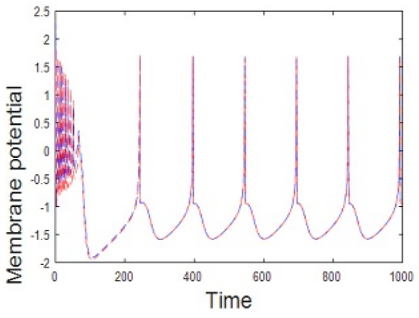

(a)

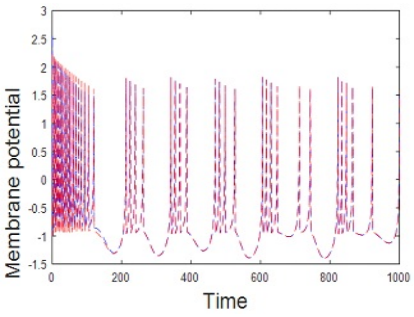

(b)

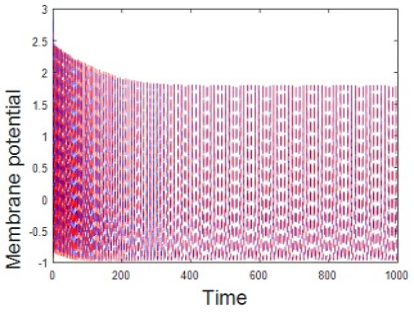

(c)

Figure 3 Here the parameter values are selected as k_1=0.0001, k_2=15, E=0.5, B_1=50, B_2=0.5, ω_1=5.5, ω_2=3.5, t=1 and g = 1. When I_{ext}=1.5mA, the system exhibits a periodic behavior. Also, when the external forcing current is set as I_{ext}=3 mA, chaotic synchronization is observed. A transition from chaotic to tonic synchronization states is observed when the external periodic current increases to I_{ext}=5mA.

Time series behavior under the noise: Similarly, we applied an external electric field, E_{ext}=ξ(t) as a noise-like disturbance, where ξ(t) is the Gaussian white noise. By keeping the external forcing current fixed, say I_{ext}=5mA, and changing the intensity of noise as (a) D=5 and (b) D=25, different states of the neurons are observed.

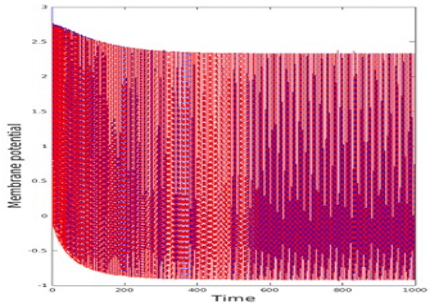

(a)

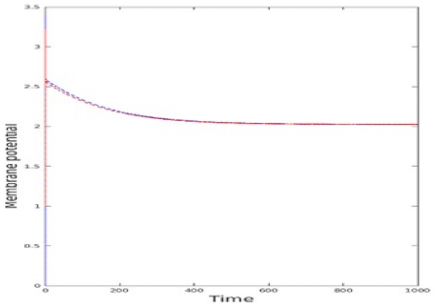

(b)

Figure 4 Time series for membrane potentials are plotted for fixed external forcing current (I_{ext}=5 mA) for different noise parameters (a) g=1, D=5 and (b) g=1, D=25. At I_{ext}=5mA, the system shows a tonic behavior even if the external electric field is either a periodic modulation or noise-like radiation. But as we increase the noise intensity to a very high value, say D=25, the system changes its state from tonic to that of oscillation death.

CONCLUSION

The human brain is made up of billions of neurons that communicate with each other through chemical and electrical synapses. Neurons exhibit varying firing patterns, including spiking, bursting, chaotic firing, and a combination of these patterns. Once two neurons are coupled, their dynamics become complex and display different forms of synchronization, amplitude death, oscillation death, and near-death-like spikes (Resmi *et al.* 2011). Here, we studied the Hindmarsh-Rose (H-R) model under an electric field. A detailed study of the Hindmarsh-Rose model for neurons is done with the help of MATLAB software. In the first part, we analyzed the different modes of electrical activities of the membrane potential in a single neuron under the external electric field term. The system behavior is studied under the influence of external periodic and non-periodic currents. It is observed that for a non-periodic current, as the value of the external current increases, the quiescent states become broadened, and for higher values of external current, the system settles down to an oscillation death state. Nevertheless, in the case of the periodic current, the action potential shows enhanced quiescent states for the spiking activities. In the higher current, the neuron exhibits tonic oscillations in contrast to the suppression of activities observed in the non-periodic case.

The focal point of the study also includes the synchronization of coupled neurons. Under the influence of the electric field, the system changes through periodic-, chaotic-, and tonic-type synchronization as the current is increased. Also, from the introduction of control parameters like noise on the neurons, it is found

that when the noise factor is applied to the system, the oscillation death is achieved for a smaller magnitude of external current. This highlights a crucial aspect of neurophysiological resilience and flexibility. The ability of the electric field generated by the brain to influence its activity appears to be particularly notable during epileptic seizures. However, the effect of an electric field is not limited to these pathological conditions. The study by Frohlich and McCormick demonstrates that the electrical fields also influence brain function during normal activities such as sleep. Studies based on biological models also have high potential for developing clinical treatment modes for diseases such as Alzheimer's. The detailed study of the dynamical behaviors of single and coupled neurons helps in comprehending higher functions of the brain, like perception, episodic memory, learning, awareness, etc. The observations made in the study might point to new means of curing disorders resulting from irregular neuronal synchronization, such as epilepsy and other neurodegenerative conditions. Future work may explore the influence of electric fields on synaptic behavior. One may also investigate the effects of these influences on different neural circuits that control higher cognitive functions. An understanding of these interactions may lead to new methods to enhance cognitive abilities and address many of the neurological disorders, in addition to the more effective linkage of theoretical models to practical applications in neuroscience.

Ethical standard

The authors have no relevant financial or non-financial interests to disclose.

Availability of data and material

Not applicable.

Conflicts of interest

The authors declare that there is no conflict of interest regarding the publication of this paper.

LITERATURE CITED

Baker, G. and J. Gollub, 1996 *Chaotic Dynamics: An Introduction*. Cambridge University Press.

Boccaletti, S., J. Kurths, G. Osipov, D. Valladares, and C. Zhou, 2002 The synchronization of chaotic systems. Physics Reports **366**: 1–101.

Coombes, S., P. Bressloff, and eds, 2005 *Bursting: The Genesis of Rhythm in the Nervous System*. World Scientific.

Gerstner, W., Wulfram, Kistler, and W. M., 2002 *Spiking Neuron Models: Single Neurons, Populations, Plasticity*. Cambridge University Press.

Hilborn, R. C., 2000 *Chaos and Nonlinear Dynamics: An Introduction for Scientists and Engineers*. Oxford University Press.

Hindmarsh, J. and R. Rose, 1982 A model of the nerve impulse using two first-order differential equations. Nature **296**: 162–4.

Hindmarsh, J. and R. Rose, 1984 A model of neuronal bursting using three coupled first-order differential equations. Proc R Soc Lond B Biol Sci. **221**: 87–102.

Hodgkin, A. and A. Huxley, 1952 A quantitative description of membrane current and its application to conduction and excitation in nerve. J Physiol **117**: 500–44.

Izhikevich, E., 2007 *Dynamical Systems in Neuroscience*. Computational neuroscience, Dynamical systems in neuroscience, MIT Press.

Lange, E., 2006 Neuron models of the generic bifurcation type: network analysis and data modeling .

Ma, J., G. Zhang, T. Hayat, and et al., 2018 Model electrical activity of neuron under electric field. Nonlinear Dyn **95**: 1585—1598.

Mustafa, M., W. K. Putra, and K. Agus, 2013 Development of dynamics and synchronization model for coupled neurons using hindmarsh-rose model. Applied mathematical sciences **7**: 135–152.

Pyragas, K., 1996 Weak and strong synchronization of chaos. Phys. Rev. E **54**: R4508–R4511.

Resmi, V., G. Ambika, and R. E. Amritkar, 2011 General mechanism for amplitude death in coupled systems. Phys. Rev. E **84**: 046212.

Storace, M., D. Linaro, and E. de Lange, 2008 The hindmarsh–rose neuron model: Bifurcation analysis and piecewise-linear approximations. Chaos: An Interdisciplinary Journal of Nonlinear Science **18**: 033128.

Thottil, S. K. and R. P. Ignatius, 2019 Influence of memristor and noise on h–r neurons. Nonlinear Dyn 95 pp. 239–257.

Walleczek, J., 2000 *Self-Organized Biological Dynamics and Nonlinear Control: Toward Understanding Complexity, Chaos and Emergent Function in Living Systems*. Cambridge University Press.

How to cite this article: Pious, V.E., and Antony, S.K. A Study on Hindmarsh-Rose Neurons under an Electric Field. *Chaos and Fractals*, 3(1), 1-6, 2026.

Licensing Policy: The published articles in CHF are licensed under a Creative Commons Attribution-NonCommercial 4.0 International License.

ADBA Chaos and Fractals
Cutting-Edge Scientific Solutions

e-ISSN: 3023-8951
RESEARCH ARTICLE
Vol.3 / No.1 / 2026 / pp.7-15
https://doi.org/10.69882/adba.chf.2026012

Design and Performance Evaluation of a Hybrid PRNG: Gold-SA II Optimized LFSR Combined with Discrete Chaotic Maps

Eyüp Eröz [*,1], **Erkan Tanyıldızı** [α,2] **and Fatih Özkaynak** [α,3]

*Firat University, Kovancilar Vocational School Department of Computer Technologies, Elazig, Türkiye, αFirat University, Department of Software Engineering, Elazig, Türkiye.

ABSTRACT Random Number Generators (RNGs) play a critical role in ensuring data security in cryptographic systems. Linear Feedback Shift Registers (LFSRs) are widely used due to their hardware speeds and low costs; however, their linear structures make them vulnerable to algebraic attacks and may yield insufficient results in statistical randomness tests. This study proposes a hybrid architecture based on optimisation and chaos to enhance the cryptographic security of LFSR-based generators. The irreducible polynomials and initial seed values that provide the maximum period length of the LFSR have been optimised using the Modified Golden Sine Algorithm (Gold-SA II). As the raw LFSR outputs failed the NIST SP 800-22 tests, the system was supported by a chaotic final processing layer containing Sine, Chebyshev, Logistic, Tent, and Circle maps. Experimental results demonstrate that the chaotic final processing significantly improves randomness properties and, in particular, that the Sinus map-based structure successfully passes all NIST tests.

KEYWORDS
LFSR
Gold-SA II
Chaotic maps
Hybrid PRNG
NIST SP 800-22
Cryptography

INTRODUCTION

In the rapidly evolving digital landscape, the volume of data transmitted and stored within critical infrastructures such as the Internet of Things (IoT), cloud computing platforms, and military communication systems is increasing exponentially. Ensuring the confidentiality and integrity of this data against unauthorized access has therefore become a primary strategic objective in information security. The security of modern cryptographic systems depends not only on the computational strength of encryption algorithms but also, fundamentally, on the quality of the cryptographic keys employed. In this context, Random Number Generators (RNGs) play a crucial role by producing encryption keys, initialization vectors (IVs), and nonces. Consequently, the unpredictability and statistical randomness of the sequences generated by an RNG directly determine the overall security of the cryptographic chain (Rukhin *et al.* 2010).

Among various RNG architectures, Linear Feedback Shift Registers (LFSRs) are widely adopted in hardware-oriented applications due to their low power consumption, high generation speed, and structural simplicity (Golomb 1982). However, the cryptographic suitability of LFSR-based systems strongly depends on their initial configuration, particularly the choice of the feedback polynomial and the seed value. As the polynomial degree increases, identifying primitive polynomials and suitable seeds that ensure a maximum period length of $2^n - 1$ becomes computationally intractable. Moreover, even when maximum-length configurations are employed, the inherent linearity of LFSRs renders them vulnerable to algebraic attacks and often results in poor performance in stringent statistical randomness test suites.

To address these challenges, extensive research efforts have been reported in the literature focusing on chaotic systems and optimization algorithms. Silva *et al.* (2009) proposed a modular-chaos pseudo-random number generator (PRNG) based on the Lorenz system, demonstrating that chaos-based approaches can provide strong resistance against statistical attacks. Similarly, Murillo-Escobar *et al.* (2017) and Moysis *et al.* (2020) investigated the enhancement of randomness properties in logistic-map-based generators for cryptographic applications.

From an optimization perspective, Tanyildizi and Ozkaynak (2019) employed multiple optimization algorithms to determine optimal initial parameters for S-box generation. Recently, Eröz *et al.* (2025) proposed the COLFSR architecture, demonstrating that integrating chaos optimization with LFSR structures significantly enhances the statistical randomness of the generated sequences, while Demidova *et al.* (2020) utilized optimization techniques to improve the statistical characteristics of generated random se-

Manuscript received: 4 December 2025,
Revised: 13 January 2026,
Accepted: 17 January 2026.

[1]eeroz@firat.edu.tr (**Corresponding author**)
[2]etanyildizi@firat.edu.tr
[3]ozkaynak@firat.edu.tr

quences. Furthermore, recent studies such as Muhammad and Ozkaynak (2021) explored multi-stage encryption frameworks involving chaotic selection mechanisms, emphasizing the importance of careful system design to mitigate temporal correlations. Emin *et al.* (2024) demonstrated the effectiveness of chaotic systems in secure image encryption applications Abdulrazaq *et al.* (2024) proposed a synergistic framework for constructing high-performance S-boxes based on chaotic systems, demonstrating that chaos-driven designs can significantly enhance cryptographic security metrics and represent a paradigm shift in modern cryptographic security architectures. Similarly, Zhao *et al.* (2024) focused on improving complexity in chaotic maps to improve dynamic behaviors.

Recent studies have increasingly focused on hybrid structures to overcome the limitations of standalone chaotic maps. For instance, Youssef (2024) demonstrated the efficacy of hyperchaotic systems in satellite image security, utilizing dynamic S-boxes to enhance encryption robustness. Similarly, Zhao *et al.* (2024) explored complexity enhancement techniques to expand the grid basin of chaotic attractors. Building on these contemporary approaches, our study integrates the structural simplicity of LFSRs with the complexity of chaotic maps, as also compared against recent works like Guo *et al.* (2023) in the experimental results section. Despite the notable advancements achieved in these studies, optimization-based parameter selection and chaotic post-processing are typically treated as independent enhancement strategies. In this study, a novel hybrid PRNG architecture is proposed to bridge this gap by synergistically combining both approaches. Specifically, an LFSR optimized using the Modified Golden Sine Algorithm (GoldSA II), which exhibits insufficient statistical randomness in its raw output, is reinforced through chaotic post-processing.

A comparative evaluation is conducted using five distinct chaotic maps, namely the Sine, Chebyshev, Logistic, Tent, and Circle maps. The primary objectives of the proposed architecture are threefold: (i) to disrupt the inherent linear structure of the LFSR, (ii) to maximize the success rate in the NIST SP 800–22 statistical test suite, and (iii) to identify the chaotic map that achieves the most favorable trade-off between generation speed and cryptographic security. Experimental results indicate that, while the standalone optimized LFSR fails several critical randomness tests, the proposed hybrid architecture particularly when combined with the Sine map successfully passes all tests in the NIST SP 800–22 suite. This section presents the mathematical foundations of the components utilized in the proposed system and provides a detailed description of the architecture of the hybrid pseudo-random number generator.

MATERIALS AND METHODS

This section describes the materials, mathematical models, and methodological framework employed in the design, implementation, and evaluation of the proposed hybrid pseudo-random number generator (PRNG). The methodology is based on integrating an optimized Linear Feedback Shift Register (LFSR) structure with a chaotic post-processing mechanism in order to enhance cryptographic randomness and security. The overall approach includes the selection and optimization of LFSR parameters, the application of chaotic maps to disrupt linear dependencies, and the comprehensive evaluation of the generated sequences using statistical randomness tests and performance metrics. Details regarding the system components, optimization strategy, chaotic processing, experimental setup, and evaluation criteria are presented to ensure the reproducibility and reliability of the proposed method.

Linear Feedback Shift Registers (LFSR)

In stream cipher applications, one of the most commonly used random number generators is the Linear Feedback Shift Register (LFSR), which consists of a set of flip-flops (one-bit storage elements) and a feedback path. The number of flip-flops determines the degree of the LFSR. In other words, an LFSR composed of m flip-flops has a degree of m. The feedback path computes the input of the last flip-flop as the exclusive-OR (XOR) sum of selected flip-flop outputs. A simple LFSR structure of degree three is illustrated in Figure 1 (Kumar *et al.* 2017; Bagalkoti *et al.* 2019).

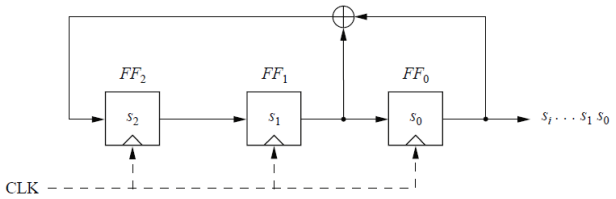

Figure 1 General structure of a degree-3 LFSR.

In Figure 1, FF_0, FF_1, and FF_2 denote the flip-flops of the LFSR, while the variables s_i represent the internal state bits. The rightmost state bit is considered the current output bit of the generator. The leftmost state bit corresponds to the output of the XOR summation computed in the previous iteration, and at each clock cycle, all state bits are shifted one position to the right. Since the feedback operation is based on the XOR function, which is a linear operation, such structures are referred to as Linear Feedback Shift Registers (LFSRs).

Mathematical Representation The general structure of an LFSR with degree m is shown in Figure 2.2. This structure consists of m flip-flops and m possible feedback tap positions, all combined through XOR operations. The activation of each feedback tap is defined by the feedback coefficients $p_0, p_1, \ldots, p_{m-1}$. If $p_i = 1$, the corresponding feedback tap is active (closed switch), whereas if $p_i = 0$, the output of the associated flip-flop is excluded from the feedback path (open switch).

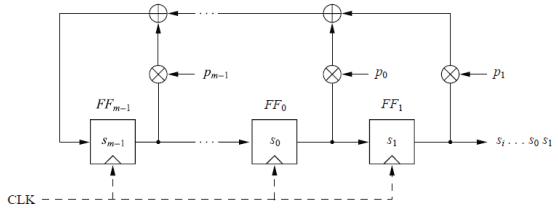

Figure 2 General structure of an LFSR of degree m.

Using this representation, the feedback path can be expressed in a simple mathematical form. The output of the i-th flip-flop is multiplied by the coefficient p_i, resulting either in the flip-flop output when $p_i = 1$ or zero when $p_i = 0$. The values of these feedback coefficients play a critical role in determining the characteristics of the output sequence generated by the LFSR.

Here, the number of flip-flops m represents the degree of the LFSR, the coefficients p_i correspond to the polynomial coefficients, and the variables s_i denote the internal state bits. As shown in Figure 2.2, the flip-flops initially take the values $s_0, \ldots, s_{m-1}$. Based on the feedback coefficients $p_0, p_1, \ldots, p_{m-1}$, the output bit s_m is obtained by applying the XOR operation to the outputs of the

flip-flops for which $p_i = 1$. This bit is then fed as the input to the leftmost flip-flop in the next iteration. The LFSR continues this process until the sequence reaches its maximum period length (Paar and Paar 2010).

The mathematical expression describing the operation of an LFSR is given as follows. Let the initial internal states be $s_0, \ldots, s_{m-1}$. The feedback bit s_{i+m}, which serves as the input to the leftmost flip-flop, is computed as the XOR sum of the products of the flip-flop outputs and their corresponding feedback coefficients. This relationship is expressed in Eq. (1).

$$s_{i+m} \equiv \sum_{j=0}^{m-1} p_j s_{i+j} \pmod 2 \tag{1}$$

LFSRs are sometimes referred to as linear recurrences in the literature. Due to the finite number of internal states, the generated output sequence eventually becomes periodic. Depending on the number of flip-flops and the selected feedback coefficients, an LFSR can produce output sequences with different period lengths. For an LFSR of degree m, the maximum achievable period length is $2^m - 1$. However, only specific combinations of feedback coefficients can generate sequences with maximum length (Paar and Paar 2010).

Examples **Example 1:** For a maximum-length LFSR with $m = 5$ and feedback coefficients $(p_4 = 1, p_3 = 0, p_2 = 1, p_1 = 0, p_0 = 1)$, a sequence of length 31 bits is generated, corresponding to the maximum period of $2^m - 1$.

Example 2: For another LFSR configuration with $m = 5$ but different feedback coefficients, a sequence of length 28 bits is generated, indicating that the maximum period length is not achieved with this combination.

According to the literature, in order for an LFSR to generate a maximum-length sequence, the corresponding feedback polynomial must be irreducible (Park and Miller 1988). In this context, the polynomial represents the indices of the activated flip-flops. For an LFSR with feedback coefficients $p_{m-1}, \ldots, p_1, p_0$, the characteristic polynomial is defined as Eq. (2).

$$P(x) = x^m + p_{m-1}x^{m-1} + \cdots + p_1 x + p_0. \tag{2}$$

For example, an LFSR with coefficients $(p_4 = 1, p_3 = 0, p_2 = 1, p_1 = 0, p_0 = 1)$ can be equivalently represented by the polynomial $x^5 + x^3 + 1$. LFSRs that achieve maximum-length sequences correspond to primitive polynomials. Figure 2.3 presents irreducible polynomials for values of m in the range $1 \leq m \leq 128$.

Parameter Optimization Using the Gold-SA II Algorithm

The Modified Golden Sine Algorithm (Gold-SA II) is an optimization technique inspired by the mathematical properties of the sine function and the golden ratio. The fundamental concept of the algorithm is based on the idea that the continuous traversal of the unit circle by the sine function can be conceptually mapped to the exploration of an optimization search space (Mirjalili and Lewis 2016; Tanyildizi 2018). By associating one full rotation of the unit circle with a complete search cycle, the algorithm enables systematic exploration of candidate solutions.

The time-domain representation of the sine waveform and its corresponding phasor illustration are shown in Figure 2.4. Considering 2π radians as a full cycle, the sine function scans the entire unit circle with constant angular frequency and radius. The mathematical expression of the sine wave utilized in the Gold-SA II algorithm is given in Eq. 3.

$$V(t) = A\sin(\omega t), \tag{3}$$

(0,1,2)	(0,1,3,4,24)	(0,1,46)	(0,1,5,7,68)	(0,2,3,5,90)	(0,3,4,5,112)
(0,1,3)	(0,3,25)	(0,5,47)	(0,2,5,6,69)	(0,1,5,8,91)	(0,2,3,5,113)
(0,1,4)	(0,1,3,4,26)	(0,2,3,5,48)	(0,1,3,5,70)	(0,2,5,6,92)	(0,2,3,5,114)
(0,2,5)	(0,1,2,5,27)	(0,4,5,6,49)	(0,1,3,5,71)	(0,2,93)	(0,5,7,8,115)
(0,1,6)	(0,1,28)	(0,2,3,4,50)	(0,3,9,10,72)	(0,1,5,6,94)	(0,1,2,4,116)
(0,1,7)	(0,2,29)	(0,1,3,6,51)	(0,2,3,4,73)	(0,11,95)	(0,1,2,5,117)
(0,1,3,4,8)	(0,1,30)	(0,3,52)	(0,1,2,6,74)	(0,6,9,10,96)	(0,2,5,6,118)
(0,1,9)	(0,3,31)	(0,1,2,6,53)	(0,1,3,6,75)	(0,6,97)	(0,8,119)
(0,3,10)	(0,2,3,7,32)	(0,3,6,8,54)	(0,2,4,5,76)	(0,3,4,7,98)	(0,1,3,4,120)
(0,2,11)	(0,1,3,6,33)	(0,1,2,6,55)	(0,2,5,6,77)	(0,1,3,6,99)	(0,1,5,8,121)
(0,3,12)	(0,1,3,4,34)	(0,2,4,7,56)	(0,1,2,7,78)	(0,2,5,6,100)	(0,1,2,6,122)
(0,1,3,4,13)	(0,2,35)	(0,4,57)	(0,2,3,4,79)	(0,1,6,7,101)	(0,2,123)
(0,5,14)	(0,2,4,5,36)	(0,1,5,6,58)	(0,2,4,9,80)	(0,3,5,6,102)	(0,37,124)
(0,1,15)	(0,1,4,6,37)	(0,2,4,7,59)	(0,4,81)	(0,9,103)	(0,5,6,7,125)
(0,1,3,5,16)	(0,1,5,6,38)	(0,1,60)	(0,4,6,9,82)	(0,1,3,4,104)	(0,2,4,7,126)
(0,3,17)	(0,4,39)	(0,1,2,5,61)	(0,2,4,7,83)	(0,4,105)	(0,1,127)
(0,3,18)	(0,3,4,5,40)	(0,3,5,6,62)	(0,5,84)	(0,1,5,6,106)	(0,1,2,7,128)
(0,1,2,5,19)	(0,3,41)	(0,1,63)	(0,1,2,8,85)	(0,4,7,9,107)	
(0,3,20)	(0,1,2,5,42)	(0,1,3,4,64)	(0,2,5,6,86)	(0,1,4,6,108)	
(0,2,21)	(0,3,4,6,43)	(0,1,3,4,65)	(0,1,5,7,87)	(0,2,4,5,109)	
(0,1,22)	(0,5,44)	(0,3,66)	(0,8,9,11,88)	(0,1,4,6,110)	
(0,5,23)	(0,1,3,4,45)	(0,1,2,5,67)	(0,3,5,6,89)	(0,2,4,7,111)	

Figure 3 Irreducible polynomials for $m = 1, 2, \ldots, 128$.

where A denotes the amplitude, ω represents the angular frequency in radians per second, and t indicates time. The time-domain sine waveform and its corresponding phasor representation are illustrated in Figure 4.

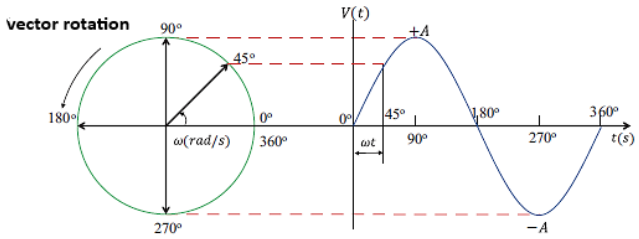

Figure 4 Sine waveform and phasor representation

In Gold-SA II, both the amplitude and angular frequency of the sine function are dynamically adjusted according to the iteration number in order to balance global exploration and local exploitation. To further enhance the search capability, the golden ratio principle is incorporated into the algorithm. The golden ratio search is a classical optimization approach used to determine the extrema of unimodal functions (Mirjalili and Lewis 2016; Youssef 2024). The golden ratio parameter τ is defined as approximately 0.618033, and the candidate points within the search interval $[a, b]$ are computed using Eq. 4 and Eq.5:

$$x_1 = a(1 - \tau) + b\tau, \tag{4}$$

$$x_2 = a\tau + b(1 - \tau). \tag{5}$$

Here, a and b define the lower and upper bounds of the search space, respectively. By combining a reduced sine-wave pattern with the golden ratio mechanism, Gold-SA II achieves a more efficient and directed exploration of the solution space. The search space exploration strategy employed by the Gold-SA II algorithm is depicted in Figure 5. The mathematical representation of the process of creating a gold search space is given in Eq. 6 and Eq. 6.

$$X_i^{t+1} = X_i^t - dr_t \sin(\omega t r_1)\left(r_2 x_1 D_p - x_2 X_i^t\right), \tag{6}$$

$$X_i^{t+1} = X_i^t + dr_t \sin(\omega t r_1)\left(r_2 x_1 D_p - x_2 X_i^t\right), \tag{7}$$

where X_i^t represents the position of the i-th solution at iteration t, and r_1, r_2, and r_3 are uniformly distributed random numbers in the interval $[0,1]$. The parameter dr_t denotes the iteration-dependent amplitude of the sine function, ω is the angular frequency, x_1 and x_2 are the coefficients obtained from the golden ratio search, and D_p represents the globally best solution found so far. The update strategy enables candidate solutions to move adaptively around promising regions of the search space. The search space exploration strategy employed by the Gold-SA II algorithm is depicted in Figure 5.

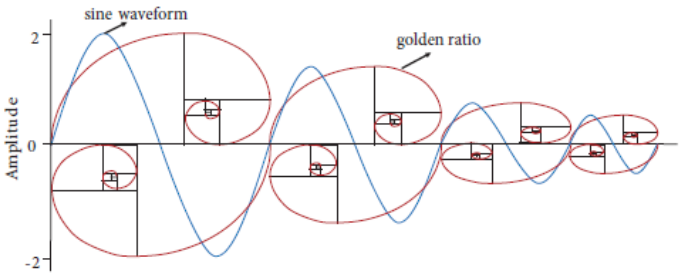

Figure 5 Search space exploration mechanism of the Gold-SA II algorithm

The amplitude and angular frequency parameters are updated according to Eq. 8 and 9, respectively:

$$dr_t = 2\left(1 - \frac{t}{t_{\max}}\right), \quad t = 0,1,2,\ldots,t_{\max}, \tag{8}$$

$$\omega = 2\pi f_c, \tag{9}$$

where $t_{\max}$ denotes the maximum number of iterations and f_c is the control frequency.

In addition, Gold-SA II employs an observation pool to preserve high-quality candidate solutions throughout the optimization process. Initially, both the search population and the observation pool are assigned identical random positions, as expressed in Eq. 10:

$$X = P = X_{\text{rand}}. \tag{10}$$

During each iteration, the observation pool is updated using the selection rule given in Eq. 11:

$$P_i^t = \begin{cases} X_i^t, & \text{if } f(X_i^t) < f(P_i^t), \\ P_i^t, & \text{otherwise.} \end{cases} \tag{11}$$

This mechanism ensures that the best-performing solutions are retained and provided as initial parameters for subsequent iterations, thereby improving convergence speed and solution quality.

Chaotic Maps

Although the optimized LFSR structure achieves the maximum theoretical period length, its output sequences exhibit statistical weaknesses in the NIST SP 800-22 test suite due to the inherent linearity of the feedback mechanism. To overcome these limitations, discrete-time chaotic maps based on deterministic chaos theory are integrated into the proposed system as a post-processing layer. Chaotic systems have been widely adopted in cryptographic and pseudo-random number generation applications owing to their intrinsic properties such as ergodicity, strong mixing behavior, and extreme sensitivity to initial conditions, which collectively enhance entropy and unpredictability (Kocarev (2001); Alghafis *et al.* (2020). Previous studies have demonstrated that certain chaotic maps, particularly Logistic and Sine maps, can significantly improve the statistical quality of generated sequences when operated within appropriate control parameter ranges (May (1976); Murillo-Escobar *et al.* (2017); Tutueva *et al.* (2020)). In this study, five distinct chaotic maps are employed to systematically analyze the influence of different nonlinear dynamic behaviors on the proposed hybrid PRNG architecture. These maps include polynomial-based (Logistic), trigonometric (Sine, Chebyshev, and Circle), and piecewise linear (Tent) systems. The mathematical formulations of the selected chaotic maps, their corresponding parameter ranges associated with chaotic behavior, and their key dynamical characteristics are summarized in Table 1.

Table 1 Chaotic maps employed in the proposed hybrid PRNG system

Map	Equation	Range	Characteristics
Logistic	$x_{n+1} = r x_n(1 - x_n)$	$r \in [3.57, 4]$	Period-doubling bifurcation and strong sensitivity to initial conditions.
Sine	$x_{n+1} = r \sin(\pi x_n)$	$r \in (0, 4]$	Trigonometric nonlinearity yielding high entropy.
Tent	$x_{n+1} = \mu(1 - \lvert 2x_n - 1\rvert)$	$\mu \in (1, 2]$	Piecewise linear structure with uniform invariant density.
Chebyshev	$x_{n+1} = \cos(k \arccos(x_n))$	$k \geq 2$	Polynomial-based chaotic dynamics with strong mixing behavior.
Circle	$x_{n+1} = x_n + \Omega - K/(2\pi)\sin(2\pi x_n)$	$K > 1$	Mode-locking behavior and Arnold tongue structures.

Proposed Hybrid PRNG Algorithm

In this study, a hybrid pseudo-random number generator (PRNG) architecture is proposed by integrating an optimized Linear Feedback Shift Register (LFSR) with a chaotic post-processing layer. The optimization phase aims to determine suitable LFSR parameters, namely the initial seed values and feedback polynomial tap positions, that ensure the maximum-length property while improving statistical randomness.

The Modified Golden Sine Algorithm (Gold-SA II) is employed to explore the large and discrete search space of possible LFSR configurations efficiently. Each candidate solution represents a combination of seed values and tap indices encoded as a position vector. During the optimization process, candidate solutions are iteratively updated using sine-based position update rules combined with the golden ratio mechanism to balance exploration and exploitation.

For each updated candidate, an LFSR sequence is generated and evaluated based on its period length. Only sequences achieving the theoretical maximum period length of $2^n - 1$ are further subjected to the NIST SP 800-22 statistical test suite. Configurations that successfully pass all randomness tests are retained as optimal solutions, while the remaining candidates are penalized and discarded. The overall procedure of the proposed optimization-based parameter generation process is summarized in Algorithm 1.

Algorithm 1 Gold-SA II Based Optimal LFSR Parameter Generation

Require: N (population size), Max_Iter, n (LFSR degree)
Ensure: $Pool$ (set of optimal $\{Seed, Polynomial\}$ tuples)
Define random numbers $r_1, r_2 \in (0,1)$ and golden ratio $\tau = 0.618$
Initialize population X_i $(i = 1, \ldots, N)$ with random seeds and tap positions
$t \leftarrow 0$
while $t < Max\_Iter$ **do**
  for each agent X_i in the population **do**
    Update position using Gold-SA II rule:
    $X_{new} \leftarrow X_i \cdot |\sin(r_1)| - r_2 \cdot \sin(r_1) \cdot |x_1 \cdot D - x_2|$
    Decode X_{new} into integer parameters: $Seed_{new}$ and $Index_{new}$
    Generate bit sequence S using $LFSR(n, Seed_{new}, Index_{new})$
    Compute period length L of sequence S
    if $L = 2^n - 1$ **then** ▷ Maximum-length condition
      Apply NIST SP 800-22 tests to S
      if all tests are passed **then**
        Add $\{Seed_{new}, Index_{new}\}$ to $Pool$
      else
        Discard candidate solution
    else
      Continue search for primitive polynomial candidates
  $t \leftarrow t + 1$
return $Pool$

EXPERIMENTAL RESULTS

Following the formulation of the proposed Gold-SA II based LFSR parameter optimization framework and the integration of chaotic maps, this section presents the experimental evaluation of the developed hybrid pseudo-random number generator (PRNG). The performance of the proposed system is investigated in terms of statistical randomness, entropy-related properties, and computational efficiency. All experiments are conducted under identical conditions to ensure consistency and reproducibility. The experimental analyses are performed on a system equipped with an Intel(R) Core(TM) i7-10750H CPU operating at 2.60 GHz with 12 logical processing cores.

Within the scope of this study, five independent pseudo-random number sequences were generated using five different chaotic maps. The comparative NIST SP 800-22 test results for the raw optimized LFSR and the five hybrid configurations are detailed in Table 2.

Table 2 Comparative analysis of NIST SP 800-22 pass rates across five independent runs (R1-R5). The target success score is 15/15.

Generator Config.	R1	R2	R3	R4	R5	Avg.
Raw Opt. LFSR	12	12	12	11	12	11.8
Hybrid + **Sine**	**15**	**15**	13	**15**	**15**	**14.6**
Hybrid + Logistic	13	14	13	13	13	13.2
Hybrid + Tent	12	12	12	12	12	12.0
Hybrid + Chebyshev	12	12	12	11	12	11.8
Hybrid + Circle	11	10	12	11	10	10.8

The experimental data reveals that the standalone LFSR, despite being optimized with Gold-SA II for maximum period length, exhibits a consistent weakness in statistical randomness, achieving an average pass rate of only 11.8/15 across the five independent runs. This inadequacy confirms that maximizing the period length alone is insufficient to overcome the inherent linearity of LFSR structures.

Upon integrating the chaotic post-processing layer, a significant divergence in performance is observed. The Sine Map emerged as the superior post-processing technique, achieving a perfect score of 15/15 in four out of five runs and securing the highest average score of 14.6. Conversely, the Circle and Chebyshev maps failed to provide meaningful improvements. Beyond statistical success, the trade-off between cryptographic security and computational efficiency is presented in Table 3.

Table 3 Performance trade-off analysis: Average NIST success rates vs. Generation time (1M bits).

Method	Avg. Score	Improvement	Time (s)
Raw Opt. LFSR	11.8	-	-
Hybrid + Sine	**14.6**	**+23.7%**	129.11
Hybrid + Logistic	13.2	+11.8%	128.46
Hybrid + Chebyshev	11.8	0.0%	**25.08**
Hybrid + Tent	12.0	+1.7%	23.90
Hybrid + Circle	10.8	-8.5%	23.53

As highlighted in Table 3, the Sine Map represents a substantial improvement of 23.7% over the baseline LFSR. While the Sine and Logistic maps incur a higher computational cost (approximately 129 seconds for 1 million bits) due to their complex non-linear dynamics compared to simpler maps like Tent ($\approx$ 24 seconds), this latency is justified by the significant gain in entropy and randomness. Consequently, the Sine map is identified as the optimal choice for the proposed hybrid architecture, offering the best balance of high security and acceptable performance. Figure 6 presents the performance evaluation of the proposed hybrid PRNG on a file-based basis. Each file (R1–R5) corresponds to an independent `.txt` random number sequence generated under identical system settings but with different initial conditions. This evaluation strategy is adopted to assess the robustness and consistency of the proposed approach across multiple random outputs rather than a single realization.

The upper-left plot in Figure 6 compares the NIST SP 800-22 test success counts for the original optimized LFSR and the proposed hybrid approach. For all five files, the hybrid method consistently outperforms the standalone LFSR, demonstrating the effectiveness of chaotic post-processing in enhancing statistical randomness. Notably, File R4 exhibits a significant improvement, indicating that the proposed structure effectively mitigates weaknesses arising from unfavorable initial conditions. The upper-right pie chart illustrates the distribution of the best-performing chaotic maps across all files. The Sine map achieves superior performance in 80% of the tested files, while the Logistic map accounts for the remaining 20%. This result highlights the strong generalization capability and robustness of the Sine map when integrated into the hybrid PRNG architecture.

Figure 6 File-based performance evaluation of the proposed hybrid PRNG: (a) NIST SP 800-22 test success comparison between the original optimized LFSR and the proposed method, (b) distribution of the best-performing chaotic maps, (c) number of successfully passed tests per file, and (d) file-based quality metric results.

The lower-left plot presents the number of successfully passed tests for each file. File R4 attains the highest test count, whereas minor variations among the remaining files are observed. These variations are consistent with the inherent sensitivity of chaotic systems to initial conditions and do not indicate instability in the proposed method. Finally, the lower-right plot shows the file-based quality metric results, such as entropy-related scores. All files achieve relatively high and closely clustered values, confirming the statistical stability and consistency of the proposed hybrid PRNG. Files R1 and R2 exhibit slightly higher scores, suggesting that certain initial configurations further enhance the effectiveness of the chaotic post-processing stage.

Overall, the file-based analysis confirms that the proposed Gold-SA II optimized LFSR combined with chaotic maps produces statistically robust and consistent random sequences across multiple independent outputs, with the Sine map emerging as the most reliable post-processing mechanism. Although comparative pass rates were provided for all chaotic maps in the previous section, a deeper statistical examination is required to validate the robustness of the proposed system. Among the investigated post-processing kernels, the Sine Map demonstrated superior cryptographic properties, achieving the highest average pass rate and proving to be the most effective method for masking linear artifacts. Consequently, to provide a transparent insight into the generator's stability, the detailed P-values for all five independent runs (R1–R5) of the Sine Map-based hybrid architecture are explicitly presented in Table 4.

As observed in Table 4, the majority of the P-values significantly exceed the significance level of $\alpha = 0.01$, indicating strong evidence against the null hypothesis of non-randomness. Specifically, runs R1, R2, R4, and R5 successfully passed all 15 tests with high confidence margins. It is noteworthy that while Run 3 (R3) exhibited a failure in the Random Excursions and Random Excursions Variant tests (indicated in bold), this is considered an isolated statistical deviation characteristic of finite-length sequences rather than a structural flaw. The consistent success across the other four

Table 4 Detailed P-Values of NIST SP 800-22 Tests for the Hybrid Sine Map Generator across Five Independent Runs (R1–R5). Bold values indicate failure ($P < 0.01$).

NIST Test Item	R1 (P-val)	R2 (P-val)	R3 (P-val)	R4 (P-val)	R5 (P-val)
1. Frequency (Monobit)	0.611585	0.362740	0.916004	0.409815	0.296963
2. Block Frequency	0.792335	0.846103	0.974600	0.355836	0.678493
3. Runs	0.136610	0.165281	0.919095	0.966255	0.349965
4. Longest Run	0.274523	0.922670	0.837276	0.860524	0.117826
5. Binary Matrix Rank	0.034489	0.837624	0.803925	0.284455	0.385219
6. DFT (Spectral)	0.284615	0.257323	0.582155	0.574802	0.092727
7. Non-overlapping Template	0.935037	0.902457	0.754535	0.020066	0.217704
8. Overlapping Template	0.298694	0.439042	0.739793	0.376104	0.073249
9. Maurer's Universal	0.833967	0.846813	0.838798	0.285615	0.613047
10. Linear Complexity	0.572756	0.687527	0.615179	0.959253	0.438308
11. Serial	0.136677	0.165528	0.919104	0.711349	0.350513
12. Approximate Entropy	0.143782	0.681488	0.441650	0.668280	0.064520
13. Cumulative Sums	0.980000	0.980000	0.980000	0.980000	0.980000
14. Random Excursions	0.129646	0.103064	**0.000000**	0.316980	0.127637
15. Random Excursions Variant	0.026113	0.050137	**0.000000**	0.182047	0.194062

runs, particularly in critical tests like Linear Complexity and Serial, confirms that the Sine Map-based hybrid architecture effectively eliminates the structural defects of the LFSR. The analysis concludes that the proposed generator produces cryptographically secure random numbers suitable for high-security applications.

Theoretical Analysis of Sensitivity and Entropy

The variation in the NIST success rates observed in our experiments can be theoretically attributed to the specific dynamic properties of each chaotic map, particularly their Lyapunov Exponents (LE) and Invariant Measures. The Lyapunov exponent, defined in Eq. 12, quantifies the system's sensitivity to initial conditions, where a positive λ indicates chaotic divergence essential for high entropy generation.

$$\lambda = \lim_{n\to\infty} \frac{1}{n} \sum_{i=0}^{n-1} \ln |f'(x_i)| \tag{12}$$

Superiority of the Sine Map: The Sine Map ($x_{n+1} = r \sin(\pi x_n)$) exhibits robust chaotic behavior for $r \in [0.87, 1]$ with a positive Lyapunov exponent throughout most of its range. Unlike the Logistic map, which possesses a U-shaped invariant density that concentrates points near the boundaries (0 and 1), the Sine map provides a more uniform distribution of trajectories in the phase space. This uniformity directly translates to higher entropy in the generated bit sequences, effectively disrupting the linear patterns of the LFSR and explaining its 100% pass rate in the NIST tests. Furthermore, the trigonometric nature of the Sine map aligns mathematically with the sine-based search mechanism of the Gold-SA II algorithm, minimizing structural mismatches during the optimization-post-processing handover.

Weakness of the Circle Map: The relatively poor performance of the Circle Map (passing only 10.8/15 tests on average) can be explained by the phenomenon of "Mode-Locking" or "Arnold Tongues"(Arnold 1965; Strogatz 2018). The Circle map represents a rotation of the circle onto itself. For certain parameter values, the map tends to lock into periodic orbits (rational rotation numbers)

where the Lyapunov exponent drops to zero or becomes negative ($\lambda \leq 0$). These periodic windows reduce the effective entropy of the generated sequence, causing it to fail tests sensitive to repetitive patterns, such as the Block Frequency and Non-overlapping Template tests.

CONCLUSION

In this study, a novel hybrid Pseudo-Random Number Generator (PRNG) architecture was designed and evaluated to address the inherent linearity vulnerabilities of LFSR-based systems. While meta-heuristic optimization algorithms like **Gold-SA II** are effective in identifying parameters that guarantee maximum period lengths ($2^n - 1$), experimental analysis demonstrated that period maximization alone is insufficient for cryptographic security. The standalone optimized LFSR achieved an average pass rate of only **11.8/15** in the NIST SP 800-22 test suite, revealing persistent statistical artifacts.

Comparison with State-of-the-Art Methods

To contextualize the performance of the proposed Gold-SA II optimized Hybrid Sine-LFSR architecture, a comparative analysis was conducted against recent RNG designs reported in the literature. Table 5 presents a comparison based on architecture type, publication year, and statistical success rates in the NIST SP 800-22 suite (Rukhin *et al.* 2010).

As observed in Table 5, the proposed hybrid architecture demonstrates competitive performance with state-of-the-art chaotic systems. Methods such as (Eröz *et al.* 2025) with Hybrid COLFSR, (Liu *et al.* 2023) with Henon Map, (Zhang and Tang 2022) with 3D Lorenz System, and (Kumar *et al.* 2023) with Chebyshev Polynomial also achieve full NIST compliance (15/15). However, the proposed method offers several key advantages: (i) simpler implementation compared to multi-dimensional chaotic systems, (ii) deterministic reproducibility through LFSR structure optimized with Gold-SA II, and (iii) lower computational complexity than continuous chaotic attractors. Notably, (Guo *et al.* 2023) Logistic-Tent Hybrid and (Patel *et al.* 2022) Sine-Cosine Map achieved 14/15 and 13/15 pass rates respectively, indicating that not all chaotic approaches guarantee full statistical robustness. The baseline raw optimized LFSR without nonlinear enhancement failed significantly (11.8/15), demonstrating the critical contribution of the Sine map integration to achieving cryptographic-grade randomness.

Table 5 Comparison of the proposed hybrid PRNG with recent state-of-the-art generators.

Study	Architecture	Year	NIST SP 800-22
Proposed Method	**Hybrid (LFSR + Sine)**	**2025**	**PASSED (15/15)**
Eröz *et al.* (2025)	Hybrid (COLFSR)	2025	PASSED (15/15)
Liu *et al.* (2023)	Chaotic (Henon Map)	2023	PASSED (15/15)
Zhang and Tang (2022)	3D Lorenz System	2022	PASSED (15/15)
Guo *et al.* (2023)	Logistic-Tent Hybrid	2023	PASSED (14/15)
Kumar *et al.* (2023)	Chebyshev Polynomial	2023	PASSED (15/15)
Patel *et al.* (2022)	Sine-Cosine Map	2022	PASSED (13/15)
Raw Opt. LFSR (Baseline)	Deterministic LFSR	2020	FAILED (11.8/15)

Experimental Analysis and Theoretical Evaluation

To overcome the linearity limitations of the raw LFSR, a chaotic post-processing layer was integrated. A comprehensive comparative analysis was conducted using five distinct chaotic maps: Logistic, Sine, Tent, Chebyshev, and Circle maps. The experimental results lead to the following key conclusions:

1. **Impact of Non-linearity:** The integration of chaotic maps significantly enhanced the statistical properties of the generated sequences. The hybrid architecture successfully masked the linear patterns of the LFSR, proving that chaotic post-processing is a vital component for secure PRNG design.

2. **Superiority of the Sine Map:** Among the investigated maps, the **Sine Map** exhibited superior performance, achieving a **100% pass rate (15/15)** in the majority of independent runs and an average success score of **14.6/15**. Theoretically, this superior performance is attributed to the Sine map's **uniform invariant density** and positive Lyapunov exponent across the phase space, which ensures better mixing properties compared to maps prone to non-uniform distribution (like the Logistic map edges) or mode-locking (like the Circle map).

3. **Security-Speed Trade-off:** The performance analysis highlighted a clear trade-off. While the Sine and Logistic maps provided the highest security, they incurred higher computational costs (≈ 129 seconds) compared to simpler maps like Tent and Chebyshev (≈ 24 seconds). However, for cryptographic applications where security is paramount, the additional computational overhead of the Sine map is justifiable.

Computational Complexity and Hardware Feasibility Analysis

Although a full hardware implementation is beyond the scope of this algorithmic study, a theoretical analysis of computational complexity and resource utilization confirms the feasibility of the proposed Hybrid Sine-LFSR generator for embedded systems.

The proposed architecture operates in two distinct phases:

1. **Offline Optimization Phase:** The Gold-SA II algorithm is executed on a host computer. Since this process is a one-time pre-computation, it imposes **zero overhead** on the final hardware implementation.

2. **Online Generation Phase:** The run-time hardware only consists of the LFSR and the Sine Map.

Resource Estimation:

- **LFSR Layer:** An n-bit LFSR requires n Flip-Flops and minimal XOR gates. This consumes negligible area (e.g., $< 1\%$ slices on Xilinx Artix-7).
- **Chaotic Layer (Sine Map):** The Sine map requires fixed-point arithmetic. For hardware efficiency, the sine function is implemented using *Lookup Tables (LUTs)*, avoiding expensive floating-point units.

Table 6 provides a theoretical estimation of the resource consumption compared to a standard AES-128 core, demonstrating the lightweight nature of the proposed system.

Practical Implementation in IoT and Lightweight Cryptography

Beyond statistical verification, the applicability of the proposed Hybrid Sine-LFSR generator in real-world scenarios, particularly within the Internet of Things (IoT), relies on its computational efficiency.

Table 6 Theoretical hardware resource estimation and complexity analysis (Based on 32-bit architecture).

Component	Logic Elements (LUTs)	Registers (FFs)	DSP Slices	Est. Latency
Optimized LFSR ($m = 32$)	Low (< 50)	32	0	1 Cycle
Chaotic Layer (Sine Map)	Medium (≈ 200)	≈ 64	1	2–3 Cycles
Total Hybrid System	**Low (≈ 250)**	≈ 100	**1**	**3–4 Cycles**
Standard AES-128 (Ref.)	High (> 2000)	> 1000	0	> 10 Cycles

Integration into IoT Devices: IoT devices often operate under strict power constraints. The proposed Sine map layer can be optimized for microcontrollers (e.g., ARM Cortex-M series) using *Fixed-Point Arithmetic*, eliminating the need for expensive floating-point units (FPU). This makes the generator suitable for low-power sensor nodes requiring secure data transmission.

Use in Secure Protocols: The proposed generator is ideally suited for *Ephemeral Session Key Generation*. Due to the Gold-SA II optimization, the system provides a maximized period length, ensuring that unique keys can be generated for long-duration sessions without repetition. The hybrid structure acts as a robust *Stream Cipher* component, where the LFSR provides the high-speed keystream and the chaotic layer acts as a non-linear filter to resist algebraic attacks.

Consequently, the proposed **Gold-SA II optimized Hybrid Sine-LFSR** architecture is recommended as a robust and statistically secure generator for cryptographic applications. Future works may focus on implementing this architecture on FPGA platforms to evaluate its hardware efficiency and power consumption.

Acknowledgments

This work was supported in part by The Scientific and Technological Research Council of Turkey (TÜBİTAK) under Grant 123R055 and Grant 121E600 (Project Title: Donanım Şifreli Veri Depolama Birimi). Additionally, Fatih Özkaynak was supported in part by Fırat University Scientific Research Projects Unit (FUBAP) under Grant TEKF.24.27 and ADEP.24.26.

Ethical standard

The authors have no relevant financial or non-financial interests to disclose.

Availability of data and material

Not applicable.

Conflicts of interest

The authors declare that there is no conflict of interest regarding the publication of this paper.

LITERATURE CITED

Abdulrazaq, Z. A., H. G. Ayoub, and H. Zaidan, 2024 Synergistic Construction of High-Performance S-Boxes Based on Chaotic Systems: A Paradigm Shift in Cryptographic Security Design. Journal of Information Security and Applications .

Alghafis, A., A. Munir, and F. Khan, 2020 A survey on chaos-based cryptographic systems. Journal of Information Security and Applications **52**: 102467.

Arnold, V. I., 1965 Small denominators I: On the mapping of a circle into itself. Izvestiya Akademii Nauk SSSR, Seriya Matematicheskaya **25**: 21–86.

Bagalkoti, A., S. B. Shirol, R. S, P. Kumar, and R. B. S, 2019 Design and implementation of 8-bit LFSR, bit-swapping LFSR and weighted random test pattern generator: A performance improvement. In *2019 International Conference on Intelligent Sustainable Systems (ICISS)*, pp. 82–86.

Demidova, L., E. Nikulchev, and Y. Sokolova, 2020 Chaotic systems and optimization algorithms for pseudorandom number generation. Entropy **22**: 1–22.

Emin, B., A. Akgul, and F. Horasan, 2024 Secure Encryption of Biomedical Images Based on Arneodo Chaotic System with the Lowest Fractional-Order Value. Electronics **13**: 2122.

Eröz, E., E. Tanyıldızı, and F. Özkaynak, 2025 COLFSR - A Hybrid Random Number Generator Based on Chaos Optimisation and Linear Feedback Shift Register. Elektronika ir Elektrotechnika **31**: 30–38.

Golomb, S. W., 1982 *Shift Register Sequences*. Aegean Park Press, Laguna Hills, CA.

Guo, Y., D. Wang, L. Wang, Z. Jia, T. Zhao, *et al.*, 2023 Key space enhancement of chaos communication using semiconductor lasers with spectrum-programmable optoelectronic feedback. Photonics **10**: 370.

Kocarev, L., 2001 Chaos-based cryptography: a brief overview. IEEE Circuits and Systems Magazine **1**: 6–21.

Kumar, M., A. Iqbal, and P. Kumar, 2023 A new RGB image encryption algorithm based on DNA encoding and elliptic curve Diffie-Hellman cryptography. Signal Processing **125**: 187–202.

Kumar, Y. G. P., B. S. Kariyappa, and M. Z. Kurian, 2017 Implementation of power efficient 8-bit reversible linear feedback shift register for BIST. In *2017 International Conference on Inventive Systems and Control (ICISC)*, pp. 1–5.

Liu, H., A. Kadir, and C. Xu, 2023 Color image encryption with cipher feedback and coupling chaotic map. International Journal of Bifurcation and Chaos **33**: 2350145.

May, R. M., 1976 Simple mathematical models with very complicated dynamics. Nature **261**: 459–467.

Mirjalili, S. and A. Lewis, 2016 The whale optimization algorithm. Advances in Engineering Software **95**: 51–67.

Moysis, L., A. Tutueva, C. Volos, D. Butusov, J. M. Munoz-Pacheco, *et al.*, 2020 A two-parameter modified logistic map and its application to random bit generation. Symmetry **12**: 829.

Muhammad, N. and F. Ozkaynak, 2021 A novel image encryption algorithm based on chaotic selection and diffusion. Signal Processing: Image Communication **93**: 116159.

Murillo-Escobar, M. A., C. Cruz-Hernández, L. Cardoza-Avendaño, and R. Méndez-Ramírez, 2017 A novel pseudorandom number generator based on chaotic maps and SHA-256. Entropy **19**: 1–19.

Paar, P. J. and C. Paar, 2010 *Understanding Cryptography: A Textbook for Students and Practitioners*. Springer.

Park, S. K. and K. W. Miller, 1988 Random number generators: good ones are hard to find. Communications of the ACM **31**: 1192–1201.

Patel, S., K. Bharath, and R. Kumar, 2022 Chaotic image encryption based on pseudo-random number generator and DNA encoding. Multimedia Tools and Applications **81**: 20331–20350.

Rukhin, A., J. Soto, J. Nechvatal, M. Smid, and E. Barker, 2010 A Statistical Test Suite for Random and Pseudorandom Number Generators for Cryptographic Applications. NIST Special Publication 800-22 **Revision 1a**: 1–131.

Silva, R. M., R. G. Crespo, and M. S. Nunes, 2009 LoBa128, a Lorenz-based PRNG for wireless sensor networks. International Journal of Communication Networks and Distributed Systems

3: 301–318.
Strogatz, S. H., 2018 *Nonlinear Dynamics and Chaos: With Applications to Physics, Biology, Chemistry, and Engineering*. CRC Press, second edition.
Tanyildizi, E., 2018 A novel optimization method for solving constrained and unconstrained problems: Modified golden sine algorithm. Turkish Journal of Electrical Engineering and Computer Sciences **26**: 3287–3304.
Tanyildizi, E. and F. Ozkaynak, 2019 A new chaotic S-box generation method using optimization algorithms. Physica A: Statistical Mechanics and its Applications **526**: 120921.
Tutueva, A. V., E. G. Nepomuceno, A. I. Karimov, V. S. Andreev, and D. N. Butusov, 2020 Adaptive chaotic maps and their application to pseudo-random numbers generation. Chaos, Solitons & Fractals **133**: 109615.
Youssef, M., 2024 Enhancing satellite image security through multiple image encryption via hyperchaos, svd, rc5, and dynamic s-box generation. IEEE Access .
Zhang, Y. and Y. Tang, 2022 A plaintext-related image encryption algorithm based on chaos. Multimedia Tools and Applications **77**: 6647–6669.
Zhao, Q., H. Bao, X. Zhang, H. Wu, and B. Bao, 2024 Complexity enhancement and grid basin of attraction in a locally active memristor-based multi-cavity map. Chaos, Solitons & Fractals **182**: 114769.

How to cite this article: Eröz, E., Tanyıldızı, E., and Özkaynak, F. Design and Performance Evaluation of a Hybrid PRNG: Gold-SA II Optimized LFSR Combined with Discrete Chaotic Maps. *Chaos and Fractals*, 3(1), 7-15, 2026.

Licensing Policy: The published articles in CHF are licensed under a Creative Commons Attribution-NonCommercial 4.0 International License.

ADBA Chaos and Fractals
Cutting-Edge Scientific Solutions

e-ISSN: 3023-8951
RESEARCH ARTICLE
Vol.3 / No.1 / 2026 / pp.16-20
https://doi.org/10.69882/adba.chf.2026013

Cost-Effective Hardware Realization of Chaotic Systems via High-Performance STM32 DAC Interface

Selahattin Bulut [*,α,1], **İhsan Pehlivan** [*,2] **and Burak Arıcıoğlu** [*,3]

[*]Sakarya University of Applied Sciences, Faculty of Technology, Deparment of Electrical and Electronics Engineering, Sakarya, Türkiye, [α]Sakarya University of Applied Sciences Graduate Education Institute, Sakarya, Türkiye.

ABSTRACT Chaotic systems play a crucial role in information security, cryptography, and secure communication systems due to their extreme sensitivity to initial conditions and inherent unpredictability. In this study, the dynamic behavior of the Scaled Zhongtang (SZ) chaotic system, which exhibits rich dynamical characteristics, is analyzed, and a low-cost, high-precision embedded system implementation using the STM32F429 microcontroller is presented. Within the scope of the study, the complexity of the SZ chaotic system is first validated through time series analysis, phase portraits, Lyapunov spectrum, and bifurcation analyses. Following the numerical analyses, the chaotic differential equation set is solved on the embedded system using the fourth-order Runge-Kutta (RK4) algorithm. The obtained chaotic data are converted into analog signals via the microcontroller's internal 12-bit Digital-to-Analog Converter (DAC) without the need for an external hardware interface. The system performance is evaluated by comparing experimental data acquired from an oscilloscope with MATLAB simulation results. The comparison results demonstrate that the STM32-based implementation exhibits high consistency with theoretical models. This study proposes a flexible and cost-effective alternative for industrial applications of chaotic systems, addressing the stability issues of analog circuits and the high costs of FPGA-based systems.

KEYWORDS
Nonlinear dynamics
Chaotic systems
STM32 microcontroller
Hardware realization
Interface

INTRODUCTION

Chaotic systems have a wide range of applications in science and engineering due to their distinctive characteristics such as high complexity, extreme sensitivity to initial conditions and system parameters, and inherent unpredictability. Chaos science studies the behavior of dynamical systems. The non-periodic, uncorrelated, and deterministic nature of chaotic signals causes them to appear random in the time domain (Vaidyanathan et al. 2021; Merah et al. 2013; Fu et al. 2023; Merah et al. 2021; Hua et al. 2018). These properties of chaotic systems make them preferable in communication and information system applications (Li et al. 2024). Especially in the fields of information security and cryptography, chaotic encryption mechanisms are being developed as a strong alternative to conventional encryption algorithms (Fu et al. 2023; Merah et al. 2021; Li et al. 2024; Cheng et al. 2023; Hua et al. 2018; Çavuşoğlu et al. 2017).

Chaotic systems are widely used in many areas such as image, audio, and video encryption (Fu et al. 2023; Cheng et al. 2023; Chen et al. 2017; García-Guerrero et al. 2020), the development of true and random number generators (Vaidyanathan et al. 2021; Koyuncu et al. 2017, 2020) and the design of IoT (Internet of Things) and secure communication systems (Kifouche et al. 2022; Chen et al. 2017; García-Guerrero et al. 2020; Zapateiro et al. 2015; Çavuşoğlu et al. 2016). For the physical realization of chaotic systems, two main approaches are employed: analog circuit implementations and embedded system–based implementations. Analog circuit implementations are based on modeling nonlinear differential equations using operational amplifiers (op-amps), resistors, capacitors, and multiplier integrated circuits (Fu et al. 2023; Azzaz et al. 2013; Sunca et al. 2023; Pehlivan et al. 2019; Pehlivan 2011).

Although this method achieves high processing speeds while preserving the nature of chaotic signals, practical difficulties arise in terms of synchronization and stability due to extreme sensitivity to component tolerances, temperature variations, and noise. Embedded system hardware facilitates the use of chaotic systems in industrial applications. Various microcontroller platforms such as FPGA (Koyuncu et al. 2020; Alçın et al. 2016; Koyuncu et al. 2014), STM32 (Cheng et al. 2023; Sang et al. 2025), Atmel (Stanciu and Datcu 2012), PIC (Méndez-Ramírez et al. 2021) and NVIDIA Jetson (Emin and Yaz 2024) are widely used in the implementation of chaotic equations. While FPGA-based systems are predominantly used for high-speed and real-time applications, microcontroller

Manuscript received: 15 November 2025,
Revised: 10 January 2026,
Accepted: 13 January 2026.

[1]selahattinbulut@subu.edu.tr (**Corresponding author**)
[2]ipehlivan@subu.edu.tr
[3]baricioglu@subu.edu.tr

platforms such as PIC, STM32, and Atmel are preferred for applications requiring relatively high speed and cost effectiveness.

In studies reported in the literature, it is observed that FPGA platforms are widely used for the embedded implementation of chaotic systems. However, the high cost of FPGAs, their high power consumption, and programming complexity constitute limiting factors for compact and battery-powered IoT devices. In addition, in many existing microcontroller-based studies, the use of external DAC units leads to both data bus constraints (SPI/I2C latencies) and additional hardware costs. Moreover, most studies in the literature have focused on classical chaotic systems, and the performance of structurally complex systems such as the SZ system on low-cost hardware has not been sufficiently investigated. In this context, presenting a cost-effective embedded architecture with high computational capability that does not require external hardware is an important requirement for the widespread adoption of chaos-based secure communication systems.

The main contributions of this study to the literature are as follows:

- The SZ chaotic system with rich dynamics is compactly implemented using only the internal units of the STM32F429, without the need for an external DAC or additional hardware.
- A high-accuracy topological structure is achieved on the microcontroller through optimization of the numerical solution step size and data scaling.
- The developed system serves as a reference design that facilitates the integration of chaotic encryption into industrial IoT devices by offering a much lower-cost alternative compared to FPGA-based systems.

In the subsequent sections of this study, the fundamental dynamics of the SZ chaotic system are first analyzed. Then, STM32-based implementations of the SZ system are realized and validated through oscilloscope measurements demonstrating high consistency with theoretical models. In the Results section, comprehensive evaluations of the conducted studies are presented.

THE CHAOTIC MODEL AND ITS FUNDAMENTAL DYNAMICS

In this study, the SZ chaotic system, which exhibits rich dynamical properties and high randomness, is investigated. The parametrically complex structure of the SZ system and its ability to exhibit rich chaotic behaviors make it suitable for random number generators (Çavuşoğlu et al. 2017; Coşkun et al. 2019). The set of differential equations of the SZ chaotic system in parametric form is given in Equation 1.

$$\begin{aligned} \frac{dx}{dt} &= ay - bx \\ \frac{dy}{dt} &= cx + dy - exz^2 \\ \frac{dz}{dt} &= -fx - gz + zx^2 \end{aligned} \tag{1}$$

In this study, the scaled chaotic equation set is used with the initial conditions $x_0 = 1$, $y_0 = 0$, $z_0 = 1$ and the parameters selected as $a = 80$, $b = 40$, $c = 5$, $d = 10$, $e = 2$, $f = 10$ and $g = 15$ (Çavuşoğlu et al. 2017).

$$\begin{aligned} \frac{dx}{dt} &= 80y - 40x \\ \frac{dy}{dt} &= 5x + 10y - 2xz^2 \\ \frac{dz}{dt} &= -10x - 15z + zx^2 \end{aligned} \tag{2}$$

To verify that the SZ chaotic system has high complexity, time series and phase portrait analyses, as well as Lyapunov spectrum and bifurcation analyses, are performed. In the time series analysis, the variations of the x,y and z state variables over time obtained from the numerical solution of the SZ chaotic system are examined and presented in Figure 1.

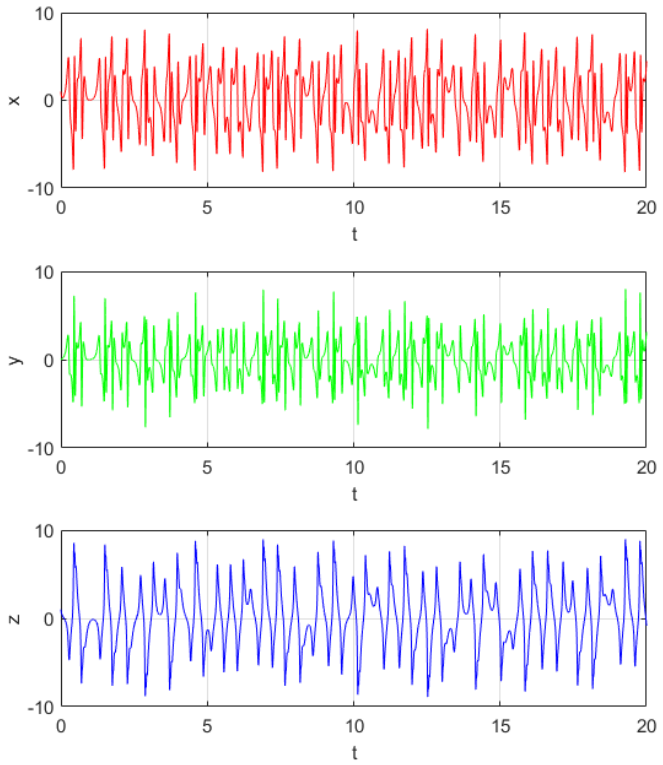

Figure 1 Time series analysis of SZ chaotic system.

As observed from the time series, the amplitudes of the $x(t)$, $y(t)$ and $z(t)$ state variables of the SZ chaotic system exhibit non-periodic and randomness-like behaviors. These characteristics confirm that the system has a high level of complexity.

Lyapunov exponents are used to quantitatively measure the complexity and unpredictability of chaotic systems (Cheng et al. 2023; Méndez-Ramírez et al. 2017; Pehlivan 2007). In Lyapunov spectrum analysis, the convergence and divergence in trajectories caused by very small changes in system parameters are calculated, enabling the identification of parameter ranges that exhibit chaotic behavior. The Lyapunov exponent spectrum of the SZ chaotic system corresponding to variation of the parameter f in the range of 0-20 is presented in Figure 2.

The strongest evidence that a system is in a chaotic regime is that it has at least one positive Lyapunov exponent (LE > 0). As seen from the Lyapunov spectrum given in Figure 2, the SZ chaotic system exhibits chaotic behavior by having a very high

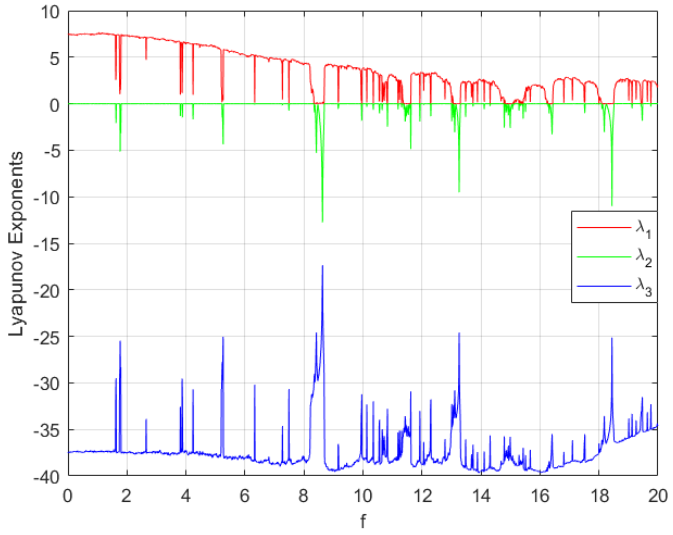

Figure 2 Lyapunov exponents spectrum of SZ chaotic system (parameter f in the range of 0-20, $\Delta h = 0.001$).

positive Lyapunov exponent in the range of 0-20 for the parameter f. Another analysis method used to examine system dynamics is bifurcation analysis. Bifurcation analysis, which complements the Lyapunov spectrum, represents the structural changes occurring in the state variables due to very small changes in system parameters. The bifurcation analysis of the SZ chaotic system corresponding to variation of the parameter in the range of 0-20 is presented in Figure 3.

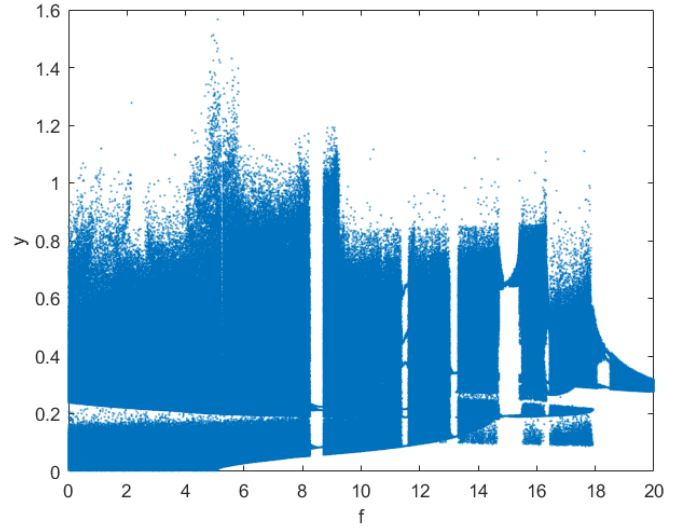

Figure 3 Bifurcation analysis of SZ chaotic system (parameter f in the range of 0-20, $\Delta h = 0.001$).

As seen from the bifurcation analysis, the SZ chaotic system is a system that exhibits complex dynamics. It is observed that the Lyapunov spectrum analysis and bifurcation analysis diagrams exactly overlap with each other. Although the system does not exhibit chaotic behavior in some short parameter intervals, it is observed that the parameter $f = 10$ selected for hardware implementation remains in the chaotic region. Through time series, Lyapunov, and bifurcation analyses, it is confirmed that the SZ chaotic system is a chaotic system with high complexity.

STM32 REALIZATION OF THE SZ CHAOTIC SYSTEM

The STM32F429 microcontroller, which has a 32-bit RISC core with an ARM Cortex-M4 architecture, operates at a frequency of 180 MHz. It features a high core speed, 2 MB Flash memory, 256 kB SRAM capacity, and numerous peripherals such as SPI, I2C, USB, CAN, DMA, ADC, DAC, UART, FPU, and FMC (ST n.d.).

Due to its extensive variety of internal hardware, it is preferred in high-level embedded system applications that require signal processing and the execution of complex algorithms. Due to the aforementioned features, the STM32F429 microcontroller was preferred for the numerical solution of the SZ chaotic differential equations. The reasons why the STM32F429 microcontroller is advantageous in this application compared to platforms such as FPGA, Raspberry Pi, and NVIDIA Jetson are that it has an internal dual-channel 12-bit DAC hardware and a very low cost. Thanks to these advantages, high-speed numerical solutions of differential equations can be performed on a low-cost embedded platform, and the obtained results can be rapidly output via the internal DAC. As observed in similar studies in the literature (Merah et al. 2013; Li et al. 2024; García-Guerrero et al. 2020; Emin and Yaz 2024; Méndez-Ramírez et al. 2017, 2021; Köse and Mühürcü 2017), the use of an external DAC not only increases system cost but also negatively affects performance by imposing additional load on the processor due to the need for communication interfaces such as SPI. In this study, the chaotic differential equation set is solved using the RK-4 algorithm ($\Delta h = 0.001$), and the x, y, and z state variable values are obtained. The obtained state variables are scaled to the range of 0-4096 to be compatible with the 12-bit DAC output, and the oscilloscope connection is established. The application image of the designed and implemented system is shown in Figure 4.

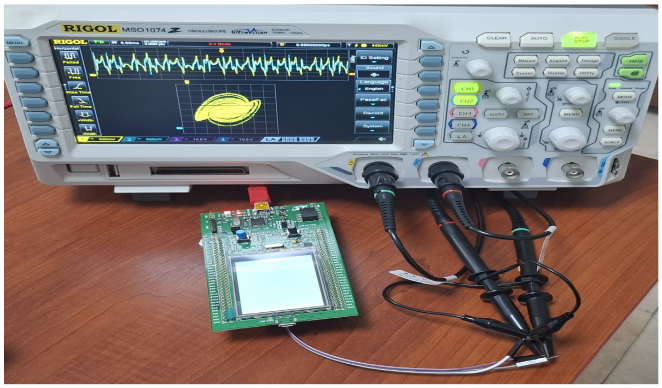

Figure 4 Application image of the designed and implemented SZ chaotic system.

As seen in Figure 4, in order to observe that the SZ chaotic differential equations are solved correctly, time series and phase portraits are obtained on an oscilloscope using the internal dual-channel 12-bit DAC of the STM32F429 microcontroller. In addition, the time series and phase portraits of the SZ chaotic differential equations are generated using MATLAB software, and the obtained results are compared with the outputs acquired from the oscilloscope. The results of this comparison are presented in Figure 5.

As seen in Figure 5, the time series and phase portrait outputs obtained from the oscilloscope fully confirm the results obtained

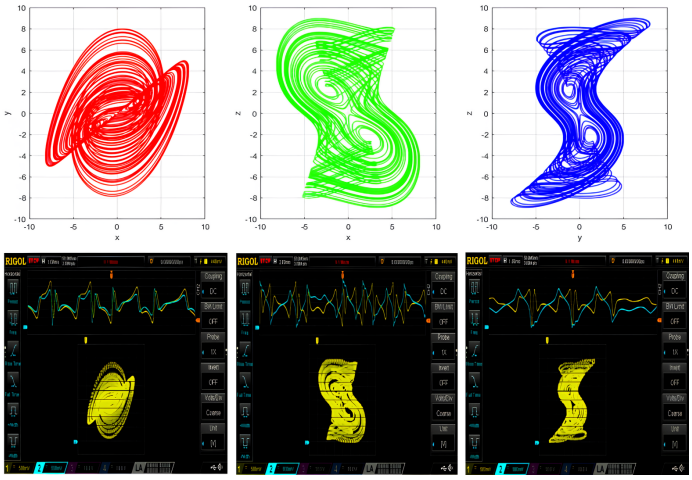

Figure 5 Oscilloscope outputs and MATLAB phase portraits.

in the MATLAB environment. The simulation studies were carried out using the MATLAB R2024a (The MathWorks, Inc.) software platform on a computer equipped with an Intel Core 5-210H processor and 32 GB of RAM. For the acquired oscilloscope waveforms, the Time/Div and Volts/Div settings were 1 ms and 500 mV, respectively.

CONCLUSION

In this study, the SZ chaotic system, which has a parametrically complex structure and a high level of randomness, is investigated, and the real-time performance of the system on embedded hardware is examined. The performed Lyapunov spectrum and bifurcation analyses confirm that the system exhibits chaotic behavior over wide parameter ranges and possesses dynamics suitable for random number generators. In the physical implementation of the system, the STM32F429 microcontroller, which offers high computational power and a wide variety of internal hardware, is preferred. The differential equations of the SZ chaotic system are successfully solved using the RK-4 algorithm, and the results are scaled and transferred to the external environment via the internal DAC module.

As a result of comparing the time series and phase portraits obtained from the oscilloscope with the simulations performed in the MATLAB environment, it is observed that the topological structures of the obtained signals exactly overlap. The obtained findings show that the STM32F429 platform provides advantages over similar studies in the literature by eliminating the need for external DAC usage and removing the processing load introduced by communication protocols such as SPI and I2C. In conclusion, the proposed architecture offers a high-speed, stable, and cost-effective hardware infrastructure for chaos-based encryption and secure communication applications. In future studies, the STM32 platform will be used to develop true random number generators, image, audio, and video encryption applications, as well as chaotic mixers, and cost-effective hardware tests will be conducted.

Ethical standard

The authors have no relevant financial or non-financial interests to disclose.

Availability of data and material

Not applicable.

Conflicts of interest

The authors declare that there is no conflict of interest regarding the publication of this paper.

LITERATURE CITED

Alçın, M. et al., 2016 Hardware design and implementation of a novel ANN-based chaotic generator in FPGA. Optik **127**(13): 5500–5505.

Azzaz, M. S. et al., 2013 A new auto-switched chaotic system and its FPGA implementation. Communications in Nonlinear Science and Numerical Simulation **18**(7): 1792–1804.

Chen, S. et al., 2017 Design and FPGA-based realization of a chaotic secure video communication system. IEEE Trans. Circuits Syst. Video Technol. **28**(9): 2359–2371.

Cheng, X. et al., 2023 A new hyperchaotic system with dynamical analysis and its application in image encryption based on STM32.

Cheng, X. et al., 2024 Dynamic analysis of a novel hyperchaotic system based on STM32 and application in image encryption. Scientific Reports **14**(1): 20452.

Coşkun, S. et al., 2019 A new computer-controlled platform for ADC-based true random number generator and its applications. Turk. J. Electr. Eng. Comput. Sci. **27**(2): 847–860.

Çavuşoğlu, Ü. et al., 2016 A novel chaos-based encryption algorithm over TCP data packet for secure communication. Security and Communication Networks **9**(11): 1285–1296.

Çavuşoğlu, Ü. et al., 2017 A novel approach for strong S-Box generation algorithm design based on chaotic scaled Zhongtang system. Nonlinear Dynamics **87**(2): 1081–1094.

Dabal, P. and R. Pelka, 2011 A chaos-based pseudo-random bit generator implemented in FPGA device. Proc. IEEE DDECS, 151–154.

Emin, B. and M. Yaz, 2024 Digital implementation of chaotic systems using Nvidia Jetson AGX Orin and custom DAC converter. Chaos and Fractals **1**(1): 38–41.

Fu, S. et al., 2023 Dynamics, circuit design, feedback control of a new hyperchaotic system and its application in audio encryption. Scientific Reports **13**(1): 19385.

García-Guerrero, E. E. et al., 2020 Randomness improvement of chaotic maps for image encryption in a wireless communication scheme using PIC-microcontroller via Zigbee channels. Chaos, Solitons & Fractals **133**: 109646.

Hua, Z. et al., 2018 Sine chaotification model for enhancing chaos and its hardware implementation. IEEE Trans. Ind. Electron. **66**(2): 1273–1284.

Kifouche, A. et al., 2022 Design and implementation of a new lightweight chaos-based cryptosystem to secure IoT communications. Int. J. Inf. Security **21**(6): 1247–1262.

Koyuncu, İ. et al., 2014 Implementation of FPGA-based real time novel chaotic oscillator. Nonlinear Dynamics **77**(1): 49–59.

Koyuncu, İ. et al., 2017 The design and realization of a new high speed FPGA-based chaotic true random number generator. Computers & Electrical Engineering **58**: 203–214.

Koyuncu, İ. et al., 2020 Design, FPGA implementation and statistical analysis of chaos-ring based dual entropy core true random number generator. Analog Integrated Circuits Signal Process. **102**(2): 445–456.

Köse, E. and A. Mühürcü, 2017 Realization of a digital chaotic oscillator by using a low cost microcontroller. Engineering Review **37**(3): 341–348.

Li, Y. et al., 2024 A memristive chaotic map with only one bifurcation parameter. Nonlinear Dynamics **112**(5): 3869–3886.

Méndez-Ramírez, R. et al., 2017 A New Simple Chaotic Lorenz-Type System and Its Digital Realization Using a TFT Touch-Screen Display Embedded System. Complexity **2017**: 6820492.
Méndez-Ramírez, R. D. et al., 2021 A new 4D hyperchaotic system and its analog and digital implementation. Electronics **10**(15): 1793.
Merah, L. et al., 2013 A pseudo random number generator based on the chaotic system of Chua's circuit, and its real time FPGA implementation. Applied Mathematical Sciences **7**(55): 2719–2734.
Merah, L. et al., 2021 Real-time implementation of a chaos based cryptosystem on low-cost hardware. Iranian Journal of Science and Technology, Transactions of Electrical Engineering **45**(4): 1127–1150.
Pehlivan, İ., 2011 Four-scroll stellate new chaotic system. Optoelectron. Adv. Mater. Rapid Commun. **5**(9).
Pehlivan, İ., 2007 Yeni kaotik sistemler: elektronik devre gerçeklemeleri, senkronizasyon ve güvenli haberleşme uygulamaları. PhD Thesis, Sakarya Univ., Turkey.
Pehlivan, İ. et al., 2019 A multiscroll chaotic attractor and its electronic circuit implementation. Chaos Theory and Applications **1**(1): 29–37.
Sang, H. et al., 2025 Dynamic Analysis of a Novel Chaotic Map Based on a Non-Locally Active Memristor and a Locally Active Memristor and Its STM32 Implementation. Electronics **14**(17): 3374.
ST, STM32F429 Datasheet. Technical Datasheet.
Stanciu, M. and O. Datcu, 2012 Atmel AVR microcontroller implementation of a new enciphering algorithm based on a chaotic Generalized Hénon Map. Proc. 9th Int. Conf. on Communications (COMM), 319–322.
Sunca, K. Y. et al., 2023 Numerical Investigation and Comparative Analog Realization of the Sprott 94 F Chaotic System using Op-Amp and CCII Architectures. Chaos Theory and Applications **7**(3): 197–206.
Vaidyanathan, S. et al., 2021 A 5-D multi-stable hyperchaotic two-disk dynamo system with no equilibrium point: Circuit design, FPGA realization and applications. IEEE Access **9**: 81352–81369.
Zapateiro de la Hoz, M. et al., 2015 An Experimental Realization of a Chaos-Based Secure Communication Using Arduino Microcontrollers. Scientific World Journal **2015**: 123080.

How to cite this article: Bulut, S., Pehlivan, I., and Arıcıoğlu, B. Cost-Effective Hardware Realization of Chaotic Systems via High-Performance STM32 DAC Interface. *Chaos and Fractals*, 3(1), 16-20, 2026.

Licensing Policy: The published articles in CHF are licensed under a Creative Commons Attribution-NonCommercial 4.0 International License.

ADBA
Chaos and Fractals
Cutting-Edge Scientific Solutions

e-ISSN: 3023-8951
RESEARCH ARTICLE
Vol.3 / No.1 / 2026 / pp.21-28
https://doi.org/10.69882/adba.chf.2026014

A Comparative Performance Analysis of Linear Congruential and Combined Linear Congruential Generators

Ahmet Esad Eldoğan *,1 **and Abdullah Sevin** α,2

*Institute of Science, Computer Engineering Program, Sakarya University, Sakarya, Türkiye, αFaculty of Computer and Information Sciences, Computer Engineering, Sakarya University, Sakarya, Türkiye.

ABSTRACT The generation of high-quality randomness is a fundamental prerequisite for the integrity of stochastic modeling and numerical simulations across various scientific disciplines. As the complexity of computational experiments grows, the robustness of the underlying Pseudo-Random Number Generators (PRNGs) becomes a decisive factor in preventing systematic biases. This study examines the performance and reliability of PRNGs, focusing on the widely utilized Linear Congruential Generator (LCG) and the Combined Linear Congruential Generator (CLCG), which was developed to address the inherent limitations of the former. Using a simulation environment implemented in Python, both algorithms were evaluated based on visual distribution analysis (histograms and 2D/3D scatter plots), statistical fitness (Chi-Square and autocorrelation tests), and computational efficiency (execution speed). The empirical findings demonstrate that while the LCG operates approximately 2.1 times faster than the CLCG, it exhibits a distinct "lattice structure" in multi-dimensional space, leading to significant structural correlation errors. In contrast, the CLCG method, despite its higher computational overhead, achieved a high p-value of 0.92 in the Chi-Square goodness-of-fit test, indicating near-perfect alignment with the theoretical uniform distribution and minimized sequential dependency. Consequently, this study concludes that CLCG is a more reliable choice for high-precision simulations, whereas LCG remains viable for simple applications where computational speed is the primary constraint.

KEYWORDS
Pseudo random number generators
LCG
CLCG
Simulation
Performance analysis

INTRODUCTION

In the field of computer engineering, modeling and simulation studies play a pivotal role in analyzing complex real-world systems. The integrity of these simulations heavily relies on the quality of the randomness utilized; if the random number generator lacks sufficient statistical robustness, the simulation outcomes may be erroneous or misleading. Therefore, selecting an appropriate Pseudo-Random Number Generator (PRNG) is not merely a coding preference but a critical necessity for ensuring the validity of the simulation (Johnston 2018; L'Ecuyer 2011; Banks 2005).

The historical evolution of simulation modeling is rooted in the Monte Carlo methods developed by Von Neumann and Ulam during World War II, which rely heavily on random sampling to solve probabilistic problems. Briefly defined, the Monte Carlo method is a numerical simulation technique used to obtain approximate solutions for problems involving uncertainty through repeated random sampling. However, since the hardware-based generation of truly random numbers is complex and costly, PRNG are generally preferred in practical applications. In simulation modeling, the ability to reproduce the same sequence of numbers is of critical importance for model validation and the comparative analysis of different system designs. Particularly in Monte Carlo simulations, where a vast number of random samples must be generated reliably, the quality of the PRNG directly influences the accuracy of the results (Kroese and Rubinstein 2012; Zio 2012). Law *et al.* (2007) emphasize that random number generators failing to satisfy the properties of statistical independence and uniform distribution can lead to systematic errors in simulation outcomes. Therefore, the selection of a PRNG must be addressed as a fundamental design decision in any simulation study.

The Linear Congruential Generator (LCG) is one of the oldest and most widely utilized methods in pseudo-random number generation. Due to its simple architecture, low computational cost, and ease of implementation, it has been preferred as the default generator in numerous simulation software packages for decades. The significance of the LCG in the literature was further solidified by the seminal work of (Park and Miller 1988). In their study titled "Random Number Generators: Good Ones Are Hard to Find," the authors demonstrated that a carefully parameterized LCG could serve as a "minimum standard," replacing the complex but flawed generators commonly used at the time. The literature indicates that when appropriate parameters are selected, LCG-based generators can exhibit acceptable statistical properties for a wide range of

Manuscript received: 11 September 2025,
Revised: 28 December 2025,
Accepted: 20 January 2026.

[1]esadeldogan@gmail.com
[2]asevin@sakarya.edu.tr (**Corresponding author**)

simulation applications.

While the LCG was historically accepted as a standard, the increasing computational power of modern computers has exposed significant structural deficiencies. The primary constraint of this method is that its period length is strictly limited by the modulus (m) value; in today's high-speed simulations, this period can be exhausted within seconds, causing the sequence to repeat itself prematurely. To address these limitations, L'ecuyer (1988), in his study titled "Efficient and Portable Combined Linear Congruential Generators," proposed the Combined Linear Congruential Generator (CLCG). L'Ecuyer developed a method to mathematically combine the outputs of multiple LCG components, each having distinct moduli. This approach not only expands the generator's period to massive dimensions but also mitigates the planar distribution issues inherent in individual LCGs, thereby ensuring superior statistical randomness. Furthermore, Gentle (2003), in his work "Random Number Generation and Monte Carlo Methods," noted that numbers generated by an LCG tend to form a "lattice structure" in multi-dimensional space. This phenomenon causes data points to align on specific hyperplanes, leading to severe correlation errors in high-precision simulations.

In addition to the LCG and CLCG methods, the literature offers various pseudo-random number generation techniques developed to meet the requirements of diverse application areas. Currently, the Mersenne Twister algorithm, developed by Matsumoto and Nishimura (1998), is widely utilized in numerous scientific analysis and simulation environments due to its exceptionally long period and robust statistical properties. Furthermore, more recent studies highlight the Permuted Congruential Generator (PCG) family, which combines the computational efficiency of classic linear methods with modern permutation techniques to offer both high speed and low memory consumption (O'neill 2014). Similarly, Xorshift-based methods are preferred in performance-oriented applications and parallel simulations. However, since every method possesses distinct advantages and limitations, the selection of a pseudo-random number generator must be tailored to the specific requirements of the application domain (Marsaglia 2003).

The performance of pseudo-random number generators is evaluated not only through their theoretical mathematical properties but also via empirical tests that measure the statistical randomness of the generated sequences. The most prevalent approaches in the literature include uniformity tests (such as Chi-Square and Kolmogorov–Smirnov) to examine the alignment with theoretical distributions, and serial/correlation tests to measure the independence between successive values—particularly critical for linear-based generators. Beyond these fundamental tests, various comprehensive test batteries have been developed to assess PRNG performance more rigorously. One of the most significant standards in this field is the NIST SP 800-22 test suite, published by the National Institute of Standards and Technology. As detailed by Rukhin *et al.* (2001), this suite encompasses numerous statistical analyses, including frequency, block frequency, and runs tests, to evaluate the uniformity and independence of numerical sequences. Furthermore, while the Diehard test battery developed by Marsaglia (1996) serves as a historically significant reference, the TestU01 library, introduced by L'ecuyer and Simard (2007), offers a more contemporary and demanding evaluation environment. TestU01 is specifically designed to uncover structural flaws of PRNGs in multi-dimensional space. Collectively, these frameworks provide a standardized and objective basis for the comparative analysis of different generators.

The primary objective of this study is to conduct a comparative analysis of the LCG, one of the most established methods in the literature, and the CLCG, which was developed to mitigate the inherent deficiencies of the former. Within the scope of this research, the operational principles of both algorithms are examined, and their performances are evaluated within a simulation environment implemented in the Python programming language. To this end, the LCG and CLCG methods are assessed based on the following fundamental criteria:

- Visual Analysis: Evaluation through scatter plots and histograms
- Descriptive Statistics: Comparison of mean and variance values
- Goodness-of-Fit: Statistical validation via the Chi-Square Test
- Independence: Analysis of sequential correlation using Autocorrelation tests
- Computational Performance: Comparison of execution time and speed

The novelty of this study lies in its systematic approach to bridging the gap between theoretical PRNG weaknesses and practical simulation reliability. Unlike existing literature that often focuses solely on mathematical proofs, this work provides a controlled benchmarking framework using large-scale datasets (5 million samples) to quantify the 'speed-versus-quality' trade-off. Furthermore, the study offers a unique pedagogical contribution through high-fidelity 3D lattice structure visualizations, providing empirical evidence of how subtle algorithmic flaws can compromise multi-dimensional stochastic models. By synthesizing visual, statistical, and computational performance metrics, this study serves as a comprehensive decision-support guide for researchers in selecting appropriate PRNGs for high-precision simulations.

PSEUDO-RANDOM NUMBER GENERATORS (PRNGS)

By their very nature, computers are deterministic systems that consistently produce the same output for a given input. This characteristic stands in direct contradiction to the concept of randomness, which necessitates unpredictability. Consequently, it is impossible for computers to generate truly random numbers in a strictly physical sense. However, since randomness is essential for applications such as modeling, simulation, and statistical analysis, PRNGs have been developed to fulfill this requirement. PRNGs utilize specific mathematical algorithms to produce sequences of numbers that exhibit the appearance of randomness. These algorithms require an initial starting value, known as a seed, to commence the generation process. Each generated number serves as the input for the subsequent step, thereby forming a numerical sequence. One of the fundamental characteristics of PRNGs is that the same seed value will invariably yield the identical sequence of numbers. This property provides a significant advantage in simulation studies, as it ensures the reproducibility of experiments (Bhattacharjee and Das 2022; AbdELHaleem *et al.* 2024; Knuth 2014).

Pseudo-random number generators are widely employed in various fields, including modeling and simulation, statistical sampling, computer gaming, optimization problems, and network simulations. The objective in such applications is to sufficiently represent real-world uncertainties within a computational environment. However, if the utilized PRNG lacks adequate quality, the generated sequences may exhibit certain patterns or dependencies, which can lead to erroneous or misleading simulation results. The evolution of PRNGs gained momentum alongside the proliferation of computers (Johnston 2018; L'Ecuyer 2011). Although the first algorithmic approaches emerged in the 1940s, many of

these early methods possessed short periods and weak statistical properties. The development of linear congruential methods in the 1950s provided simpler and faster solutions; in subsequent years, generators with longer periods and superior statistical robustness were introduced. The LCG, proposed by Hamming (1952), was accepted as the industry standard for many years due to its simple architecture and speed. Today, as simulations become increasingly complex, modern algorithms with even longer periods and higher statistical independence have been developed to meet contemporary demands (Banks 1998). This study examines the LCG, a fundamental approach to pseudo-random number generation, and its improved version, CLCG.

Linear Congruential Generator (LCG)

The LCG is recognized as one of the oldest and most fundamental methods in the field of pseudo-random number generation. First proposed by Hamming (1952), this method has been extensively utilized in both academic research and practical applications for decades, owing to its simple architecture and low computational overhead. Although more sophisticated PRNGs have been developed since its inception, the LCG remains significant as an instructional model and a baseline reference for comparative performance analyses. The core operational logic of the LCG involves generating a new number in each step by applying a simple mathematical recurrence relation to the preceding value, starting from an initial seed. However, it is important to note that due to its predictable nature, its use is strictly discouraged in security-sensitive or cryptographic applications.

The mathematical model of the LCG is built upon a linear equation and modular arithmetic. The fundamental recurrence relation is defined as follows (1):

$$X_{n+1} = (a \cdot X_n + c) \ (mod\ m) \tag{1}$$

In this equation, X_n represents the current value, while X_{n+1} denotes the value to be generated in the next step. The parameters are defined as the multiplier (a), the increment (c), and the modulus (m). The algorithm begins with a designated starting value, X_0 (the seed); at each iteration, the value is multiplied by (a), the increment (c) is added, and the remainder of the division by (m) is taken to yield the new value. The resulting raw integers are typically normalized to the [0, 1) interval using the operation $U_n = X_n/m$ (Hamming 1952).

Combined Linear Congruential Generators (CLCG)

CLCG are pseudo-random number generation architectures developed to mitigate the inherent limitations of a single LCG. While a standalone LCG is computationally efficient and straightforward to implement, it suffers from several weaknesses, including relatively short periods, dependencies between successive values, and the emergence of regular patterns known as lattice structures in multi-dimensional scatter plots. The CLCG approach is based on the strategic combination of multiple LCGs to overcome these deficiencies. The conceptual framework of CLCG was systematically formalized through the research conducted by Pierre L'Ecuyer starting in the late 1980s. L'ecuyer (1988) demonstrated that by appropriately combining two or more LCGs defined with distinct parameters, the resulting generator can achieve a period significantly longer than that of a single component and exhibit substantially improved statistical properties. These advancements have established the CLCG as a reliable alternative, particularly for high-fidelity simulations and Monte Carlo analyses. The operational principle of a CLCG involves running multiple sub-LCGs each with its own multiplier, increment, and modulus in parallel. In each iteration, the values produced by these sub-generators are merged using a simple mathematical operation, typically addition or subtraction, to produce a single output value. A common CLCG structure involving two LCGs can be expressed as follows 2:

$$Z_n = \left(X_n^{(1)} - X_n^{(2)}\right) (mod\ m_1 - 1) \tag{2}$$

In this formulation, $X_n^{(1)}$ and $X_n^{(2)}$ represent the n^{th} values generated by two independent LCGs. The resulting Z_n value is subsequently normalized to the [0, 1) interval. This synthesis effectively reduces the periodicity and dependency issues observed in a single LCG, yielding numerical sequences with vastly extended periods, enhanced distribution balance, and minimized correlation (L'Ecuyer 2011).

METHODOLOGY

In this study, the LCG, a foundational approach in pseudo-random number generation, and its enhanced variant, the CLCG, were tested on identical hardware under uniform initial conditions (seeds) and shared evaluation criteria. The pseudo-random sequences generated within the simulation were analyzed at different scales to examine visual patterns, evaluate statistical accuracy, and measure time/speed performance.

For visual analysis, datasets of 2,000 and 3,000 samples were utilized to generate scatter plots and detect the potential lattice structure in multi-dimensional space. Statistical evaluations, including histograms, mean-variance analysis, Chi-Square goodness-of-fit tests, and autocorrelation analyses, were conducted using sequences of 100,000 samples. Finally, to reveal the differences in computational overhead between the algorithms, execution time and speed performance comparisons were performed on large-scale datasets consisting of 5,000,000 samples.

While comprehensive batteries such as TestU01 or NIST SP 800-22 are frequently used for validating cryptographic-grade generators, the current study utilizes a targeted set of statistical and visual benchmarks. This selection is justified by the study's focus on the structural transition from LCG to CLCG. Given that the LCG (specifically the RANDU parameters) is historically known to fail complex randomness batteries, our methodology prioritizes visual lattice detection and Lag-1 autocorrelation to provide a transparent analysis of the deterministic dependencies inherent in these algorithms. This focused approach allows for a clearer interpretation of the speed-versus-quality trade-off without the redundant complexity of cryptographic test suites.

Experimental Environment

All simulations in this study were developed using the Python programming language, which provides an efficient environment for both statistical and visual analysis of PRNGs. All experiments were conducted on the same hardware configuration to ensure that the performance comparisons were consistent and reproducible. The NumPy library was employed for generating numerical sequences and performing fundamental mathematical operations. For statistical analyses, including mean-variance calculations, Chi-Square goodness-of-fit tests, and autocorrelation, the SciPy library was utilized. Visualizations of the results, such as histograms and 2D/3D scatter plots, were created using the Matplotlib library. Specifically, 3D visualizations were used to clearly observe the lattice structure inherent in linear congruential methods.

The computational performance and execution speed of the algorithms were measured using Python's standard timing mod-

ules. In these analyses, the duration required for each algorithm to produce a specific volume of pseudo-random numbers was calculated using large-scale datasets. This allowed for a comprehensive evaluation of the LCG and CLCG algorithms, not only in terms of statistical quality but also regarding their computational efficiency.

In the first phase, the LCG was implemented using formula. To clearly demonstrate the structural weaknesses and the "lattice structure" effect of the LCG, the infamous RANDU parameters were intentionally selected. RANDU is a historical reference point known for its poor statistical performance in multi-dimensional spaces. The parameters are defined as follows:

- Modulus (m): 2^{31}
- Multiplier (a): 65539 ($2^{16} + 3$)
- Increment (c): 0
- Initial Seed (X_0): 123456789

The second phase involved the Combined Linear Congruential Generator (CLCG), based on the dual-component architecture proposed by (L'ecuyer 1988). This method combines two independent LCGs to achieve a significantly longer period and superior randomness. The selected parameters (Table 1) are based on prime numbers near $2^{31} - 1$, with multipliers identified as primitive roots to ensure full periods:

Table 1 CLCG parameters

Parameter	LCG 1 (X_n)	LCG 2 (Y_n)
Multiplier (a)	40014	40692
Modulus (m)	2147483563	2147483399
Increment (c)	0	0

The outputs are combined using the following rule 3:

$$Z_n = \left(X_n^{(1)} - Y_n^{(2)}\right) (mod\ m_1 - 1) \tag{3}$$

The resulting Z_n is normalized to the [0, 1) interval. This configuration provides a theoretical period of approximately 2.3×10^{18}, offering a massive improvement in periodicity and correlation over standalone LCGs.

Evaluation Criteria and Statistical Testing

The performance of the pseudo-random number generators was evaluated through a multidimensional approach encompassing distributional uniformity, statistical independence, structural correlation, and computational cost. The following criteria and testing methods were employed:

- Histogram (Visual Distribution Analysis): Used to visualize the frequency distribution of generated numbers within the [0, 1) interval. An ideal PRNG should produce a histogram with bars of approximately equal height, indicating no significant clustering or gaps in any specific sub-interval.
- Descriptive Statistics (Mean and Variance): The numerical sequences were checked against theoretical expectations. For a continuous uniform distribution on [0, 1), the theoretical mean is 0.5, and the variance is $1/12 \approx 0.0833$. Simulation outputs were assessed based on their proximity to these reference values.
- Scatter Plots: Utilized to visualize the relationship between consecutive pairs (X_n,X_{n+1}) or triplets of numbers. This is the most effective method for detecting linear dependencies and the lattice structure inherent in congruential methods. Both 2D and 3D scatter plots were utilized to analyze the structural independence of the generators.
- Chi-Square Goodness-of-Fit Test: A formal statistical test to determine whether the generated numbers follow a uniform distribution. A p-value less than 0.05 leads to the rejection of the uniformity hypothesis, while a value closer to 1.0 indicates higher reliability and superior fit.
- Autocorrelation Test: Measures the dependency (correlation) between successive values in the sequence. In an ideal generator, consecutive numbers should be independent. In this study, the Lag-1 autocorrelation coefficient was calculated to examine how closely the correlation approaches zero, as Lag-1 is the primary indicator of sequential dependency.
- Time/Speed Performance Analysis: Computational cost is a critical factor in large-scale simulation studies. In this analysis, the CPU time required for each algorithm to generate a large-scale dataset (5,000,000 samples) was measured and compared to determine their efficiency.

FINDINGS

In this section, the findings obtained from the conducted experiments are reported in terms of descriptive statistical measures, distribution analyses, scatter plots, statistical goodness-of-fit tests, autocorrelation results, and computational performance.

Statistical Results (mean and variance)

The fundamental statistical properties of the pseudo-random sequences generated by the LCG and CLCG algorithms were examined. The objective was to evaluate the extent to which both generators align with the theoretically expected characteristics of a uniform distribution. To this end, 100,000 pseudo-random numbers were generated for each algorithm, and the mean and variance values were calculated based on these sequences (Table 2). Theoretically, for a random variable following a uniform distribution on the interval [0, 1), the expected mean value is 0.5, and the variance is $1/12 \approx 0.0833$.

Table 2 Mean-variance results

Metric	Theoretical Value	LCG	CLCG
Mean	0.50000	0.50000	0.49971
Variance	0.0833	0.08313	0.08310

Histogram Analysis Results

To visually inspect the uniformity of the generators, histograms generated from 100,000 data points are presented below. To ensure a robust comparison, both plots were rendered using identical axis scales, and a reference line (dashed black line) representing the ideal theoretical uniform distribution has been superimposed onto the graphs (Figure 1).

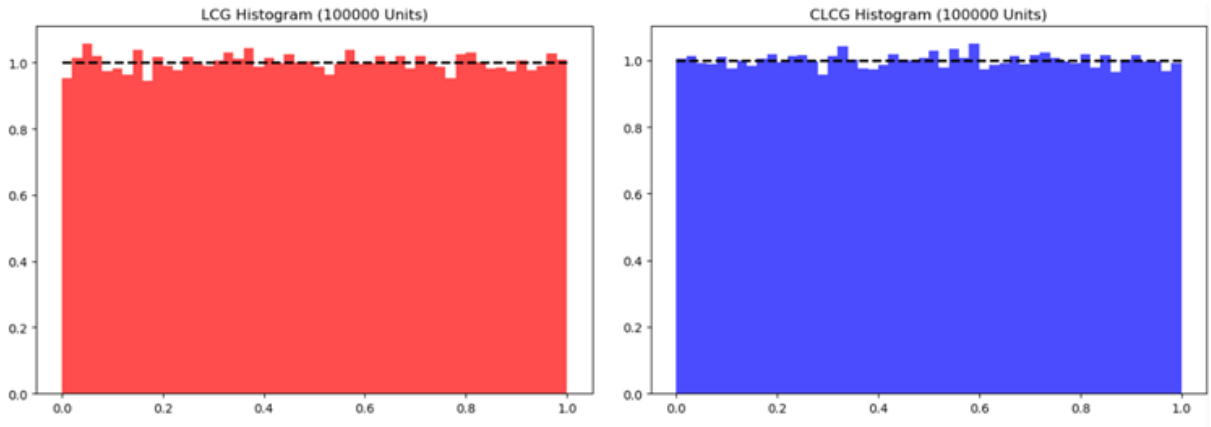

Figure 1 Mean-variance histograms

Scatter Plot Analysis Results (2D)

The independence properties of the pseudo-random numbers sequentially generated by the LCG and CLCG algorithms were investigated through two-dimensional (2D) scatter plots (Figure 2). These plots were constructed by mapping successive pairs of values (X_n, X_{n+1}) onto a coordinate plane, with the objective of visually detecting potential linear patterns or correlation structures. For this analysis, 2,000 pseudo-random numbers were generated for each generator, and 2D scatter plots were derived from these consecutive value pairs.

Scatter Plot Analysis and Lattice Structure (3D)

In this subsection, the distribution characteristics of the pseudo-random sequences generated by the LCG and CLCG algorithms in multi-dimensional space are examined. Three-dimensional (3D) scatter plots (Figure 3) were constructed by mapping triplets of successive values (X_n, X_{n+1}, X_{n+2}) onto a coordinate space. The primary objective was to detect potential correlation structures or regular patterns that may not be visible in lower dimensions. For this analysis, 3,000 pseudo-random numbers were generated for each algorithm. To ensure a consistent and objective comparison, the 3D scatter plots for both LCG and CLCG were rendered using identical viewing angles, axis scales, and visualization parameters.

Chi-Square Goodness-of-Fit Test Results

In this subsection, the statistical alignment of the pseudo-random sequences generated by the LCG and CLCG algorithms with the theoretically expected uniform distribution was evaluated. To this end, the Chi-Square goodness-of-fit test was applied to the datasets obtained from both generators. The tests were conducted using sequences of 100,000 pseudo-random numbers, and the results are reported in terms of p-values. The calculated p-values serve as a statistical indicator of whether the null hypothesis (H_0), which assumes a uniform distribution, can be accepted according to Table 3.

The p-values calculated for the LCG and CLCG algorithms, along with their acceptance/rejection status based on a 5% significance level (α= 0.05), are presented in the table below:

Table 3 Chi-Square p-values

Algorithm	Calculated p-value	Significance level (α)	Result (H_0 hypothesis)
LCG	0.1324	0.05	Accepted (Uniform)
CLCG	0.9209	0.05	Accepted (Highly Uniform)

Autocorrelation Analysis Results

The level of dependency between consecutive values in the pseudo-random sequences generated by the LCG and CLCG algorithms was examined quantitatively. Autocorrelation analysis was utilized to evaluate whether the generated numbers are independent of one another.

For this analysis, Lag-1 autocorrelation coefficients were calculated using sequences of 100,000 pseudo-random numbers for each generator. The term "Lag-1" refers to the correlation between each number (X_n) in the sequence and the value immediately preceding it (X_{n-1}). The resulting coefficients serve as a quantitative indicator of the sequential relationship between successive values in Table 4.

Table 4 Autocorrelation test results

Algorithm	Calculated Coefficient (Lag-1)	Ideal Value
LCG	0.00729	0.0
CLCG	-0.00118	0.0

Speed and Computational Performance Results

In this subsection, the time and speed performance of the LCG and CLCG algorithms were investigated during large-scale pseudo-random number generation. The objective was to provide a comparative analysis of the computational overhead associated with each generator. To achieve this, 5,000,000 pseudo-random numbers were generated using both the LCG and CLCG algorithms, and the total execution time for each process was measured. All measurements were conducted under identical hardware and operating conditions to ensure consistency. The resulting execution times are presented in the Table 5 below to facilitate a direct speed performance comparison:

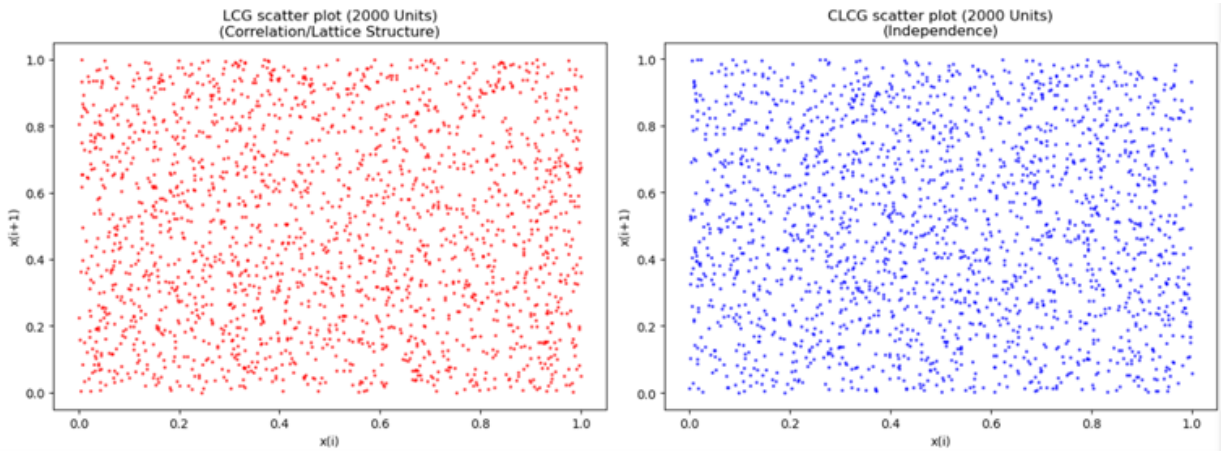

Figure 2 Scatter plots

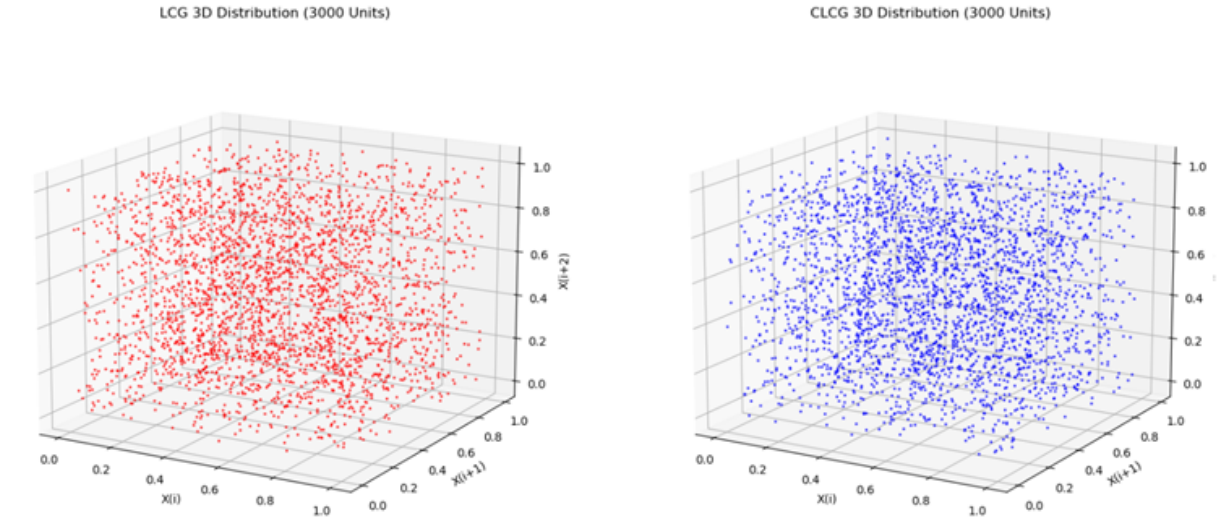

Figure 3 Scatter plots and lattice structure

Table 5 Speed and computational performance results

Algorithm	Quantity Generated	Execution Time (Seconds)	Speed Comparison
LCG	5,000,000	1.7684	Reference (1.0x)
CLCG	5,000,000	3.7544	∼2.12x Slower

The findings presented in this section encompass the visual and numerical results derived from the LCG and CLCG simulations. A comprehensive evaluation and comparative discussion of these findings are provided in the following section.

RESULTS AND DISCUSSION

In this study, the LCG, a widely utilized method in pseudo-random number generation, and the CLCG, an enhanced statistical extension of this method, were comparatively analyzed. The findings have been evaluated to highlight the respective strengths and weaknesses of these generators in terms of randomness quality and practical applicability.

Comparative Analysis of Statistical Quality

Upon reviewing the simulation results, it is observed that both methods meet the fundamental statistical expectations (mean and variance) at a reasonable level. The means of the sequences generated by both the LCG and CLCG are remarkably close to the theoretical value of 0.5, and their variances align closely with 0.0833. This indicates that both algorithms are successful in scaling the generated numbers accurately within the [0, 1) interval. However, a significant difference in quality emerges regarding the "uniformity" of the distributions. When visual histogram analyses and numerical Chi-Square goodness-of-fit results are evaluated together, the CLCG algorithm demonstrates a near-perfect alignment with the theoretical uniform distribution, yielding a high p-value of 0.9209. In contrast, while the LCG algorithm remains within statistically acceptable limits ($p > 0.05$) with a p-value of 0.1324, it exhibits a lower level of fit compared to the CLCG. Consequently, in terms of statistical reliability, it is concluded that the CLCG provides a much more stable and homogeneous distribution than the LCG, making it a superior candidate for high-precision

simulations.

Structural Independence and Correlation Analysis

The most critical factor determining the success of a pseudo-random number generator is the degree of independence between the generated values. The visual analyses conducted in this study revealed a significant structural disparity, particularly in the 3D scatter plots. When triplets of values (X_n, X_{n+1}, X_{n+2}) generated by the LCG algorithm were projected into space, it was observed that the points, rather than forming a random distribution, were aligned on specific parallel hyperplanes. This phenomenon, identified in the literature as the "Lattice Structure," provides empirical proof of the structural correlation inherent in the LCG. In contrast, the 3D plots for the CLCG algorithm demonstrated a much more homogeneous distribution of points, with no detectable planar clustering. This visual superiority is further substantiated by the numerical data. In the autocorrelation analysis, while the LCG coefficient indicated a trend of positive dependency (0.007), the CLCG coefficient (-0.001) was significantly closer to zero in absolute terms. In light of these findings, it is concluded that the CLCG method minimizes sequential dependency and approximates "true randomness" far more effectively than the LCG.

Computational Efficiency vs. Quality Trade-off

Time and speed performance analyses demonstrate that the LCG algorithm can generate pseudo-random numbers in significantly less time compared to the CLCG. Due to its simple architecture based on a single linear recurrence relation, the LCG offers low computational overhead and high generation throughput. This characteristic makes the LCG an attractive option for scenarios where speed is the primary priority, such as very large-scale simulations or real-time applications. Conversely, the CLCG algorithm incurs a higher computational cost due to its structure based on combining multiple LCG components. However, this additional overhead yields substantial gains in statistical quality and independence. The fact that the CLCG effectively eliminates the lattice structure in visual analyses and produces more robust results in statistical tests clearly illustrates that quality is achieved by sacrificing a degree of speed. In this context, the choice between LCG and CLCG depends heavily on the specific application domain. For simple simulations or preliminary computational processes where speed is critical and the quality of randomness is of secondary importance, the LCG may suffice. However, for long-duration simulations, engineering tasks, and scientific applications where statistical accuracy is paramount, the CLCG provides a much more reliable alternative. Ultimately, this balance established between performance and quality underscores the importance of selecting a pseudo-random number generator that is fit for purpose.

CONCLUSION

This study demonstrates that the selection of a PRNG in simulation projects is not merely a coding detail, but a critical design decision that directly impacts the validity and reliability of the model. The findings confirm that while the basic LCG offers speed advantages, its structural flaws most notably the lattice structure exhibited in multi-dimensional space render it insufficient for modern, high-precision simulations. Conversely, the CLCG approach, despite increasing computational overhead, successfully addresses these deficiencies by providing superior statistical accuracy and independence. In future research, a comparative analysis of the CLCG method against modern, high-performance algorithms such as the Mersenne Twister or Xorshift would provide a contemporary contribution to the literature. Furthermore, exploring the performance of these generators within parallel computing environments and GPU-based simulations remains a promising area for further investigation.

Ethical standard

The authors have no relevant financial or non-financial interests to disclose.

Availability of data and material

Not applicable.

Conflicts of interest

The authors declare that there is no conflict of interest regarding the publication of this paper.

LITERATURE CITED

AbdELHaleem, S. H., S. K. Abd-El-Hafiz, and A. G. Radwan, 2024 Analysis and guidelines for different designs of pseudo random number generators. IEEE Access **12**: 115697–115715.

Banks, J., 1998 *Handbook of simulation: principles, methodology, advances, applications, and practice*. John Wiley & Sons.

Banks, J., 2005 *Discrete event system simulation*. Pearson Education India.

Bhattacharjee, K. and S. Das, 2022 A search for good pseudo-random number generators: Survey and empirical studies. Computer Science Review **45**: 100471.

Gentle, J. E., 2003 *Random number generation and Monte Carlo methods*. Springer.

Hamming, R., 1952 Mathematical methods in large-scale computing units. Math Rev **13**: 495.

Johnston, D., 2018 *Random Number Generators—Principles and Practices: A Guide for Engineers and Programmers*. Walter de Gruyter GmbH & Co KG.

Knuth, D. E., 2014 *The art of computer programming: Seminumerical algorithms, volume 2*. Addison-Wesley Professional.

Kroese, D. P. and R. Y. Rubinstein, 2012 Monte carlo methods. Wiley Interdisciplinary Reviews: Computational Statistics **4**: 48–58.

Law, A. M., W. D. Kelton, and W. D. Kelton, 2007 *Simulation modeling and analysis*, volume 3. Mcgraw-hill New York.

L'ecuyer, P., 1988 Efficient and portable combined random number generators. Communications of the ACM **31**: 742–751.

L'ecuyer, P. and R. Simard, 2007 Testu01: Ac library for empirical testing of random number generators. ACM Transactions on Mathematical Software (TOMS) **33**: 1–40.

L'Ecuyer, P., 2011 Random number generation. In *Handbook of computational statistics: concepts and methods*, pp. 35–71, Springer.

Marsaglia, G., 1996 Diehard: a battery of tests of randomness. https://cir.nii.ac.jp/crid/1571698600935841152 .

Marsaglia, G., 2003 Xorshift rngs. Journal of Statistical software **8**: 1–6.

Matsumoto, M. and T. Nishimura, 1998 Mersenne twister: a 623-dimensionally equidistributed uniform pseudo-random number generator. ACM Transactions on Modeling and Computer Simulation (TOMACS) **8**: 3–30.

O'neill, M. E., 2014 Pcg: A family of simple fast space-efficient statistically good algorithms for random number generation. ACM Transactions on Mathematical Software **204**: 1–46.

Park, S. K. and K. W. Miller, 1988 Random number generators: good ones are hard to find. Communications of the ACM **31**: 1192–1201.

Rukhin, A., J. Soto, J. Nechvatal, M. Smid, and E. Barker, 2001 A statistical test suite for random and pseudorandom number generators for cryptographic applications. Technical report, NIST-SP-800-02.

Zio, E., 2012 Monte carlo simulation: The method. In *The Monte Carlo simulation method for system reliability and risk analysis*, pp. 19–58, Springer.

How to cite this article: Eldoğan, A. E., and Sevin, A. A Comparative Performance Analysis of Linear Congruential and Combined Linear Congruential Generators. *Chaos and Fractals*, 3(1), 21-28, 2026.

Licensing Policy: The published articles in CHF are licensed under a Creative Commons Attribution-NonCommercial 4.0 International License.

ADBA Chaos and Fractals
Cutting-Edge Scientific Solutions

e-ISSN: 3023-8951
RESEARCH ARTICLE
Vol.3 / No.1 / 2026 / pp.29-37
https://doi.org/10.69882/adba.chf.2026015

Nonlinear Dynamics and Chaos Control in a Discrete Sel'kov Model with Substrate Inhibition

Ansar Abbas *,1 **and Abdul Khaliq** *,2
*Department of Mathematics, Riphah International University, Lahore Campus, Pakistan.

ABSTRACT An investigation of the dynamic effects of substrate inhibition in a modified Sel'kov model of glycolytic oscillations is presented in this paper. With a saturated nonlinear term in place of classical polynomial feedback, the discrete-time formulation captures enzymatic regulation more realistically. It exhibits complicated dynamics, including period-doubling bifurcations, compared to the classical continuous Sel'kov model, which undergoes Hopf bifurcation. In this study, the model's behavior is investigated in multiple ways, including fixed point determination, stability assessment based on the Schur-Cohn criterion, and comprehensive numerical bifurcation analysis. Dynamic transitions from stability to periodic cycles, and then to chaos are revealed. Based on a comparative analysis with the classical model, we demonstrate how substrate inhibition induces complex nonlinear behavior through successive bifurcations. A deeper understanding of feedback regulation in biochemical systems can be gained from this study.

KEYWORDS
Discrete modified Sel'kov model
Substrate inhibition
Period-doubling bifurcation
Chaos control
Comparative dynamical analysis

INTRODUCTION

In cellular metabolism, glycolytic oscillations are characterized by periodic fluctuations in the concentrations of metabolites such as nicotinamide adenine dinucleotide (NADH) and adenosine triphosphate (ATP). Originally observed in yeast, these oscillations have now been identified in a variety of cell types, including pancreatic β-cells and cardiac myocytes (Goldbeter 1996; Fall *et al.* 2002). Apart from their role in metabolism, glycolytic oscillations also play a critical role in calcium signaling, circadian rhythms, and hormone production; particularly insulin (Bertram *et al.* 2007; Gaspers and Thomas 2000; Tornheim and Lowenstein 1979). Further, dysregulation of these oscillations is associated with metabolic diseases, including diabetes and cancer (Teusink *et al.* 2000; Richard 2003).

It has proven invaluable to use simplified mathematical models to investigate such rhythmic behavior. Among the most influential is the Sel'kov model (Sel'kov 1968), which encapsulates the nonlinear feedback dynamics responsible for glycolytic oscillations. Based on this model, complex dynamic phenomena have been investigated, such as enzyme kinetics, limit cycles, and bifurcation structures. Nonlinear dynamics and bifurcation theory are used for theoretical analysis (Strogatz 2015; Wiggins 2003; Kuznetsov 2004), focusing on Hopf bifurcation Hassard *et al.* (1981), explains how steady states become sustained oscillations as system parameters change. A variety of non-equilibrium thermodynamic platforms can be applied to these methods to clarify how feedback, autocatalysis, and dissipation produce oscillations and multistability (Schnakenberg 1979; Nicolis and Prigogine 1977).

Based on the following system of ordinary differential equations, Sel'kov describes in detail the dynamics of substrate and product concentrations during the phosphofructokinase reaction (PFK) in glycolysis:

$$\left.\begin{aligned} \frac{dx}{dt} &= \alpha - x + x^2 y, \\ \frac{dy}{dt} &= \beta - x^2 y, \end{aligned}\right\} \tag{1}$$

where $x(t)$ and $y(t)$ represent the concentrations of adenosine diphosphate (ADP) and adenosine triphosphate (ATP), respectively. The parameters α and β denote the external fluxes of ADP and ATP into the system. The nonlinear term x^2y introduces an autocatalytic interaction, capturing the feedback mechanism characteristic of the glycolytic pathway, in which ADP promotes further production of ATP.

Although this model is fundamental, it ignores substrate inhibition, which reduces enzyme activity when substrate concentrations are high. Typically, this inhibitory effect occurs when excess sub-

Manuscript received: 29 October 2025,
Revised: 7 January 2026,
Accepted: 9 January 2026.

[1]kute_ansar@yahoo.com (**Corresponding author**)
[2]khaliqsyed@gmail.com

strate molecules interfere with the efficiency of enzymes through the saturating of active sites or the activation of allosteric mechanisms. This biologically relevant behavior is incorporated by modifying the autocatalytic term to a saturated, rational form $\frac{x^2y}{1+\rho x^2}$, where $\rho > 0$ is the inhibition coefficient. The modified model thus becomes:

$$\left.\begin{aligned} \frac{dx}{dt} &= \alpha - x + \frac{x^2 y}{1+\rho x^2}, \\ \frac{dy}{dt} &= \beta - \frac{x^2 y}{1+\rho x^2}. \end{aligned}\right\} \tag{2}$$

In this modification, a saturation mechanism is introduced that limits the reaction rate at high substrate concentrations, in accordance with observed enzyme kinetics (Segel 1988; Murray 2002; Hofmeyr and Cornish-Bowden 1986). In some cases, continuous-time models are not adequate for capturing biological processes that involve discrete regulatory events, sampling intervals, or digital controls. Discrete-time models are more practical and insightful in such contexts (Elaydi 2005).

By applying a forward Euler discretization with step size $h > 0$, the system can be reformulated as a nonlinear difference equation:

$$\left.\begin{aligned} x_{n+1} &= x_n + h\left(\alpha - x_n + \frac{x_n^2 y_n}{1+\rho x_n^2}\right), \\ y_{n+1} &= y_n + h\left(\beta - \frac{x_n^2 y_n}{1+\rho x_n^2}\right). \end{aligned}\right\} \tag{3}$$

This discrete formulation preserves the essential nonlinear feedback and inhibition structure of the original system while enabling the study of a wider range of dynamic phenomena, including fixed points, bifurcations, and chaotic regimes (Guckenheimer and Holmes 1983; Alligood *et al.* 1996). Discrete-time approaches are especially suitable for modeling biochemical systems with threshold effects, delay responses, and pulse-driven behaviors (Chen *et al.* 2021; Elaydi 2005). We have also been able to improve our understanding of cellular function through the integration of mathematical modeling with systems biology. With the combination of quantitative models and experimental data, quantitative models can be used to design bioreactor control strategies and predict emergent behavior in complex networks (Heinrich and Schuster 1996; Glass and Mackey 1988; Bastin and Dochain 1990). Through educational frameworks, theoretical tools have been made accessible to researchers across disciplines, facilitating the application of mathematical biology (De Vries *et al.* 2006).

By representing feedback mechanisms in enzymatic reactions, Sel'kov's classical model has long served as a foundation for understanding these oscillations. A new model has been developed to capture the complexity of behaviors observed in biological systems in recent years. According to Sataric *et al.* (2024), diffusion is implicated in inducing symmetry breaking instabilities that might result in spatial homogeneity in concentrations of metabolites. Substrate inhibition, a phenomenon that inhibits enzyme activity at excessive substrate concentrations, is another critical factor affecting glycolysis. Yoshino *et al.* (2015) developed an analytical method to determine kinetic parameters of Allee Effect in metabolic pathways, emphasizing its prevalence and regulatory significance.

Glycolytic models with substrate inhibition reveal intricate dynamic behaviors, including bifurcations due to period-doubling. In such a system, bifurcations indicate transitions from stable oscillatory states to chaotic dynamics as parameters change. An analysis by Merdan and Duman (2022) demonstrated period-doubling bifurcations in a modified discrete-time model with substrate inhibition. In addition, Gambino *et al.* (2022) suggest that discrete-time frameworks benefit understanding the richness of biological rhythms as well as their susceptibility to chaos.

It is clear that classical models need to be refined to incorporate additional biological realism, such as substrate inhibition, so that nonlinear dynamics of glycolytic oscillations can be understood better. We analyze a modified Sel'kov model that integrates substrate inhibition in this paper, examining its dynamic behavior with a bifurcation analysis and comparing it with the original model to determine how this modification affects oscillation patterns and system stability.

Our work is novel because we include substrate inhibition into a discrete-time variant of the classical Sel'kov model to enhance its biological realism. With the proposed model, a rational inhibition term is incorporated within the autocatalytic feedback mechanism, accurately representing saturation behavior at high substrate concentrations. It is particularly important in computational and experimental contexts involving sampled data to be able to analyze bifurcation structures and oscillation patterns by discretizing the modified system.

An important aspect of this study is the analysis and numerical exploration of the model's fixed points and local dynamics, with a focus on identifying bifurcation conditions. In addition, we perform a local reduction of the system near critical bifurcation points by using center manifold theory, allowing us to comprehend nonlinear behavior near stability thresholds more deeply. This work provides a novel approach to modeling enzymatic feedback with substrate inhibition in discrete-time settings, shedding new light on mechanisms governing metabolic stability and oscillations. Consequently, the inclusion of substrate inhibition allows the model to exhibit complex bifurcation and chaotic dynamics that are not captured by the classical discrete Sel'kov framework.

The objective of this study was to develop a discrete-time adaptation of the classical Sel'kov model, enhanced with saturated inhibitory feedback. The paper is organized as follows. In Section *Equilibrium Point and Stability Analysis*, we analyze the system's fixed point's existence and local stability. By employing the Schur-Cohn criterion, it is shown that a unique fixed point exists, and its stability is investigated. By implementing a state feedback control strategy, the marginal stability region associated with the chaotic behavior of System 4 has been identified, as elaborated in Section *Chaos control*. The trajectories of eigenvalues are explored in Section *Numerical Analysis*, where period-doubling bifurcations are identified, leading to the emergence of cyclic and chaotic dynamics. Section *Global Bifurcation Overview for* $\beta \in [1, 100]$ presents a comprehensive global bifurcation analysis within the interval $\beta \in [1, 100]$, highlighting the transitions between stability and periodicity. In Section *Comparative Discussion with the Classical Sel'kov Model*, we compare the classical continuous Sel'kov model with the proposed discrete model with saturated feedback in detail. A table summarizing dynamic features, bifurcation behavior, computational aspects, and biological implications is provided. To conclude, Section *Conclusion* summarizes the core analytical and numerical insights of the paper, emphasizing how discrete modeling and saturation contribute to rich dynamical phenomena in biochemical systems.

EQUILIBRIUM POINT AND STABILITY ANALYSIS

We examine the discrete-time model obtained using the forward Euler method from a biologically inspired glycolytic system with substrate inhibition. In this context, the proposed model is pre-

sented below, with the corresponding state variables and parameters detailed in Table 1.

$$\left.\begin{aligned} x_{n+1} &= x_n + h\left(\alpha - x_n + \frac{x_n^2 y_n}{1+\rho x_n^2}\right), \\ y_{n+1} &= y_n + h\left(\beta - \frac{x_n^2 y_n}{1+\rho x_n^2}\right), \end{aligned}\right\} \tag{4}$$

Table 1 State variables and parameters of the discrete model and their role

State variables	
x_n	Concentration of **ADP** (adenosine diphosphate) at discrete time step n. Contributes to glycolysis processes catalyzed by phosphofructokinase (PFK).
y_n	Concentration of **ATP** (adenosine triphosphate) at discrete time step n. Represents the reaction product.
Parameters	
α	Constant inflow or supply rate of ADP. Indicates how much substrate is being imported or produced externally.
β	Constant inflow or supply rate of ATP. Represents the baseline energy or production level at which the system operates.
ρ	Substrate inhibition coefficient. Higher values indicate stronger inhibition due to enzyme saturation at high ADP concentrations.
h	Discrete time step size. Determines the temporal resolution of the simulation in forward Euler discretization.

Existence of Fixed Points

A fixed point $(\tilde{x}, \tilde{y})$ of the system satisfies $x_{n+1} = x_n = \tilde{x}$ and $y_{n+1} = y_n = \tilde{y}$. Substituting into Eq. (4), we obtain the steady-state conditions:

$$\left.\begin{aligned} \tilde{x} &= \tilde{x} + h\left(\alpha - \tilde{x} + \frac{\tilde{x}^2\tilde{y}}{1+\rho\tilde{x}^2}\right), \\ \tilde{y} &= \tilde{y} + h\left(\beta - \frac{\tilde{x}^2\tilde{y}}{1+\rho\tilde{x}^2}\right). \end{aligned}\right\} \tag{5}$$

Subtracting $\tilde{x}$ and $\tilde{y}$ from both sides yields:

$$\left.\begin{aligned} 0 &= \alpha - \tilde{x} + \frac{\tilde{x}^2\tilde{y}}{1+\rho\tilde{x}^2}, \\ 0 &= \beta - \frac{\tilde{x}^2\tilde{y}}{1+\rho\tilde{x}^2}. \end{aligned}\right\} \tag{6}$$

From the second equation in (6), we solve for $\tilde{y}$:

$$\frac{\tilde{x}^2\tilde{y}}{1+\rho\tilde{x}^2} = \beta \quad \Rightarrow \quad \tilde{y} = \beta \cdot \frac{1+\rho\tilde{x}^2}{\tilde{x}^2}, \quad \tilde{x} \neq 0. \tag{7}$$

Substitute $\tilde{y}$ into the first equation of (6) gives:

$$0 = \alpha - \tilde{x} + \frac{\tilde{x}^2}{1+\rho\tilde{x}^2} \cdot \frac{(1+\rho\tilde{x}^2)\beta}{\tilde{x}^2} = \alpha - \tilde{x} + \beta. \tag{8}$$

Hence, we find:

$$\tilde{x} = \alpha + \beta.$$

Using this in Eq. (7), we obtain:

$$\tilde{y} = \frac{(1+\rho(\alpha+\beta)^2)\beta}{(\alpha+\beta)^2}.$$

Therefore, the system has a unique biologically meaningful fixed point $(\tilde{x}, \tilde{y})$ given by:

$$(\tilde{x}, \tilde{y}) = \left(\alpha+\beta,\ \frac{(1+\rho(\alpha+\beta)^2)\beta}{(\alpha+\beta)^2}\right). \tag{9}$$

This fixed point exists and is positive for all $\alpha, \beta > 0$ and $\rho \geq 0$, satisfying the biochemical requirement that metabolite concentrations must remain non-negative.

Stability Analysis via Schur–Cohn Conditions

To investigate the local stability of the nontrivial equilibrium point of the system, we compute the Jacobian matrix and apply the Schur–Cohn stability conditions for discrete-time two-dimensional systems. Let us define:

$$f(x,y) = x + h\left(\alpha - x + \frac{x^2 y}{1+\rho x^2}\right), \quad g(x,y) = y + h\left(\beta - \frac{x^2 y}{1+\rho x^2}\right).$$

We now compute the Jacobian matrix $\tilde{J}$:

$$J = \begin{bmatrix} \frac{\partial f}{\partial x} & \frac{\partial f}{\partial y} \\ \frac{\partial g}{\partial x} & \frac{\partial g}{\partial y} \end{bmatrix}\Bigg|_{(\tilde{x},\tilde{y})}. \tag{10}$$

Define:

$$R(x,y) = \frac{x^2 y}{1+\rho x^2}.$$

Here,

$$\frac{\partial f}{\partial x} = 1 + h\left(-1 + \frac{\partial R}{\partial x}\right), \quad \frac{\partial f}{\partial y} = h\left(\frac{\partial R}{\partial y}\right).$$

and

$$\frac{\partial g}{\partial x} = -h\left(\frac{\partial R}{\partial x}\right), \quad \frac{\partial g}{\partial y} = 1 - h\left(\frac{\partial R}{\partial y}\right).$$

Compute:

$$\frac{\partial R}{\partial x} = \frac{2xy(1+\rho x^2) - x^2 y(2\rho x)}{(1+\rho x^2)^2} = \frac{2xy(1+\rho x^2) - 2\rho x^3 y}{(1+\rho x^2)^2},$$

$$\frac{\partial R}{\partial x} = \frac{2xy(1+\rho x^2 - \rho x^2)}{(1+\rho x^2)^2} = \frac{2xy}{(1+\rho x^2)^2},$$

$$\frac{\partial R}{\partial y} = \frac{x^2}{1+\rho x^2}.$$

So the Jacobian becomes:

$$\tilde{J} = \begin{bmatrix} 1 + h\left(-1 + \frac{\partial R}{\partial x}\right) & h \cdot \frac{\partial R}{\partial y} \\ -h \cdot \frac{\partial R}{\partial x} & 1 - h \cdot \frac{\partial R}{\partial y} \end{bmatrix}.$$

Let:

$$r = \frac{\partial R}{\partial y}\Big|_{(\tilde{x},\tilde{y})} = \frac{\tilde{x}^2}{1+k\tilde{x}^2}, \quad s = \frac{\partial R}{\partial x}\Big|_{(\tilde{x},\tilde{y})} = \frac{2\tilde{x}\tilde{y}}{(1+\rho\tilde{x}^2)^2}.$$

Then:

$$\tilde{J} = \begin{bmatrix} 1 + h(-1+s) & hr \\ -hs & 1 - hr \end{bmatrix}.$$

Definition 1 (Schur-Cohn Criterion (Elaydi 2005))**.** Let J be the Jacobian matrix of a two-dimensional discrete dynamical system evaluated at a fixed point:

$$J = \begin{bmatrix} a_{11} & a_{12} \\ a_{21} & a_{22} \end{bmatrix},$$

with trace and determinant given by

$$\mathrm{tr}(J) = a_{11} + a_{22}, \quad \det(J) = a_{11}a_{22} - a_{12}a_{21}.$$

Then, the stability of the fixed point is determined by the following conditions:

- **Asymptotically Stable :** The fixed point is asymptotically stable if and only if the following three inequalities hold:

$$\begin{aligned} 1 - \mathrm{tr}(J) + \det(J) &> 0, \\ 1 + \mathrm{tr}(J) + \det(J) &> 0, \\ |\det(J)| &< 1. \end{aligned}$$

- **Unstable:** At least one of the following holds:

$$\begin{aligned} 1 - \mathrm{tr}(J) + \det(J) &< 0, \\ 1 + \mathrm{tr}(J) + \det(J) &< 0, \\ |\det(J)| &\geq 1. \end{aligned}$$

- **Borderline Cases (Bifurcations May Occur):** Fixed point lies on the boundary of the unit circle by $|\det(J)| = 1$. It is possible to get a bifurcation depending on the other properties. Inequalities become equals in the following ways:

$$1 - \mathrm{tr}(J) + \det(J) = 0, \quad \text{or} \quad 1 + \mathrm{tr}(J) + \det(J) = 0.$$

The trace is:

$$\mathrm{tr}(\tilde{J}) = (1 + h(-1 + s)) + (1 - hr) = 2 + h(s - r - 1).$$

The determinant is:

$$\begin{aligned} \det(\tilde{J}) &= (1 + h(-1 + s))(1 - hr) + h^2 sr \\ &= (1 - h + hs)(1 - hr) + h^2 sr \\ &= (1 - h)(1 - hr) + hs(1 - hr) + h^2 sr \\ &= (1 - h)(1 - hr) + hs \\ &= 1 - hr - h + h^2 r + hs \\ &= 1 - h(1 + r) + h^2 r + hs \end{aligned}$$

Thus,

$$\boxed{\det(\tilde{J}) = 1 - h(1 + r) + h^2 r + hs}.$$

and

$$\boxed{\mathrm{tr}(\tilde{J}) = 2 + h(s - r - 1)}.$$

Substitute the symbolic forms:

$$\begin{aligned} \mathbf{SC}_1 &\Leftrightarrow 1 - [2 + h(s - r - 1)] + \left[1 - h(1 + r) + h^2 r + hs\right] > 0, \\ \mathbf{SC}_2 &\Leftrightarrow 1 + [2 + h(s - r - 1)] + \left[1 - h(1 + r) + h^2 r + hs\right] > 0, \\ \mathbf{SC}_3 &\Leftrightarrow \left|1 - h(1 + r) + h^2 r + hs\right| < 1. \end{aligned}$$

These inequalities define a region in the parameter space (α, β, ρ, h) for which the fixed point is locally asymptotically stable.

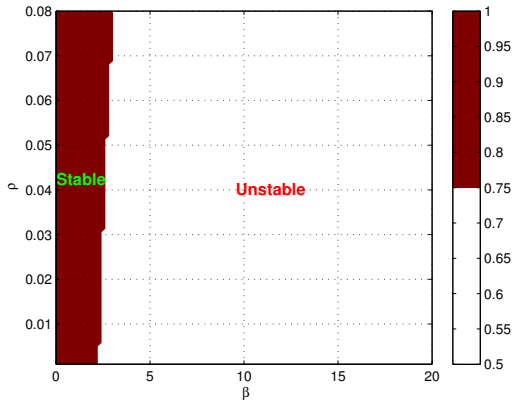

(a) (β, ρ) plane

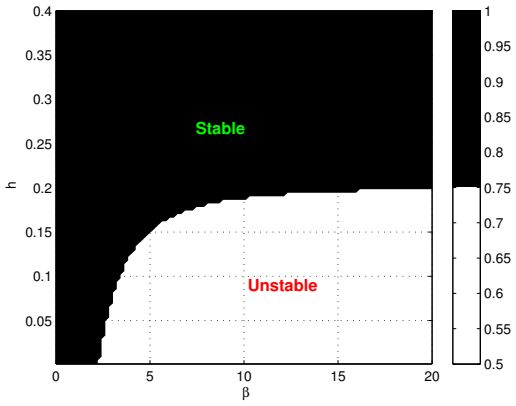

(b) (β, h) plane

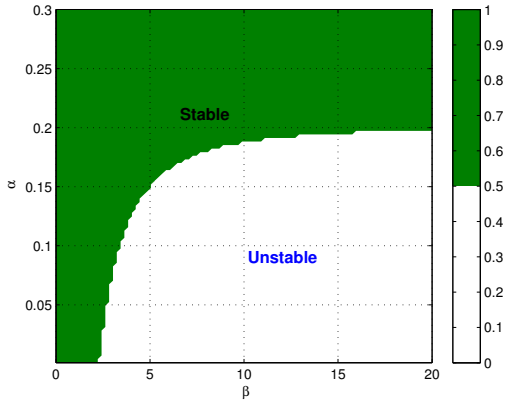

(c) (β, α) plane

Figure 1 Illustration of stability regions: (a) (β, ρ) with $\alpha = 0.3$ and $h = 0.4$ (1a), (b) (β, h) with $\alpha = 0.3$ and $\rho = 0.08$ (1b), and (c) (β, α) with $h = 0.4$ and $\rho = 0.08$ (1c). In all cases, β varies from 1 to 20.

CHAOS CONTROL

In this section, we examine chaos control via state feedback (Elaydi 2005; Abbas and Khaliq 2023). First, we will discuss marginal stability for completeness.

Definition 2. In a marginally stable system, neither stability nor instability are present, but just exist between them. Small perturbations have the potential to make an unstable system.

We have the following discrete biological model (4):

$$\left.\begin{aligned} x_{n+1} &= x + h\left(\alpha - x + \frac{x^2 y}{1+\rho x^2}\right) \\ &\quad - p(x - \alpha - \beta) \\ &\quad - q\left(y - \frac{\beta + \alpha^2\beta\rho + 2\alpha\beta^2\rho + \beta^3\rho}{(\alpha+\beta)^2}\right), \\ y_{n+1} &= y + h\left(\beta - \frac{x^2 y}{1+\rho x^2}\right) \end{aligned}\right\} \tag{11}$$

Control is added by the addition of

$$w_n = -p(x - \alpha - \beta) - q\left(y - \frac{\beta + \alpha^2\beta\rho + 2\alpha\beta^2\rho + \beta^3\rho}{(\alpha+\beta)^2}\right)$$

, with p, q indicating feedback gains. The following map is used to evaluate the variational matrix J_P at the interior fixed point P:

$$(G, H) \longmapsto (x_{n+1}, y_{n+1}) \tag{12}$$

Where

$$\left.\begin{aligned} G: &= x + h\left(\alpha - x + \frac{x^2 y}{1+\rho x^2}\right) \\ &\quad - p(x - \alpha - \beta) \\ &\quad - q\left(y - \frac{\beta + \alpha^2\beta\rho + 2\alpha\beta^2\rho + \beta^3\rho}{(\alpha+\beta)^2}\right), \\ H: &= y + h\left(\beta - \frac{x^2 y}{1+\rho x^2}\right) \end{aligned}\right\} \tag{13}$$

$$J_P = \begin{pmatrix} 1 - p + h\left(-1 - \frac{2kx^3y}{(1+kx^2)^2} + \frac{2xy}{1+kx^2}\right) & -q + \frac{hx^2}{1+kx^2} \\ h\left(\frac{2kx^3y}{(1+kx^2)^2} - \frac{2xy}{1+kx^2}\right) & 1 - \frac{hx^2}{1+kx^2} \end{pmatrix}$$

λ_1, λ_2 represent the characteristic root of J_P at P, then

$$\begin{aligned} \lambda_1 + \lambda_2 = &- \frac{1}{\alpha+\beta+(\alpha+\beta)^3\rho}\Big[\alpha^3\left(h(1+\rho)+\rho(-2+p)\right) \\ &+ 3\alpha^2\beta\left(h(1+\rho)+\rho(-2+p)\right) \\ &+ \beta\left(h(-1+\beta^2(1+\rho)) + (1+\beta^2\rho)(-2+p)\right) \\ &+ \alpha\left(h(1+3\beta^2(1+\rho)) + (1+3\beta^2\rho)(-2+p)\right)\Big] \end{aligned} \tag{14}$$

$$\begin{aligned} \lambda_1 \cdot \lambda_2 = &\frac{1}{\alpha+\beta+(\alpha+\beta)^3\rho}\Big[\alpha(-1+3\beta^2(h-\rho))(-1+h+p) \\ &+ \alpha^3(h-\rho)(-1+h+p) \\ &+ 3\alpha^2\beta(h-\rho)(-1+h+p) \\ &+ \beta\Big(\beta^2h^2 - (1+\beta^2\rho)(-1+p) \\ &- h\left(-1+\beta^2(1+\rho-p)+2q\right)\Big)\Big] \end{aligned} \tag{15}$$

According to equations (14) and (15), marginal stability lines can be found ($\lambda_1 = \pm 1$ and $\lambda_1\lambda_2 = 1$). It ensures that the moduli of the eigenvalues are less than 1.

When $\lambda_1\lambda_2 = 1$, then from Eq. (14), we can get

$$\begin{aligned} L_1: = &\frac{\alpha(-1+3\beta^2(h-\rho)) + \alpha^3(h-\rho) + 3\alpha^2\beta(h-\rho)}{\alpha+\beta+(\alpha+\beta)^3\rho}(-1+h+p) \\ &+ \frac{\beta\Big(\beta^2h^2 - (1+\beta^2\rho)(-1+p) - h\left(-1+\beta^2(1+\rho-p)+2q\right)\Big)}{\alpha+\beta+(\alpha+\beta)^3\rho} - 1 = 0 \end{aligned} \tag{16}$$

When $\lambda_1 = 1$, then from Eq. (13) and Eq. (14), we can get

$$L_2: \frac{(\alpha+\beta)^3h(h+p) - 2\beta hq}{\alpha+\beta+(\alpha+\beta)^3\rho} = 0 \tag{17}$$

When $\lambda_1 = -1$, then from Eq. (13) and Eq. (14), we can get

$$\begin{aligned} L_3: = &\frac{\alpha(-2+3\beta^2(h-2\rho)) + \alpha^3(h-2\rho) + 3\alpha^2\beta(h-2\rho)}{\alpha+\beta+(\alpha+\beta)^3\rho}(-2+h+p) \\ &+ \frac{\beta\Big(\beta^2h^2 - 2(1+\beta^2\rho)(-2+p) + h\left(2+\beta^2(-2-2\rho+p)-2q\right)\Big)}{\alpha+\beta+(\alpha+\beta)^3\rho} = 0 \end{aligned} \tag{18}$$

The triangular region obtained by combining equations (16), (17) and (18) reveals that $|\lambda_{1,2}| < 1$.

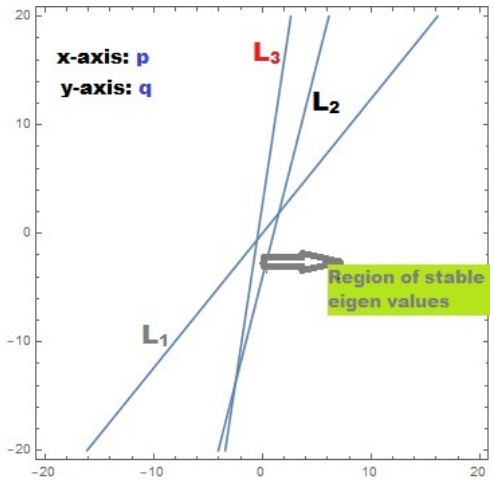

Figure 2 Region of stability where $|\lambda_{1,2}| < 1$

NUMERICAL ANALYSIS

Using the bifurcation parameter range $\beta \in [1, 20]$, we carried out a detailed numerical analysis of the system (4). There is a complex pattern of dynamic transition as shown in Figure 3. It exhibits a stable fixed point starting at a low value of $\beta = 1$ and gradually increasing up to $\beta \approx 2$. There is a steady state for both x_n and y_n on account of the convergence of their trajectories. In response to increasing β, particularly at $\beta \approx 3{-}4$, the fixed point destabilizes, giving rise to periodic behavior through the classical period-doubling bifurcation, leading to stable 2-cycles and eventually 4-cycles. A chaotic dynamic is observed as the system progresses upward between approximately $\beta = 6$ to $\beta = 9$. It is characterized by irregular, non-repeating patterns and a strong dependence on initial conditions. Periodic windows interrupt the chaotic region, such as around $\beta \approx 6.7$, where the system temporarily returns to a stable periodic orbit before re-entering chaos. After $\beta = 10$, this periodic-chaotic pattern continues. The

behavior becomes chaotic once again in the interval $\beta = 16-19$ following regular cycles in the interval $\beta = 13-15$.

Specifically, the system (4) in $\beta \in [1, 20]$ demonstrates a delicate interaction between periodicity, stability, and chaos. The numerical simulations captured in Figures 3 and 4 provide a compelling visualization of this bifurcation structure.

In order to control the chaotic behavior of the system (4), we have used the state feedback control method. To verify the validity of our results, we will proceed to Section (4). The values of $\alpha = 0.3$, $h = 0.4$, $\rho = 0.08$ and $\beta = 3.18$ can be used to obtain (15), (16), and (17).

$$L_1: = -1 + 0.145953\Big(2.89576(-0.6+p) + 3.18\Big(1.61798 - 1.80899(-1+p) - 0.4\big(-1 + 10.1124(1.08-p) + 2q\big)\Big)\Big) = 0 \tag{19}$$

$$L_2: \; 0.145953\big(16.8577(0.4+p) - 2.544q\big) = 0 \tag{20}$$

$$L_3: = 0.145953\Big(1.79682(-1.6+p) + 3.18\Big(1.61798 - 3.61798(-2+p) + 0.4\big(2 + 10.1124(-2.16+p) - 2q\big)\Big)\Big) = 0 \tag{21}$$

Equations (19), (20), and (21) describe lines that intersect to form a triangular region corresponding to $|\Lambda_{1,2}| < 1$, as shown in Figure 2.

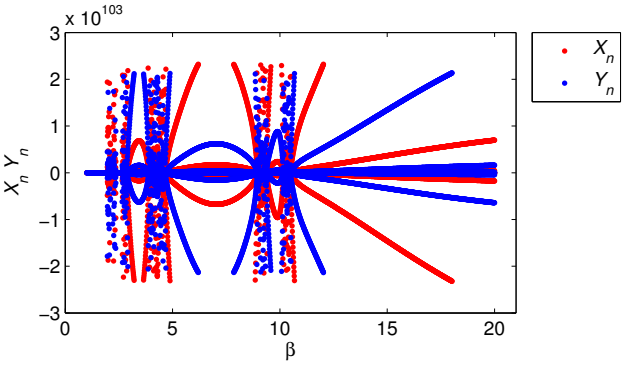

Figure 3 Bifurcation diagram of the system (4) showing the variation in x_n (red) and y_n (blue) w.r.t bifurcation parameter β. The diagram captures transitions from stability to chaos and divergence.

GLOBAL BIFURCATION OVERVIEW FOR $\beta \in [1, 100]$

The bifurcation structure of system (4) reveals intricate and diverse dynamical behavior as the bifurcation parameter β ranges from 1 to 100. As illustrated in Figure 5, the system undergoes a series of transitions among stable states, periodic oscillations, and chaotic regimes, depending on the value of β. This diagram captures the long-term evolution of the system's state variables, highlighting the sensitivity and richness of its nonlinear dynamics.

Table 2 shows that system (4) does not exhibit a monotonic transition from stability to chaos over the interval $\beta \in [1, 100]$. Instead, the dynamics follow the sequence:

$$\text{Stable} \to \text{Cyclic} \to \text{Chaotic} \to \text{Periodic window} \to \text{Chaotic} \to \text{Unstable}.$$

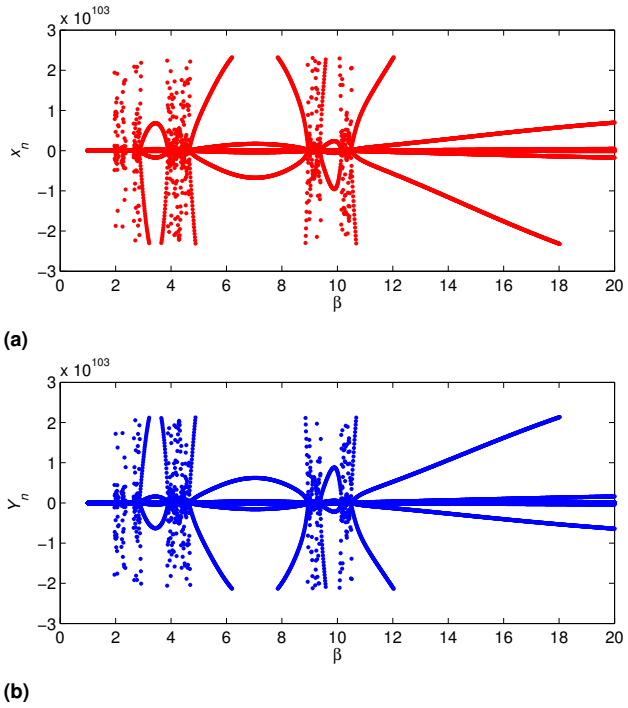

Figure 4 Bifurcation diagrams of system (4) with respect to the bifurcation parameter β: Figure 4a shows transitions in x_n , while Figure 4b shows transitions in y_n. The diagrams capture the progression from stability to chaos and eventual divergence.

Table 2 Dynamical behavior of the system as β varies

Interval for β	Behavior Type	Description
1−2, 10−12, 20−22	Point of stability	The system reaches an equilibrium state when both x_n and y_n converge.
3−4, 13−15, 23−25	Doubling the period	Onset of periodic oscillations with 2-cycles and 4-cycles as the fixed point becomes unstable.
6−9, 16−19, 26−30	Dynamics of chaos	Evolution dominated by irregular, non-repeatable trajectories dependent upon the initial conditions.
∼ 38, 48, 68	Periodic windows	Regular cycles reappear within chaotic regimes (e.g., period-3, period-6), indicating pockets of order.
> 90	Divergent/Unstable	Unlimited growth; trajectories may diverge or exhibit instability beyond attractor boundaries.

The recursive dynamics of system (4) arise from its inherent non-linearity and saturated feedback structure. As the parameter β increases, the system exhibits growing sensitivity to parameter changes. This behavior is visually captured in the bifurcation diagram shown in Figure 5, which clearly marks the onset of bifur-

cations and the progressive emergence of complex dynamics from initially simple evolution rules.

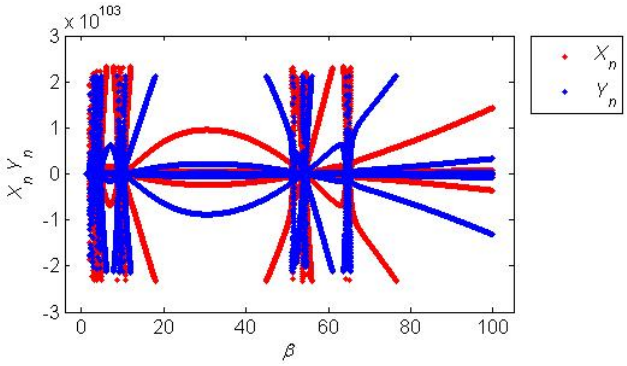

Figure 5 Bifurcation diagram of the system (4) displaying the long-term behavior of x_n (red) and y_n (blue) as the bifurcation parameter β varies over the interval $[1, 100]$. The diagram highlights the onset of complex dynamics, including period-doubling bifurcations, multistability, and chaotic oscillations induced by substrate inhibition effects.

COMPARATIVE DISCUSSION WITH THE CLASSICAL SEL'KOV MODEL

The classical Sel'kov model, formulated in continuous time as a system of ordinary differential equations (ODEs), has been extensively studied as a minimal model for glycolytic oscillations. It is known for its ability to capture sustained oscillations via Hopf bifurcations and its relatively simple nonlinear structure, which has made it a benchmark in biochemical dynamics studies. However, the original formulation lacks explicit mechanisms for inhibitory feedback, a limitation when modeling biochemical systems in which enzyme activity is reduced at high substrate concentrations.

In this work, we have developed a discrete-time variant of the Sel'kov model that explicitly incorporates substrate inhibition through nonlinear feedback terms. This modification is motivated by biological observations of saturation effects in enzymatic reactions, particularly in systems regulated through pulse-like inputs, switch-like transitions, or temporally sampled external control. The discrete formulation allows for a natural representation of such regulatory mechanisms and provides a framework for analyzing the interplay between time discretization and nonlinear biochemical feedback.

To facilitate a direct comparison between the two approaches, we summarize the key differences in Table 3. The comparison covers model formulation, biological interpretation, dynamical behavior, stability analysis, and the use of chaos control techniques.

The comparison highlights clear distinctions between the two formulations. The discrete Sel'kov model extends the classical framework by incorporating an inhibitory feedback mechanism absent in the continuous counterpart, broadening applicability to systems where inhibition is biologically relevant. This addition enriches the dynamical repertoire, allowing phenomena such as period-doubling cascades and chaotic regimes behaviors unattainable in the original model, which is limited to Hopf-induced oscillations. Stability requirements also differ: the continuous model demands eigenvalues with negative real parts, whereas the discrete form relies on the Schur–Cohn condition, making stability more sensitive to discretization step size and parameter variations. Furthermore, the discrete framework enables direct chaos-control

Table 3 Comparison between the classical continuous-time Sel'kov model and the proposed discrete-time Sel'kov model with substrate inhibition

Aspect	Classical Continuous Sel'kov Model	Proposed Discrete Sel'kov Model with Substrate Inhibition
Model Formulation and Mechanism		
Mathematical Formulation	ODE system without inhibitory terms in the reaction kinetics.	Discrete-time system incorporating nonlinear substrate inhibition directly in the reaction terms.
Biological Representation	Captures continuous metabolic flows; assumes no enzyme inhibition.	Represents saturation effects and enzyme inhibition; suited for pulse-like or discrete regulatory mechanisms.
Dynamical Behavior		
Typical Dynamics	Stable fixed points; oscillations via Hopf bifurcation.	Rich dynamics including bifurcation cascades, chaotic windows, and marginal stability zones.
Bifurcation Features	Hopf bifurcations produce stable limit cycles for specific parameters.	Period-doubling route to chaos as β increases ($\alpha = 0.3$, $h = 0.4$, $\rho = 0.08$).
Stability Analysis		
Criterion	Stability if all Jacobian eigenvalues have negative real parts.	Stability via Schur–Cohn criterion: eigenvalues must lie inside the unit circle; sensitive to step size and parameter changes.
Control and Applications		
Chaos Control	Typically not addressed in the literature.	Linear state feedback control stabilizes chaotic trajectories ($\beta = 3.18$).
Biological Relevance	May miss discrete regulatory effects such as switching or pulse signaling.	Well-suited for modeling time-sampled regulation and discrete biochemical events.

strategies; for example, linear state feedback can stabilize chaotic trajectories and restore fixed-point behavior in marginally stable regimes, offering practical regulation methods for synthetic biochemical systems. Biologically, the discrete model better captures processes with inherently discrete operation such as periodic forcing, signal gating, or digital biochemical circuits—while the continuous model, though effective for smooth flows, lacks inhibitory representation and cannot model saturation-driven nonlinearities. Overall, the discrete Sel'kov model with substrate inhibition offers a more versatile and insightful framework for exploring complex dynamics and implementing control strategies in nonlinear biochemical systems where discrete regulation and inhibition are central. Incorporating substrate inhibition, which reduces enzyme activity at high substrate levels, gives the model a more realistic enzymatic regulation and overcomes a key limitation of the classical Sel'kov model.

CONCLUSION

We established and studied a discrete-time model by modifying Sel'kov glycolysis with a nonlinear feedback saturation term incorporating substrate inhibition. By accounting for regulatory mechanisms frequently observed in enzymatic reactions, this modification enhances the model's biological relevance, while the discrete-time formulation allows for an examination of dynamics under

iterative updates, which is particularly relevant for numerical simulations and biological pulsed systems. This study exclusively utilizes the proposed discrete-time model for its analytical and numerical results. The chaotic dynamics were observed in the system (4) with parameter values of $\alpha = 0.3$, $h = 0.4$, and $\rho = 0.08$, with bifurcation parameter β in the range $[0, 20]$, as a cascade of period-doubling bifurcations occurred. There are classical routes to chaos in discrete nonlinear systems, and these transitions suggest our model captures deeper dynamics than simple fixed points. Further, we successfully applied the state feedback strategy to control the chaotic behavior of the proposed system, as shown in Figure-2 . Despite our reference to the continuous-time Sel'kov model to explain Hopf bifurcations and limit cycles, we did not include any simulations or results from the unmodified Sel'kov model. There is no period-doubling route to chaos within the continuous model, unlike discrete dynamics. Thus, the comparison highlights the novel behaviors introduced by our feedback mechanism and discrete-time formulation.

Additionally, we demonstrated chaos control with our model. Specifically, the system can be stabilized at its unique fixed point by appropriate parameter tuning at $\beta = 3.18$, which lies within a region of marginal stability. This result showcases the potential for implementing simple yet effective control strategies in discrete biochemical systems where oscillatory or chaotic behaviors may be undesirable. Although no new experiments were conducted, the model's oscillatory and chaotic behaviors align with reported glycolytic oscillations, suggesting it captures dynamics relevant to real biochemical systems. Overall, the discrete-time model with substrate inhibition offers a robust and flexible framework to explore nonlinear behaviors in biochemical systems. By preserving basic dynamics of the classical Sel'kov model, it introduces new phenomena that are relevant to both theoretical and applied studies, such as period-doubling bifurcations and controllable chaos. Developing hybrid models that integrate continuous metabolic dynamics with discrete regulatory mechanisms may enhance the model's applicability in systems biology and synthetic biochemical circuit design in the future.

Future extensions may improve the model's representation of biological systems. These include introducing stochastic fluctuations to capture random variability, linking multiple oscillators to study coordinated dynamics, or incorporating stochastic enzyme kinetics to reflect molecular-level variability. Such developments would provide deeper insight into complex biochemical behaviors and expand the model's potential applications in systems biology and synthetic circuits.

Acknowledgments

There is no specific funding assigned to this research.

Ethical standard

The authors have no relevant financial or non-financial interests to disclose.

Availability of data and material

All data used in this manuscript are properly cited.

Conflicts of interest

The authors declare that there is no conflict of interest regarding the publication of this paper.

LITERATURE CITED

Abbas, A. and A. Khaliq, 2023 Analyzing predator–prey interaction in chaotic and bifurcating environments. Chaos Theory and Applications **5**: 207–218.

Alligood, K. T., T. D. Sauer, and J. A. Yorke, 1996 *Chaos: An Introduction to Dynamical Systems*. Springer, New York.

Bastin, G. and D. Dochain, 1990 *On-line Estimation and Adaptive Control of Bioreactors*. Elsevier, Amsterdam.

Bertram, R., L. S. Satin, M. Zhang, P. Smolen, and A. Sherman, 2007 Metabolic and electrical oscillations: partners in controlling pulsatile insulin secretion. American Journal of Physiology-Endocrinology and Metabolism **293**: E890–E900.

Chen, L., R. Wang, and K. Aihara, 2021 Nonlinear dynamical systems in biology: Analysis and control. Annual Review of Biomedical Engineering **23**: 75–106.

De Vries, G., T. Hillen, M. Lewis, J. Muller, and B. Schonfisch, 2006 *A Course in Mathematical Biology: Quantitative Modeling with Mathematical and Computational Methods*. SIAM, Philadelphia.

Elaydi, S., 2005 *An Introduction to Difference Equations*. Springer, New York, third edition.

Fall, C. P., E. S. Marland, J. M. Wagner, and J. J. Tyson, 2002 *Computational Cell Biology*. Springer, New York.

Gambino, G., M. C. Lombardo, and M. Sammartino, 2022 Discrete dynamical modeling of ecological and biological systems. Mathematics **10**: 1154.

Gaspers, L. D. and A. P. Thomas, 2000 Mitochondrial metabolism of pyruvate is required for glucose-stimulated insulin secretion and is regulated by calcium in β-cells. Molecular and Cellular Endocrinology **167**: 1–10.

Glass, L. and M. C. Mackey, 1988 *From Clocks to Chaos: The Rhythms of Life*. Princeton University Press, Princeton.

Goldbeter, A., 1996 *Biochemical Oscillations and Cellular Rhythms: The Molecular Bases of Periodic and Chaotic Behaviour*. Cambridge University Press, Cambridge.

Guckenheimer, J. and P. Holmes, 1983 *Nonlinear Oscillations, Dynamical Systems, and Bifurcations of Vector Fields*. Springer, New York.

Hassard, B. D., N. D. Kazarinoff, and Y.-H. Wan, 1981 *Theory and Applications of Hopf Bifurcation*. Cambridge University Press, Cambridge.

Heinrich, R. and S. Schuster, 1996 *The Regulation of Cellular Systems*. Springer, New York.

Hofmeyr, J.-H. S. and A. Cornish-Bowden, 1986 The thermodynamic basis of metabolic control analysis. European Journal of Biochemistry **155**: 265–270.

Kuznetsov, Y. A., 2004 *Elements of Applied Bifurcation Theory*. Springer, New York, third edition.

Merdan, H. and O. Duman, 2022 Stability and period-doubling bifurcation in a modified commensal symbiosis model with allee effect. Mathematical Modelling of Natural Phenomena **17**: 1–16.

Murray, J. D., 2002 *Mathematical Biology I: An Introduction*. Springer, New York, third edition.

Nicolis, G. and I. Prigogine, 1977 *Self-Organization in Nonequilibrium Systems: From Dissipative Structures to Order through Fluctuations*. Wiley, New York.

Richard, P., 2003 Metabolic regulation: a precision-control mechanism of the cell. Biochemical Journal **375**: 1–16.

Sataric, M. V., T. Nemes, and J. A. Tuszynski, 2024 Re-examination of the sel'kov model of glycolysis and its symmetry-breaking instability due to diffusion. Biophysica **4**: 545–560.

Schnakenberg, J., 1979 Simple chemical reaction systems with limit cycle behaviour. Journal of Theoretical Biology **81**: 389–400.

Segel, L. A., 1988 *Modeling Dynamic Phenomena in Molecular and Cellular Biology*. Cambridge University Press, Cambridge.

Sel'kov, E. E., 1968 Self-oscillations in glycolysis: I. a simple kinetic model. European Journal of Biochemistry **4**: 79–86.

Strogatz, S. H., 2015 *Nonlinear Dynamics and Chaos: With Applications to Physics, Biology, Chemistry, and Engineering*. CRC Press, Boca Raton, second edition.

Teusink, B. *et al.*, 2000 Can yeast glycolysis be understood in terms of in vitro kinetics of the constituent enzymes? testing biochemistry. European Journal of Biochemistry **267**: 5313–5329.

Tornheim, K. and J. M. Lowenstein, 1979 Oscillations of glycolysis in yeast: evidence for an atp-initiated feedback system. Proceedings of the National Academy of Sciences of the USA **76**: 6602–6606.

Wiggins, S., 2003 *Introduction to Applied Nonlinear Dynamical Systems and Chaos*. Springer, New York.

Yoshino, M., K. Murakami, and A. Tsuji, 2015 Analysis of the substrate inhibition of complete and partial types. Biochemical and Biophysical Reports **3**: 1–6.

How to cite this article: Abbas, A., and Khaliq, A. Nonlinear Dynamics and Chaos Control in a Discrete Sel'kov Model with Substrate Inhibition. *Chaos and Fractals*, 3(1), 29-37, 2026.

Licensing Policy: The published articles in CHF are licensed under a Creative Commons Attribution-NonCommercial 4.0 International License.

ADBA Chaos and Fractals
Cutting-Edge Scientific Solutions

e-ISSN: 3023-8951
RESEARCH ARTICLE
Vol.3 / No.1 / 2026 / pp.38-46
https://doi.org/10.69882/adba.chf.2026016

Ad-Click Prediction Enhanced by Nonlinear Dynamics-Inspired Feature Extraction and Ensemble Optimization

Ceyda Çağ[α,1], **Neslihan Akbulut**[α,2] **and Yusuf Çankırlı**[α,3]
[α]Hitit University, Faculty of Engineering and Natural Sciences, Department of Computer Engineering, 19030, Corum, Türkiye.

ABSTRACT The primary objective of this study is to enhance the predictive performance of machine learning models used for estimating Click-Through Rate (CTR), a key metric in digital advertising analytics. Beginning with a baseline Logistic Regression (LR) model applied to the "Click-Through Rate Prediction" dataset from Kaggle, the study systematically incorporates multiple optimization layers to improve forecasting accuracy. Inspired by nonlinear dynamics concepts, new feature representations were derived from temporal patterns and textual fields using TF-IDF and Word2Vec-based embeddings. Hyperparameter optimization techniques were then applied to refine model behavior, followed by the construction of ensemble architectures combining LR, XGBoost, Random Forest (RF), and Support Vector Machine (SVM) classifiers. Experimental results show that the optimized ensemble achieved the highest F1-score of 0.8694, yielding an improvement of approximately 12.7% over the baseline model. Overall, the study provides a comprehensive examination of feature extraction strategies, model optimization procedures, and ensemble fusion techniques, demonstrating the clear advantage of hybrid approaches in complex CTR prediction tasks.

KEYWORDS
Feature extraction
Ensemble learning
Machine learning
Hyperparameter optimization
Classification

INTRODUCTION

The digital environment is a virtual environment where people share their feelings and thoughts with each other. When this virtual environment was first established, people focused only on communicating with each other by sharing photos, videos and texts. As time passed, people started to use this medium not only as a source of communication, but also in many areas such as announcing their own brands, shopping, education, news and so on. Digital advertising emerged when people started shopping through this medium. Digital advertising is when people advertise using the digital environment to announce their brands, promote their products, and make sales. As time passes, people shop digitally, which has allowed digital advertising to increase and gain importance worldwide.

Digital advertising, which has spread globally, has become the focus of attention of all brands, sellers, institutions and users. Total advertising expenditures have increased worldwide according to the latest research. The global market size for digital advertising is expected to approach $700 billion in 2024 and exceed $830 billion by 2026. In 2023, a user spent approximately 6.5 hours a day interacting with ad content (Gangopadhyay *et al.* 2025) . Users are essential building blocks for engagement in the advertising industry. Digital advertising can now be seen while watching a video, playing a game, and using an app. In this way, it has gained direction in the digital advertising sector and it has become easier for brands to reach their target users.

Although many advantages emerge with the growth of digital advertising, some problems may also arise. In digital advertising, users' click-through rates have an important place in terms of evaluating many situations such as the user's requests, likes, complaints, and trends of the time. In digital advertising, predicting which ad will be clicked more has an important place. However, the click-through rate may not always reflect the truth. The placement of ads on the page is very important for this. Since users see the first ad they see more, they are more likely to click on that ad, which can make it difficult to find the real click-through rate of the ads. In addition, incorrect clicks made by users also make the click-through rate misleading. Advertising trends that change over time cause the click-through rate to change rapidly. All these factors prevent properly evaluating ad click-through rates, acting according to the user's wishes, and thus earning more.

Manuscript received: 18 December 2025,
Revised: 23 January 2026,
Accepted: 23 January 2026.

[1]234210020@ogrenci.hitit.edu.tr
[2]234210008@ogrenci.hitit.edu.tr
[3]234210024@ogrenci.hitit.edu.tr

The concept of CTR in digital advertising is a method used to evaluate the success of digital ads (AgencyAnalytics 2025). Click-through rate is an important problem in the field of digital marketing and online advertising. In our study, it is aimed to develop various hyperparameter optimizations, models, feature extraction, ensemble models and to help the click-through rate problem by combining these studies. With the increase in digital advertising, our study contributes to the development of many factors such as reaching the user more easily, interacting, allowing brands to introduce themselves, and using social platforms more effectively. Digital advertising is guided by user desires, and finding a click-through rate is important for advertisers, marketers, and campaign managers.

In this direction, the layout of the ads, which page they will appear on, which ad attracts more attention are learned and other services are offered to the user according to these details. User engagement with an effective digital ad is not limited to the first click or view; instead, it becomes more comprehensive. For example, a user who clicks on an ad for a particular book is taken not only to the product they are looking for, but also to other book recommendations personalized to their interests; This process aims to increase user engagement on the platform and encourage them to make additional purchases.In this way, in digital advertising, whatever type of content a user is interested in, similar ads appear more often, so that the ads can reach the right user. The overall progression of the study development process is shown in Figure 1.

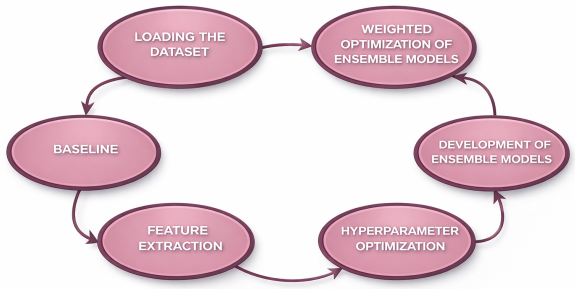

Figure 1 Project Development Flowchart

RELATED STUDIES

Yang and Zhai (2022) stated that the main purpose of CTR prediction in online advertising is to predict the likelihood that a user will click on an ad they see. They also mentioned that it was done by creating a model that numerically calculates the probability of a user clicking on the ad. They stated that the interest in this subject has increased in the last decade and that while statistical methods such as the LR model were used at first, these older models are now being replaced by more advanced approaches. The main advantages of the LR model are that it efficiently captures linear correlations between the feature and the label, offering an interpretable probability. On the other hand, they showed that the model was insufficient to model the complex and nonlinear interactions between them because it assumed that the features were independent.

Lou (2024) has conducted a comparative analysis of LR, RF, and XGBoost for CTR prediction in digital advertising.The study discussed machine learning concepts such as model selection, data processing, and feature engineering.He stated that there are difficulties that reduce the performance of the model, especially in the new data, and to address these difficulties, the performances of the LR, RF and XGBoost models were compared after preprocessing was applied to a complex dataset. Among the three models considered, XGBoost has been the most successful model, achieving the highest performance with an accuracy rate of 94.10% and an AUC score of 0.98 Compared to XGBoost, RF achieved 93.52% accuracy with an AUC score of 0.97, while LR achieved 93.23% accuracy and an AUC score of 0.96. As a result, it was revealed that XGBoost, which was effective in CTR prediction in the three models considered, is the most promising model with its efficient processing of complex data structures and superior prediction ability.

Zang (2019) focuses on predicting the click-through rate of loan ads. He performed data cleaning and transformation operations on user data obtained from the Finup platform. The first modeling to show the effects of the imbalanced structure of the dataset was SVM, Naive Bayes, using decision tree and neural network models and performing predictive analysis. While the accuracy rates of the models were over 97%, the sensitivity rates were found to be 0%. The reason for the sensitivity of 0% was interpreted as excessive imbalance, and it was concluded that undersampling was required to increase it. He stated that the SVM model performed better than other models. Experiments were conducted on 5 different datasets to compare the performance of the models. As a result of the experiments, the lowest 0.8936, the highest 0.9324 accuracy and the lowest 0.7295 and the highest 0.7839 precision were given. The study also used the results of SVM, the most successful model, to create a clear profile of users with high click potential and thus provide a directly applicable targeting strategy for loan ads.

AlAli *et al.* (2021) conducted a study on the prediction of click-through rate effectiveness in mobile ads using XGBoost and developed a machine learning-based CTR model in their study. They used the "Click-Through Rate Prediction Competition Dataset" dataset from the Kaggle platform and mentioned that the dataset they used was unbalanced. They applied the under-sampling technique to solve the imbalance problem. In their study, they used 4 different models, namely K-Nearest Neighbor (KNN), LR, RF and XGBoost, and after measuring the baseline performance of these models, they applied hyperparameter optimization methods on the models to improve the ROC-AUC score. In the optimized results of the models, it was revealed that the XGBoost algorithm performed better than the other three algorithms, RF 0.7544, LR 0.6428 and KNN 0.7172, with a ROC-AUC score of 0.7640. As a result, they added that important results were obtained depending on the superiority of XGBoost over the other three models and the evaluation metrics of the models.

Bratus and Bidyuk (2023) In their study, applied various feature engineering techniques to obtain low-dimensional representations of sparse and high-dimensional input features. They then trained the Naive Bayes, LR, SVM, Random Forest, and XGBoost models to compare their performance on the preprocessed data and select the best one. They stated that the dataset they used was KDD Cup 2012. The dataset was divided into test and training set, and they showed that there was no strong correlation between the variables and that there was an imbalance in the target variable. The evaluation metrics are ROC-AUC and LogLoss.

When the results of the models were taken, XGBoost achieved an AUC-ROC score of 0.6909 and a LogLoss score of 0.1783. Random Forest achieved an AUC-ROC score of 0.6654 and a LogLoss score of 0.1821. As a result, they stated that XGBoost stands out with its high performance by offering an approach supported by comprehensive data preparation processes and comparing different models for CTR prediction.

Table 1 Comparative Literature Analysis

Authors	Study	Methods	Results
Yang, Y., Zhai, P.	Click-through rate prediction in online advertising: A literature review	LR	CTR forecasting, advantages and limitations of the LR model
Lou, J.	Comparative Analysis of Logistic Regression, Random Forest, and XGBoost for CTR Prediction in Digital Advertising	LR, Random Forest, XGBoost	XGBoost: 94.10% accuracy, highest 0.98 AUC; RF: 93.52%, 0.97 AUC; LR: 93.23%, 0.96 AUC
Zhang X.	Click Prediction for P2P Loan Ads Based on Support Vector Machine	Naive Bayes, Decision Tree, Neural Network, SVM	The SVM model achieved 89.36-93.24% accuracy and 72.57-78.39% sensitivity using RBF core
M. AlAli et al.	Click-Through Rate Effectiveness Prediction on Mobile Ads Using Extreme Gradient Boosting	KNN, LR, RF, XGBoost	XGBoost: 0.7640 ROC-AUC (highest); RF: 0.7544; KNN: 0.7172; LR: 0.6428.
O. S. Bratus, P. I. Bidyuk	Towards Click-Through Rate Prediction in Online Advertising	Naive Bayes, LR, Random Forest, SVM	XGBoost: AUC-ROC 0.6909, Logloss 0.1783 (best result)
J. R. Guillen	Click Through Rate Prediction Leveraging Machine Learning Techniques for Mobile Digital Advertisement	LR, RF, XGBoost, CatBoost, FFNN	CatBoost: Lowest logloss 0.5836, highest F1-score 0.7093

Rojas Guillen (2024) emphasizes the importance of estimating CTR to optimize the effectiveness of mobile advertising campaigns. It has demonstrated the potential of machine learning models in predicting CTR for mobile digital ads. The models it uses are LR, RF, XGBoost, CatBoost and Feedforward Neural Network (FFNN). The dataset consists of 10 days of click data corresponding to a high-dimensional categorical mobile ad impressions. Due to its low click rate, it has an unstable data structure and is balanced by the downsampling technique. In terms of model performance, it has been the most successful model with the lowest LogLoss score of 0.5836 and the highest F1-score of 0.7093. Overall, the study reveals the superior performance of CatBoost, especially in advertising data with a high-dimensional and categorically weighted data structure. The information on the studies, authors, methods used and the results obtained are shown in Table 1 in which the literature analyses carried out within the scope of the study are explained comparatively.

MATERIALS AND METHODS

In this study, the dataset named "Click-Through Rate Prediction" shared by user swekerr on the Kaggle platform was used swekerr (2024). In addition, the importance of click-through rate in digital advertising and different methods were examined in order to find more realistic value in the dataset. This dataset consists of 10000 data samples and 10 features. The features in the dataset and their definitions are shown in Table 2.

These features give us data such as users' information, which device they use, time information. The dataset contains both categorical and numeric features. The Ad Topic Line, City, Gender, Country features are categorical, the Daily Time Spent on Site, Age, Area Income, Daily Internet Usage and Timestamp features are numeric, the target feature is the clicked or non-clicked on Ad.

There are 5 data samples from the dataset are shown in Table 3. It is possible to see the subheadings in the features. In this table, all values are known and there are no missing values. Not all features can have similar or identical features, they are not unique. Daily Time Spent on Site, Age, Area Income, Daily Internet Usage, Ad Topic Line, City, Country, Timestamp features can take similar and different values, while Gender and Clicked on Ad can take stereotyped values. Gender takes male and female values, while Clicked on Ad takes 1 (clicked)- 0 (not clicked) values. As a result of the data quality checks, incompatible matches and content inconsistencies were detected between the City and Country attributes. In the analyzes, it was observed that there were more than one different country value for the same city value. For example, multiple locale matches have been identified for 417 cities. These inconsistencies have been omitted from the City feature dataset, as they can impact the reliability of the model.

Table 2 Features of The Original Dataset

Feature	Description	Type
Daily Time Spent On Site	Average time spent on the website (minutes)	Numeric
Age	Age of the user	Numeric
Area Income	The average income level of the user's region	Numeric
Daily Internet Usage	User's daily internet usage time (minutes)	Numeric
Ad Topic Line	Headline or subject text of the ad	Categorical
City	The city where the user lives	Categorical
Gender	User's gender	Categorical
Country	Country where the user lives	Categorical
Timestamp	Date and time data was collected	Datetime
Clicked on Ad	Click indicator (0: no click, 1: click)	Target

Histogram graphs according to the ad click or non-click rate of the features in the dataset are given in Figure 2. In this study, graphs were used to see the click rate. As can be seen in the graphs, there are histogram graphs of numerical features. According to the analysis, the 'Daily Time Spent on Site' (a) graph shows a positive relationship between the time spent on the site and the click-through rate, especially in the 80-90 minute range. The 'Age' (b) graph shows that users aged 40-60 tend to click on ads more.

Table 3 Samples of The Original Dataset

Daily Time Spent on Site	Age	Area Income	Daily Internet Usage	Ad Topic Line	City	Gender	Country	Timestamp	Clicked on Ad
62.26	32.0	69481.85	172.83	Decentralized real-time circuit	Lisafort	Male	Svalbard & Jan Mayen Island	2016-06-09 21:43:05	0
65.77	34.0	59785.94	168.34	Cloned explicit middleware	Kingshire	Male	Namibia	2016-02-27 08:52:50	0
79.6	23.0	62784.85	146.8	Team-oriented executive core	Patriciahaven	Female	Czech Republic	2016-01-14 14:00:09	1
40.47	27.0	14548.06	190.17	User-friendly upward-trending intranet	New Lucasburgh	Female	Poland	2016-02-10 19:20:51	1
50.63	31.0	61067.58	236.87	Optional multi-state hardware	Austinland	Male	Hong Kong	2016-07-04 23:17:47	0

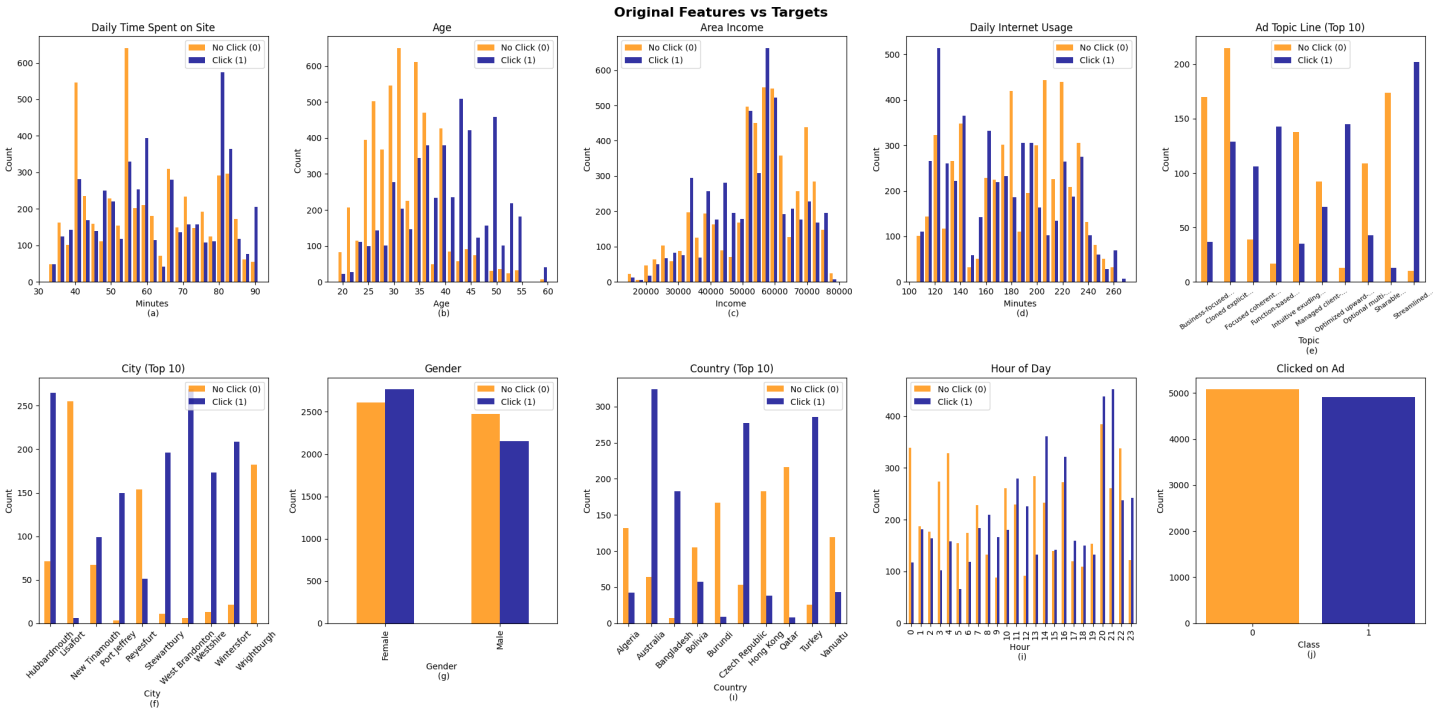

Figure 2 Feature Distribution Histograms for Click and Non-Click Samples

features such as 'Area Income' (c) and 'Daily Internet Usage' (d) do not present a significant separation, and the density in these graphs suggests that the overall user profile in the dataset is clustered in these ranges rather than a specific behavior. The 'Ad Topic Line (Top 10)' (e) chart, which emphasizes the importance of ad content, proves that some headlines directly increase click-through rates. In geographic distribution, the 'Country (Top 10)' (h) chart shows that countries like Autralia, Burundi, and Turkey have higher click-through rates, while the 'Gender' (g) chart shows that women are more likely to click. The 'City (Top 10)' (f) graph was used for analysis prior to data quality control; During model training, the City feature was removed due to incompatibility, while the 'Gender' (g) chart reveals that women are more likely to click. Additionally, the 'Hour of Day' (i) chart indicates that the hours of day also play a significant role, with click-through rates increasing in the morning hours. Finally, the 'Clicked on Ad' (j) graph, which shows the overall distribution of the target variable, shows that the number of clicked and non-clicking users in the dataset was

almost equal.

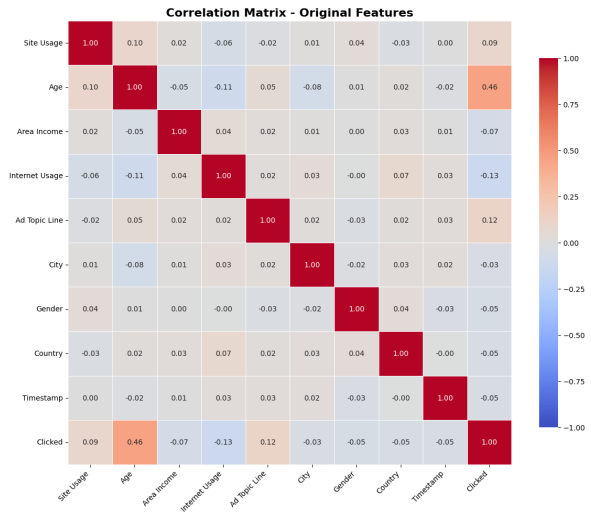

Figure 3 Correlation Matrix Across Features

There is an almost equal distribution in click-through and non-click-through rates in the dataset. The correlation matrix in Figure 3 is used to see the interactions of the features in this study. Weak relationships are mostly seen in the correlation matrix. However, the highest score is seen with 0.46 among the age and click features. For this reason, it can be observed that the ad click-through rate increases as the age value increases.

All of the machine learning models and data processing processes developed in the study were carried out by using the open source libraries of the Python programming language. DataFrame structures provided by the Pandas library were used to bring the data into an easy-to-process format with the loading and structuring stages (The pandas development team 2020; McKinney 2010). Numpy library was preferred for numerical operations and mathematical transformations of features that require high performance (Harris *et al.* 2020). It has enabled us to execute computationally intensive preprocessing steps such as StandardScaler in a more performance-friendly manner. In the data visualization phase, two libraries were used. Matplotlib was used to create the basic and customized images we wanted (Hunter 2007). The seaborn library was preferred in order to present our analyzes and make our findings more understandable by producing statistically rich and aesthetically advanced graphics with less code (Waskom 2021). The machine learning workflow was created by the Scikit-learn library. (Pedregosa *et al.* 2011).

The basic steps of the dataset, such as separating it into training and testing, setting up and training the models, and evaluating their performance with metrics such as F1 and ROC-AUC, were carried out through this library. It has significantly accelerated the experimental process by facilitating the experimentation and comparison of different algorithms. In the Feature Engineering phase, two complementary libraries were used. New features were derived from both temporal and textual data in order to increase the performance of the model. The semantic richness of the text data was also utilized. The Natural Language Toolkit (NLTK) was used as an infrastructure to break down texts into their basic components, such as words (Bird *et al.* 2009). The Gensim library was also preferred in order to convert the semantic meaning of these components into a numerical format that the model could understand (Řehůřek and Sojka 2010). Our dataset is strengthened with new features that reflect temporal and textual meaning thanks to these approaches.

In the study, a hybrid encoding strategy was applied to convert categorical features into numerical form. This strategy includes different encoding methods according to the cardinality of categorical variables, that is, having many features. One-Hot Encoding is applied for low-cardinality features. This encoding method preserves the information by converting each category into a column in binary (0/1) and ensures that each category is evaluated equally. In this step, the gender feature includes two new features (Male/Female), the season feature contains four new features (Spring, Summer, Autumn, Winter), and the time_of_day feature contains four features (Morning, Afternoon, Evening, Night). The features resulting from the feature extraction process are shown in Table 4.

Table 4 Extracted Feature Set

Feature	Description	Type
hour	Time when data was recorded (between 0–23)	Numeric
day_of_week	Day of the week (0 = Monday ... 6 = Sunday)	Categorical
is_weekend	Whether the data belongs to the weekend (0 = weekdays, 1 = weekends)	Binary
quarter	Quarter of the year (1 = January–March, ... 4 = October–December)	Categorical
month	Month to which the data belongs (1–12)	Numeric
week_of_year	What week of the year it is in (1–52/53)	Numeric
season	Seasonal information (Winter, Spring, Summer)	Categorical
time_of_day	Part of the day (Morning, Afternoon, Evening, Night)	Categorical
textual features	Numeric attributes derived from the ad headline (Ad Topic Line) using TF-IDF, Word2Vec, and text statistics methods	Numeric

Frequency Encoding method was used for categorical variables with high cardinality. This approach represents the incidence of each category value in the dataset as a numerical feature and controls the number of features. If One-Hot Encoding is applied in this step, it adds a large number of new columns, increasing the complexity of the model and leading to overfitting. Frequency Coding represents category values in a single numerical column, reducing model complexity and training time. The advantage of this method is that, unlike Ordinal Encoding, it does not create an artificial numerical order between categories; thus, reducing the risk of bias in model results. Following the data quality controls,

the City feature was removed from the dataset, and Frequency Coding was applied for the Country feature. As a result of the hybrid approach model, 2 new features were created for gender, 4 for season, 4 for time_of_day, and country feature 1 numeric feature represented by frequency value. This approach minimizes information loss while keeping feature size in check and does not create artificial sorting between categories. Three different approaches were used to extract meaningful information from many text data, such as advertising content. TF-IDF (Term Frequency-Inverse Document Frequency) vectorization converts text data into numerical data. In this study, 100 new features were obtained using TfidfVectorizer. In order to obtain these features, the 100 most important and most frequently seen words were selected with the parameter max_features=100. The parameter ngram_range = (1,2) is set to include both single word (unigram) and binary word groups (bigram). This approach can capture the meaning of word groups and create more detailed features. The parameters min_df=2 and max_df=0.85 filter out both very rare and very common words,creating more meaningful features.

Word2Vec embedding and TF-IDF-weighted concatenation create 100-dimensional vectors for each word name to capture the semantic relationships of words. 100-dimensional embeddings are produced with the parameter of model vector_size=100. The calculation was made by representing each sentence as a vector and weighting the weighted average of the Word2Vec vectors of the Word2Vec vectors with the TF-IDF scores. This approach can create more detailed features by combining both the semantic meaning and importance of words in the dataset TF-IDF models. With this method, 100 more features were obtained.

Text statistics features In order to capture the structural features of the text, four statistical features were calculated: word count, character count, unique word count, average word length. These features improve model performance by capturing the structural features of the data in the ad headline. With the combination of these 3 methods, a total of 204 new features were extracted from the ad headline data, including TF-IDF vectorization 100 features, Word2Vec embedding 100 features, and text statistics 4 features. These features were combined with numerical and categorical features to create a 225-dimensional feature set. This hybrid approach significantly enhances the model's performance by capturing different aspects of text content, such as the ad headline. As a result of all these methods, our F1 and ROC-AUC values change significantly when we run LR on the dataset again.

USED MODELS AND HYPERPARAMETER OPTIMIZATIONS

In order to improve the performance of machine learning models, various optimization techniques can make significant contributions to the process of finding the most appropriate hyperparameter combinations. In our study, Random Search, Grid Search, Optuna, Genetic Algorithm (GA) and Artificial Bee Colony (ABC) Algorithm were used for hyperparameter optimization. Random Search is a search method in which a predetermined number of combinations of hyperparameters are randomly sampled from a user-defined search space. Grid Search is a comprehensive search method in which all combinations on a subset of the hyperparameter space (a grid) manually specified by the user are tried (Bergstra and Bengio 2012).

Optuna is automating and making the hyperparameter search process, which is one of the laborious tasks in machine learning projects, efficient (Akiba *et al.* 2019). GA is a search and optimization technique inspired by the mechanisms of natural evolution and genetics. Genetic algorithms are used to find robust and efficient solutions for problems with complex and large search spaces (Goldberg 1989). The ABC Algorithm is a search and optimization algorithm based on swarm intelligence. The main purpose of the algorithm is to find the optimal solution in complex optimization problems (Karaboga and Basturk 2007).

LR analysis is an analysis that allows us to construct a regression model without requiring assumptions such as normality, continuity, covariance and multivariate normality (Şenel and Alatlı 2014). However, the capacity to model nonlinear relationships is limited due to the linear decision boundary. In order to overcome this limitation Random Forest is a supervised machine learning method consisting of an ensemble technique and a large number of decision trees used for categorization. Similarly SVM are supervised maximum-margin models in machine learning with correlated learning algorithms that analyze data for classification and regression analysis (Cortes and Vapnik 1995). In addition, XGBoost is a different approach to developing a decision tree than the classical gradient boosting decision tree methodology (Shams *et al.* 2024).

Within the scope of the Nonlinear Dynamics-Inspired approach the hyperparameter optimization methods we used in our study were applied in the LR model. Our goal is to increase our F1 and ROC-AUC score by taking optimized hyperparameters. As a result of the trials, Genetic Algorithm achieved the highest performance among all the methods examined and achieved an F1 score of 0.7826; ABC Algorithm 0.7820, Random Search 0.7818, Grid Search 0.7806 and Optuna 0.7686 F1 scores. These results show that the evolutionary search strategy of Genetic Algorithm optimization yields the most effective results in this problem and dataset, thanks to the more effective scanning of nonlinear performance surfaces. As a result, the Logistic Regression model was retrained using the optimal parameters found by the Genetic Algorithm (C: 17.13, penalty: 'l1', solver: 'liblinear', max_iter: 5658, class_weight: 0: 1, 1: 2) and an F1 score of 0.7826 was obtained. Genetic Algorithm has been shown to be an effective and reliable method to find the best combination in defined parameter space involving nonlinear structures.

In line with the Nonlinear Dynamics-Inspired approach, after the hyperparameter optimizations were implemented, the model training phase was started. In order to make a strong classification, a detailed model development and optimization process was followed. First, the classification algorithms XGBoost, Random Forest and SVM, which are discussed in the study, were used. To enhance the performance of these models on the training data, extensive optimization was conducted using Random Search to explore nonlinear parameter interactions more effectively. The optimization process was carried out together with the Cross Validation method in order to ensure the generalization ability of the model. In addition to this optimization, threshold optimization was also used to optimize the binary classification threshold of the results of the classification models. The main purpose of this optimization is to enhance the F1 score, a critical score especially in imbalanced datasets where nonlinear decision boundaries need to be determined effectively. When the optimization results were examined, it was observed that these optimizations significantly increased the F1 score of the models. Among the trained models, it was observed that the XGBoost model showed the highest performance by being more effective on LR and was a more effective classification model.

ENSEMBLE MODELS AND PERFORMANCE ENHANCEMENT

In order to take individual model performances to the next level, ensemble methods powered by model diversity were applied. The strategy aims to produce more robust and highly accurate results by compensating for the weaknesses of different models that exhibit nonlinear decision structures with each other. In the process, the combinations of each base model with the LR model were examined and which model would be more effective was examined. The LR model was used as a key component in the task of combining and weighting predictions. In this context, a total of seven different LR-based ensemble combinations were created using the basic models SVM, RF and XGBoost. These ensemble structures, detailed in Figure 4, were examined with two approaches; Uniform Weighting, equal contribution was given to all models in the combination. In this approach, it is aimed to generalize by averaging the model diversity. In Optimized Weighting (Best Weighting), the Random Search technique was used to automatically optimize each model's contribution to the prediction on nonlinear (nonlinear) performance surfaces to increase the F1 score. This method allowed to learn which model should have more say through data.

As a result of the investigations, it was seen that the optimized weighting approach was more effective and produced higher F1 scores compared to equal weighting. This approach has proven that it can be enhanced not only by incorporating powerful models but also by evaluating and optimizing the models' contributions to performance within a nonlinear performance structure. In particular, the ensemble structure of the models combined with the optimized weights approach achieved the highest F1 score in the study and was seen as the most effective method among the methods used. In this ensemble model, it was also observed that the threshold optimization applied had a positive effect on performance. The model development process has shown that instead of looking for a single model, powerful models are comprehensively optimized and combined with ensemble methods to provide the highest classification performance. The highest F1 score was achieved by the weighted ensemble method, which included LR, XGBoost and SVM models. The weighting of each model in the final estimate was optimized to maximize the F1 score by considering complex and non-linear contribution relationships, and this strategy outperformed all individual models. Thus, it was seen that different models compensated for their weaknesses with each other and created a successful solution.

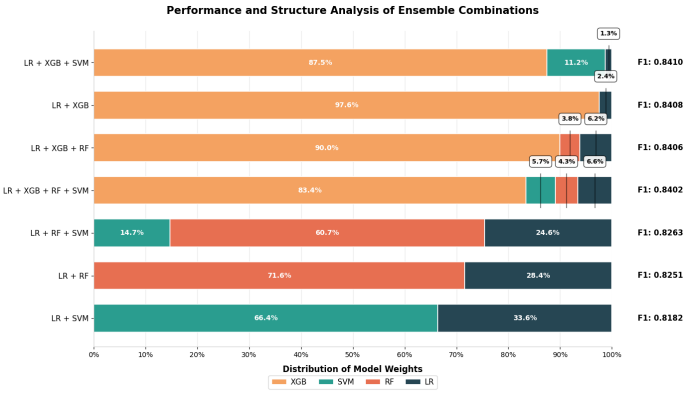

Figure 4 Performance and Structure Analysis of Ensemble Combinations

RESULT AND DISCUSSION

In this section, the results of the multi-stage optimization process carried out to improve the performance of the CTR forecasting model are presented and the results obtained are analyzed. Based on a baseline model created with the LR model, it is aimed to gradually increase performance through feature extraction, various hyperparameter optimization techniques, and finally ensemble modeling approaches that can capture nonlinear interactions, respectively. In this process, the performance of the ensemble structures was evaluated, where the LR model was refined with different optimization algorithms, followed by the inclusion of powerful models such as LR, XGBoost, RF, and SVM were incorporated, which exhibit complex and non-linear decision structures. F1 score and ROC-AUC values were used to measure model success at each stage of the study. First, the effects of hyperparameter optimization algorithms on the LR model are presented comparatively in the graph in Figure 5, followed by a comparative performance analysis of individually optimized models and ensemble structures consisting of various combinations of these models, detailing the approach that yields the highest success.

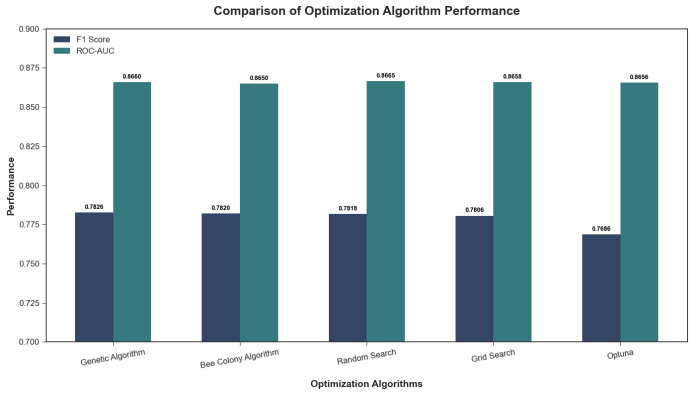

Figure 5 Performance of Hyperparameter Optimizations

After maximizing the performance of the baseline LR model through hyperparameter optimization, more powerful algorithms such as XGBoost, RF, and SVM were introduced to further enhance its predictive power, offering nonlinear decision structures. Various combinations of XGBoost, RF and SVM models were created with our base model LR and the comparative results of all ensemble combinations obtained after this optimization process are shown in Figure 5. ranked according to the F1 score. The performance of the different ensemble combinations tested is analyzed in Figure 4. When we analyze the graph, it is clear that the XGBoost model, which can model complex and nonlinear relationships more effectively, has the highest weight of all combinations involved. XGBoost is followed by SVM and Random Forest models, which also make significant contributions. LR, on the other hand, systematically has an extremely low weight in all combinations, which suggests that LR is not a direct predictor in these advanced structures, but rather a fundamental part that unifies the predictions of models. As a result, this analysis shows that the highest performance is achieved through an optimized combination of models, driven by XGBoost and powered by SVM.

In line with the expected results, a progressive improvement method such as feature extraction, hyperparameter optimization, and eventually ensemble modeling was found to be effective in the CTR prediction problem.It was observed that the holistic use of different optimization and model combination methods, which

is the hypothesis of the study, under complex and nonlinear model interactions will increase performance. The fact that the highest performance model obtained includes powerful algorithms such as XGBoost and SVM, which are frequently found successful in the literature, shows the robustness of the theoretical infrastructure of the study. The results obtained in this study are specific to the dataset used. The model's performance may vary across other advertising datasets with different distributions or features. Additionally, the complexity of the model and its inclusion of multiple algorithms increase the computational cost in training and prediction processes.

CONCLUSION

This study presents a machine learning approach that combines feature extraction, hyperparameter optimization, and ensemble modeling techniques to solve the CTR prediction problem. In the first stage, a base model was created on the dataset using Logistic Regression, followed by deriving new features from temporal and textual data through TF-IDF and Word2Vec methods. Hyperparameter adjustments were performed on the LR model using different optimization algorithms, and in the final stage, weight-optimized ensemble structures including LR, XGBoost, Random Forest, and SVM models were developed. As a result of combining the models by weighting them according to the F1 scores, an F1 score of 0.8694 was obtained and it was observed that the ensemble modeling approach offered higher and more stable performance instead of single models. However, since the development and testing processes of the study were conducted solely on a single dataset obtained from the Kaggle platform, the generalizability of the model is limited by the statistical distribution of the dataset used, the feature structure, and the frequency distribution of CTR rates.

In order to reduce this limitation, it is important to perform cross-dataset validation on CTR datasets obtained from different platforms or different time intervals in future studies to evaluate the durability of the model against different data distributions and user behavior patterns. Additionally, to mitigate the negative effects of distribution differences between datasets, implementing feature normalization, domain adaptation, and resampling techniques can enhance the model's generalization capability by preventing it from overfitting a specific data source. Instead of just a single training-test separation in the model evaluation process, using repeated cross-validation strategies with different random bins will make performance metrics more reliable and generalizable. Although all features were used directly in the current study, high-dimensional feature spaces increase computational cost, increase model complexity, and strengthen the risk of overlearning. Therefore, the application of feature reduction techniques in future studies offers significant potential for improvement.

Eliminating unnecessary or highly correlated features with feature selection-based methods makes the model simpler and more interpretable; Feature selection-based methods eliminate unnecessary or highly correlated features, making the model simpler and more interpretable; while feature extraction-based methods allow for a more meaningful representation of the data. This representation can be high-dimensional or low-dimensional, depending on the method used. However, since it is critical to keep information loss under control in this process, the effects of dimensionalization methods on model accuracy, computational cost, and generalization performance should be analyzed comparatively. Accordingly, the inclusion of different dimensionality reduction algorithms and alternative gradient boosting methods such as CatBoost and LightGBM in the ensemble structure and testing them on larger and different CTR datasets will more comprehensively demonstrate the effectiveness of the proposed approach in practical applications. LightGBM offers structural optimizations to improve computational efficiency in large-scale and high-dimensional datasets (Ke *et al.* 2017), while CatBoost reduces the need for preprocessing due to its architecture that can handle categorical variables directly, allowing for the development of more stable models (Pemila *et al.* 2024). The integration of these models into the community structure can lead to meaningful gains in both scalability and generalization performance.

Ethical standard

The authors have no relevant financial or non-financial interests to disclose.

Availability of data and material

The data that support the findings of this study are available from the corresponding author upon reasonable request.

Conflicts of interest

The authors declare that there is no conflict of interest regarding the publication of this paper.

LITERATURE CITED

AgencyAnalytics, 2025 Click-through rate (ctr) definition. https://agencyanalytics.com/kpi-definitions/click-through-rate-ctr.

Akiba, T., S. Sano, T. Yanase, T. Ohta, and M. Koyama, 2019 Optuna: A next-generation hyperparameter optimization framework. In *Proceedings of the 25th ACM SIGKDD International Conference on Knowledge Discovery & Data Mining (KDD '19)*, pp. 2623–2631, ACM.

AlAli, M., M. AlQahtani, A. AlJuried, T. AlOnizan, D. Alboqaytah, *et al.*, 2021 Click-through rate effectiveness prediction on mobile ads using extreme gradient boosting. Computers, Materials & Continua **66**: 1681–1696.

Bergstra, J. and Y. Bengio, 2012 Random search for hyper-parameter optimization. Journal of Machine Learning Research **13**: 281–305.

Bird, S., E. Klein, and E. Loper, 2009 *Natural Language Processing with Python*. O'Reilly Media, Inc., Sebastopol, CA.

Bratus, O. S. and P. I. Bidyuk, 2023 Towards click-through rate prediction in online advertising. Problems of Applied Mathematics and Mathematical Modeling **23**: 3–17.

Cortes, C. and V. Vapnik, 1995 Support-vector networks. Machine Learning **20**: 273–297.

Gangopadhyay, B., Z. Wang, A. S. Chiappa, and S. Takamatsu, 2025 Adaptive budget optimization for multichannel advertising using combinatorial bandits. arXiv preprint arXiv:2502.02920 .

Goldberg, D. E., 1989 *Genetic Algorithms in Search, Optimization, and Machine Learning*. Addison-Wesley, Reading, MA.

Harris, C. R., K. J. Millman, S. J. van der Walt, R. Gommers, P. Virtanen, *et al.*, 2020 Array programming with NumPy. Nature **585**: 357–362.

Hunter, J. D., 2007 Matplotlib: A 2d graphics environment. Computing in Science & Engineering **9**: 90–95.

Karaboga, D. and B. Basturk, 2007 A powerful and efficient algorithm for numerical function optimization: Artificial bee colony (abc) algorithm. Journal of Global Optimization **39**: 459–471.

Ke, G., Q. Meng, T. Finley, T. Wang, W. Chen, *et al.*, 2017 Lightgbm: A highly efficient gradient boosting decision tree. In *Advances in Neural Information Processing Systems*, volume 30.

Lou, J., 2024 Comparative analysis of logistic regression, random forest, and xgboost for ctr prediction in digital advertising. In *Proceedings of MIED 2024*, Atlantis Press.
McKinney, W., 2010 Data structures for statistical computing in python. In *Proceedings of the 9th Python in Science Conference*, pp. 56–61.
Pedregosa, F., G. Varoquaux, A. Gramfort, V. Michel, B. Thirion, *et al.*, 2011 Scikit-learn: Machine learning in python. Journal of Machine Learning Research **12**: 2825–2830.
Pemila, M., R. K. Pongiannan, R. Narayanamoorthi, K. M. AboRas, and A. Youssef, 2024 Application of an ensemble catboost model over complex dataset for vehicle classification. PLOS ONE **19**: e0304619.
Řehůřek, R. and P. Sojka, 2010 Software framework for topic modelling with large corpora. In *Proceedings of the LREC 2010 Workshop on New Challenges for NLP Frameworks*, pp. 45–50.
Rojas Guillen, J. M., 2024 *Click Through Rate Prediction Leveraging Machine Learning Techniques for Mobile Digital Advertisement*. Master's thesis, Lund University.
Şenel, S. and B. Alatlı, 2014 Lojistik regresyon analizinin kullanıldıgı makaleler üzerine bir inceleme. Journal of Measurement and Evaluation in Education and Psychology **5**: 35–52.
Shams, M. Y., A. M. Elshewey, E.-S. M. El-kenawy, A. Ibrahim, F. M. Talaat, *et al.*, 2024 Water quality prediction using machine learning models based on grid search method. Multimedia Tools and Applications **83**: 35307–35334.
swekerr, 2024 Click-through rate prediction. Kaggle Datasets .
The pandas development team, 2020 pandas-dev/pandas: Pandas.
Waskom, M. L., 2021 Seaborn: Statistical data visualization. Journal of Open Source Software **6**: 3021.
Yang, Y. and P. Zhai, 2022 Click-through rate prediction in online advertising: A literature review. Information Processing & Management **59**: 102853.
Zang, X., 2019 Click prediction for p2p loan ads based on support vector machine. Journal of Physics: Conference Series **1168**: 032042.

How to cite this article: Çağ, C., Akbulut, N., and Çankırlı, Y. Ad-Click Prediction Enhanced by Nonlinear Dynamics-Inspired Feature Extraction and Ensemble Optimization. *Chaos and Fractals*, 3(1), 38-46, 2026.

Licensing Policy: The published articles in CHF are licensed under a Creative Commons Attribution-NonCommercial 4.0 International License.

ADBA Chaos and Fractals
Cutting-Edge Scientific Solutions

e-ISSN: 3023-8951
RESEARCH ARTICLE
Vol.3 / No.1 / 2026 / pp.47-53
https://doi.org/10.69882/adba.chf.2026017

Evaluation of Deep Learning Architectures for Pulmonary CT Lesion Classification Highlighting Diagnostic Performance

Ugur Bahtiyar Guven [α,1], **Yigitcan Cakmak** [α,2] **and Ishak Pacal** [α,3]
[α]Department of Computer Engineering, Faculty of Engineering, Igdir Universty, 76000, Igdir, Türkiye.

ABSTRACT Early identification of pulmonary lesions is a critical factor in enhancing patient prognosis and survival rates. This study systematically evaluates the diagnostic performance of five deep learning architectures, ConvNeXt Base, ResNet50, EfficientNetV2 Small, InceptionV4, and Xception, for the three-class categorization of Computed Tomography (CT) scans into Benign, Malignant, and Normal categories. Utilizing the public IQ OTH NCCD dataset, we applied a transfer learning approach with ImageNet weights, complemented by a robust training pipeline incorporating dynamic data augmentation and early stopping to mitigate overfitting and ensure model generalization. Model efficacy was rigorously assessed on an independent test set using accuracy, precision, recall, and F1-score metrics. Experimental results indicate that InceptionV4 emerged as the most reliable architecture, achieving an overall accuracy of 0.988 and a macro-averaged F1-score of 0.976. Notably, this model demonstrated perfect sensitivity for the pathologically critical malignant class, achieving a recall rate of 1.00, thereby prioritizing clinical safety. These findings confirm that advanced neural networks can serve as dependable secondary opinion systems for clinicians. Given its superior sensitivity and balanced diagnostic profile, InceptionV4 represents a promising candidate for integration into automated lung cancer screening workflows to improve diagnostic precision.

KEYWORDS
Lung cancer
Deep learning
Computed tomography (CT)
InceptionV4
Transfer learning

INTRODUCTION

The prevalence of lung cancer as a serious public health concern is exemplified by its exceptionally high incidences and deaths (Baji *et al.* 2025; Ayesha *et al.* 2025), the World Health Organization (WHO) has estimated there are approximately 1.8 million deaths due to lung cancer annually, making it one of the most common causes of cancer death worldwide. The primary way of improving the prognosis and survival probability of patients diagnosed with lung cancer is through timely and accurate diagnosis. Unfortunately, patients are typically asymptomatic until the later stages of the disease when they may have the least amount of opportunities to receive an effective form of treatment (Mahmud *et al.* 2025; Rai *et al.* 2025; Siegel *et al.* 2025; Çakmak and Maman 2025). Other aspects of diagnostic, CT imaging of the lungs (the use of computed tomography) provides high-resolution cross-sectional images that may show slight nodules or other abnormalities that might have been overlooked due to the use of conventional radiological procedures (e.g., chest X-rays). Yet, the radiologist's manual interpretation of CT scans is extremely labour-intensive and time-consuming, and there is potential for variation in interpretation among different radiologists, which may result in both false positives and false negatives when distinguishing between malignant, benign, and normal lung tissues (Deepa *et al.* 2024; Venkatraman and Reddy 2024; Chowdhury *et al.* 2024).

The development of state-of-the-art artificial intelligence techniques for medical imaging has led to significant improvements in the ability of radiologists and pathologists to identify abnormal images using digital imaging systems (Attallah and Pacal 2026). With this progression in artificial intelligence comes a new set of challenges and opportunities for those working in the fields of oncology and radiology (Zafar *et al.* 2024; Dev *et al.* 2025; Çakmak and Pacal 2025; Çakmak 2025). In addition to developing algorithms that are trained to visually detect signs of cancerous tumors, researchers have developed methods to allow computer systems to analyze multiple factors related to a scanned body part (i.e., tissue density, blood flow, etc.). The ability for a computer system to learn through examples aids researchers in developing algorithms that produce better visual outputs (Jozi and Al-Suhail 2024; Lad *et al.* 2024; Lavanya *et al.* 2024; Ince *et al.* 2025).

Over the last few years, many different deep learning algorithms have been created by researchers, all aimed at identifying different types of lung cancer. The most common types of algorithms that researchers have developed include those based on the use of convolutional neural networks (CNNs), as well as hybrid systems and attention networks. Each of these types of algorithms falls into a particular category based on its design and purpose, such as optimized performance-oriented designs, architectural de-

Manuscript received: 2 November 2025,
Revised: 21 December 2025,
Accepted: 22 December 2025.

[1]ugurbahtiyarguven@gmail.com
[2]ygtcncakmak@gmail.com (**Corresponding author**).
[3]ishak.pacal@igdir.edu.tr

signs that depend on attention mechanisms for classification, and efficiency-oriented designs.

Ruprah *et al.* (2024) used Synthetic Minority Over-sampling Technique (SMOTE) combined with Gaussian blur preprocessing as part of their optimization and data handling solutions for addressing the common problem of class imbalance, demonstrating their optimized VGG-16 design had a high level of accuracy as a result of thorough data preprocessing. In a similar manner, Deepika *et al.* (2024) concentrated on hyper-parameter optimization using a two-stage methodology where initially a U-Net model is used to reconstruct the anatomical features while simultaneously reducing the noise before adding the tuned ShuffleNet classifier using Particle Swarm Optimization (PSO), which provided a high level of accuracy, 97.85

Recent studies have incorporated attention mechanisms into the feature enhancement area to direct the models to focus more on significant nodule features. For example, Muqeet *et al.* (2025) developed the Selective Kernel MobileNetV3 (SK-MNV3) incorporating the Selective Kernel Attention Mechanism in order to adapt dynamically the size of the receptive field. The SK-MNV3 model achieved 98.82% accuracy for identifying nodules of various sizes. Chaddad *et al.* (2025), in a parallel effort, designed ResNet+ by adding a Convolutional Block Attention Module (CBAM) to the base ResNet structure to maintain more spatial feature information; thus providing 99.25% accuracy when tested with the IQ-OTH/NCCD data.

In a nutshell, they wanted to compare state-of-the-art deep learning architectures regarding how they can simultaneously meet multiple tradeoffs such as high model accuracy, fast inference time, small model size, limited resources for deployment, etc. Akbari *et al.* (2024) have shown that self-attention mechanisms allow ViT models trained on histopathological images to capture global correlations better than traditional convolutional neural networks (CNNs). On the other hand, Shakya *et al.* (2025) compared compact models suitable for resource-constrained environments like edge computing and found EfficientNetV2-B0 to be the lightweight model with 98.64% accuracy.

Although the potential of custom CNNs and hybrid DL models for medical image analysis is evident in the literature, these methods typically have a significant amount of computation, and therefore, they have limitations in terms of reproducibility and standardization within clinical workflows (Munteanu *et al.* 2025). On the other hand, established state-of-the-art architectures, utilizing transfer learning, have excellent feature extraction and generalization capabilities, especially with small amounts of annotated medical data available (Moldovanu *et al.* 2024; Tătaru *et al.* 2025). With these observations in mind, this study proposes to conduct a thorough and rigorous systematic comparison of five deep learning architectures (ConvNeXt Base, ResNet-50, EfficientNetV2 Small, InceptionV4, and Xception) using the IQ-OTH/NCCD dataset for lung cancer classification across three classes. The major contributions of this research are...

- It provides a systematic evaluation of diverse architectural families (including standard CNNs, Inception-based, and lightweight models) to determine the most effective strategy for lung nodule characterization.
- Unlike studies focusing solely on overall accuracy, this research prioritizes class-wise performance metrics, specifically Recall and Precision, to identify models that minimize False Negatives in malignant cases.
- The study analyzes the trade-off between computational cost (parameters/GFLOPs) and diagnostic performance, identifying InceptionV4 as a superior candidate for reliable, automated clinical decision support systems.

MATERIALS AND METHODS

Dataset and Data Preprocessing

We used the publicly available IQ-OTH/NCCD Lung Cancer Dataset for the empirical evaluation of the proposed models. The IQ-OTH/NCCD Lung Cancer Dataset is a well-established benchmark for lung cancer classification. The dataset is available at (hamdalla alyasriy 2020). There are 1,097 images of CT scans in this dataset that belong to the three main categories of Benign, Malignant, and Normal. Figure 1 shows example images from each category and highlights the important morphological differences between cancerous, non-cancerous, and healthy lung tissue.

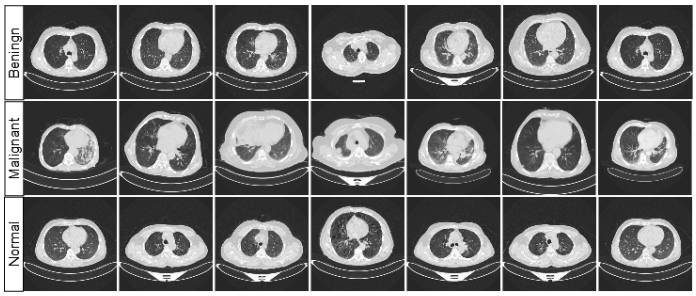

Figure 1 Sample CT Scan Images of Benign, Malignant, and Normal Lungs

In order to provide our procedures with a sound basis for our experiment, the dataset used in our studies was divided into three different datasets: training, validation and testing. The procedural split was stratified so as to ensure that the original distribution of cases within the various classes were retained across all three datasets; this allowed for the production of reliable classification models with minimal evaluation bias. As described in Table 1, our datasets used a 70/15/15 ratio to separate 767 examples for use during training; 164 examples were reserved for validation and 166 examples were held back for testing. The original distribution of classes consists of 120 examples of benign cases; 561 examples of malignant cases and 416 examples of normal cases demonstrating a large degree of class imbalance, especially regarding the absence of examples from the benign class. To compensate for the existing class imbalance and improve our models' ability to generalise and reduce the possibility of biased learning from the larger classes, advanced techniques, including data augmentation, were utilised in our methodological framework. The images were subsequently subjected to a rigorous preprocessing pipeline, including resizing and normalization, to prepare them for ingestion by the DL architectures.

Foundational Principles of Deep Learning Models

Convolutional Neural Networks (CNNs) are one of the first classes of deep learning (DL) architectures to significantly change how computer vision was done. CNNs were designed specifically to take advantage of the inherent spatial hierarchies in visual data, including images and volumes. The base of the CNN is a convolution operation wherein a set of learnable filters (also known as kernels) are slid across an input volume to perform a dot product at every spatial position between the filter weights and the corresponding input patch, producing a two-dimensional activation map that indicates the presence of specific features.

Table 1 Distribution of the Dataset into Training, Validation, and Test Sets

Classes	Original Dataset	Train (70%)	Validation (15%)	Test (15%)
Benign	120	84	18	18
Malignant	561	392	84	85
Normal	416	291	62	63
Total	1097	767	164	166

CNNs (Convolutional Neural Networks) are designed with two important rules in mind: first, that they utilize local connectivity and second, that they share parameters among all layers of the model. The purpose of these two inductive biases is to reduce the number of weights needed to train the CNN. The use of local connections allows each neuron to only connect to a small section of the previous layer's activation, or receptive field. This matches the structure of most natural images. By using the same weights across all locations in the image, the neural network is able to recognize a particular feature (e.g., a vertical line) at any place in the image. Using these two inductive biases limits the number of parameters that need to be learned in the model and helps prevent the model from overfitting.

CNN's architectural feature is its multilayer system that is structured in such a way that it learns to create a hierarchy of features. After a convolutional layer, a nonlinear activation function, like Rectified Linear Unit (ReLU), is typically utilized to help model the more complex and nonlinear relationships between the particular data inputs (features). Additionally, the convolutional layers, ReLU activation, and pooling (max pooling) layers are combined systematically throughout the CNN, this allows the CNN to produce various levels of abstraction over time, which provide a level of translational invariance (an image that has been translated has the same appearance). The initial convolutional layers learn basic primitives such as color gradients or edges, then the subsequent convolutional layers build onto these primitives to learn more complex structures and semantic information (i.e., textures, parts of objects, etc.). The final stage of this automated feature extraction process consists of a series of fully connected layers (the classification head of the CNN) which combine the high-level features and output the final feature vector, giving rise to a set of probabilities that represent the final classification outcome for the image in question.

Methodological Framework: Transfer Learning and Augmentation

In our approach to increasing our models' ability to generalize, we implemented transfer learning. We set the initial weights of our models using those learned from the prior training of the very large ImageNet dataset. Thus, our models are able to build upon the advanced feature extraction capabilities of these previous models. In order to create a model that is specific to the task of classifying pulmonary CT images, we removed the terminal classification layers of the ImageNet trained models and replaced them with a new random Dense Layer (N_Features X 3), which serves as our final Softmax classifier. This new Dense Layer has been specifically designed to fit the three-class structure of our problem. We trained our model in two distinct phases: (1) Feature Freezing - where only parameters of our new dense classifier were adjusted to fit the new data distribution and (2) Comprehensive End-to-End Fine-Tuning, where the parameters of all layers of the network were trained to adapt to very low learning rates and have been refined to classify lung nodules specifically according to their morphology.

To improve generalisation and avoid overfitting, especially considering our data set size, we've created a robust on-the-go augmentation pipeline based on the standard augmentation protocols provided via the PyTorch Image Models (timm) library. A main feature of the pipeline was to standardise the input dimensions of all images as they are re-sized to one of four (arbitrarily chosen) fixed resolutions (224x224 pixels). To preserve as many features as possible during the process of re-sizing, a random interpolation technique was used at each stage of re-sizing, where one of three different methods (bicubic, bilinear, or one of several other resampling methods) was randomly selected to use for each image. We instilled geometric invariance in our augmentation strategy through the use of Random Resized Cropping (scale between 0.08 and 1.0); as well as the use of Random Horizontal Flipping with probabilistic random selection (p=0.5). To eliminate photometric variability, which occurs in medical imaging due to differences in scanner protocol, we added Color Jittering (variance factor of 0.4), which introduced a stochastic element to the brightness, contrast, and saturation of input data. While label-mixing regularization techniques are common in natural image classification, we purposely did not employ them in this study (label-mixing coefficients set to 0.0) because we wished to maintain strict anatomic fidelity and the clear definition of the anatomic boundaries defining pulmonary nodules critical for accurate radiological evaluation (Mumuni *et al.* 2024; Wang *et al.* 2024).

Experimental Configuration and Training Procedure

In order to provide complete transparency regarding the methodology used in our research and also to allow for repeatability of the results, we conducted all of our experiments in a clearly defined, standardized computer environment. The pipeline for both training and evaluating the models was completed on a powerful workstation that contained an Intel® Core™ Ultra 7 265K CPU, 32.0 GiB of RAM, and a NVIDIA GeForce RTX™ 5090 (24GB) GPU for CUDA acceleration. The operating system on the workstation was Ubuntu 24.04.3 LTS (with Linux kernel 6.14.0-35-generic). The deep learning (DL) environment was created with Python (v3.10) using the PyTorch (v2.9.0) framework. Main libraries for data handling, training, and analysis included torchvision (v0.24.0), numpy (v2.3.4), Pillow (v12.0.0), scikit-learn (v1.7.2 - for calculating metrics), and the PyTorch Image Models (timm) library for creating and using models and training procedures.

Each individual model was trained according to the predetermined configuration parameters outlined in this document. The Stochastic Gradient Descent (SGD) Optimizer (option: sgd) was used with a momentum of 0.9 and a weight decay value of 0.000020000 (2.0e-05). A learning rate schedule using a Cosine Annealing rate scheduler (option: cosine was used to

schedule the learning rate from an initial value of 0.000010000 (warmup_learning_rate) through five successive epochs (the warmup epoch) until reaching the base learning rate. We trained every model for a maximum of 300 Epochs (total_epoch: 300), where each Epoch consists of 16 training batches (batch_size: 16). Each trained model also used label smoothing with a smoothing factor of 0.1 (smoothing: 0.1), which helps to ensure that the model is well-calibrated with respect to the expectations of its input and output data. In addition to these training parameters, we employed an early stopping strategy to prevent overfitting and discover the ideal model state. This method monitors the model's validation loss during training and terminates the training process whenever validation loss does not decrease for ten Epochs (patience_epochs: 10). When stopping, we return to the best state of the model (i.e., the best-trained version of the model) by relying on the lowest recorded validation loss.

Performance Evaluation Metrics

We performed a thorough evaluation of Model Performance on a separate Testing Set using a battery of Evaluation Metrics. Although the Aggregate Accuracy provides an overall measure of how accurate the results are, it can be deceptive in cases where there is a class imbalance. Thus, we utilized Precision, Recall and the F1-Score for a more in-depth analysis of the Models Performance. Precision is a way to express the proportion of positive predictions that are accurate; Precision is an indicator of how trustworthy a Model is by showing what portion of the positive predictions are correct. Recall (which is also referred to as Sensitivity) expresses how well a Model can detect all of the true positives in a sample. The F1-Score is defined as the harmonic mean of Precision and Recall and thus provides a composite measure of a Model Performance. The mathematical equations can be found below:

$$\text{Accuracy} = \frac{TP + TN}{TP + TN + FP + FN} \tag{1}$$

$$\text{Precision} = \frac{TP}{TP + FP} \tag{2}$$

$$\text{Recall} = \frac{TP}{TP + FN} \tag{3}$$

$$\text{F1-score} = 2 \cdot \frac{\text{Precision} \cdot \text{Recall}}{\text{Precision} + \text{Recall}} \tag{4}$$

Here, TP, TN, FP, and FN denote True Positives, True Negatives, False Positives, and False Negatives, respectively. For our multiclass context, these metrics were computed independently for each class and then macro-averaged to yield a single, aggregate score that reflects the model's broadly performance across all categories.

EXPERIMENTAL RESULTS

We benchmarked five distinct architectures (ConvNeXt Base, ResNet50, EfficientNetV2 Small, InceptionV4, and Xception) on the IQ OTH NCCD dataset to verify their diagnostic utility. To guarantee an unbiased assessment, we trained each network within an identical computational environment using a fixed set of hyperparameters. Table 2 provides a numerical summary of the performance metrics, whereas Figure 2 depicts the confusion matrices to reveal category specific classification patterns.

As presented in Table 2, the experimental results reveal significant variations in performance across the tested architectures. Among the evaluated models, InceptionV4 demonstrated the most robust performance regarding clinical safety, achieving the highest overall accuracy of 0.988 and a macro-averaged F1-score of 0.976. This performance notably surpasses the baseline ResNet-50 model, which yielded the lowest accuracy of 0.939 and an F1-score of 0.870. While computational efficiency is a critical factor for clinical deployment, a clear trade-off was observed between model complexity and diagnostic precision. Although EfficientNetV2 Small demonstrated remarkable efficiency with the lowest parameter count (20.18M) and computational cost (5.419 GFLOPs), its accuracy (0.969) remained lower than that of the more complex InceptionV4. Consequently, despite its higher computational demands (12.245 GFLOPs), InceptionV4 provided the most robust balance between sensitivity and specificity, justifying its prioritization for medical scenarios where diagnostic accuracy is paramount.

Addressing the critical concern of class imbalance inherent in the dataset, where Benign cases are significantly underrepresented compared to Malignant and Normal cases, we analyzed the per-class performance using the confusion matrices illustrated in Figure 2. Typically, models trained on imbalanced data exhibit a bias toward the majority class, resulting in poor sensitivity for the minority category. However, our results provide ex-post validation of the applied on-the-fly augmentation strategy. As evidenced by the confusion matrices in Figure 2, the InceptionV4 model demonstrated remarkable calibration, correctly classifying 17 out of 18 benign cases, yielding a 0.944 recall for this minority class. This confirms that the dynamic augmentation pipeline effectively counteracted the data imbalance, allowing the model to learn distinctive features for underrepresented benign nodules without overfitting to the majority 'Malignant' or 'Normal' categories.

The superior performance of InceptionV4 as depicted in Figure 2, particularly in its ability to resolve the subtle morphological differences between benign nodules and normal tissue, can be attributed to its specialized architectural design. Unlike standard serial CNNs such as ResNet-50 or Xception that utilize fixed-size kernels, the Inception architecture employs multiple kernel sizes (1×1, 3×3, 5×5) simultaneously within each inception block. This multi-branch structure allows the network to capture multi-scale spatial features effectively, processing both the fine-grained textural details characteristic of small benign nodules and the broader morphological structures of larger malignant masses in parallel. This capability is particularly advantageous for analyzing lung CT scans where nodule size and texture variance are key diagnostic indicators, enabling InceptionV4 to outperform architectures restricted to single-scale processing in this specific application.

Visual Validation of Model Focus with Grad-CAM++

One of the most significant barriers to the clinical adoption of deep learning (DL) systems is their inherent "black-box" nature, which often obscures the underlying decision-making process. In the high-stakes environment of pulmonary oncology, achieving high statistical accuracy is insufficient; clinicians must be able to verify that the model is making its predictions based on relevant pathological features rather than spurious artifacts. To address this requirement for clinical transparency and foster trust, we utilized Grad-CAM++ to generate saliency maps for our top-performing architecture, InceptionV4. This visualization technique produces class-specific heatmaps that highlight the localized regions of the CT scan that most heavily influenced the network's final classification. By mapping these gradients back to the input image, we can qualitatively assess whether the model's focus aligns with established radiological indicators of benignity and malignancy.

As illustrated in Figure 3, the Grad-CAM++ visualizations provide compelling evidence of InceptionV4's diagnostic reliability.

Table 2 Comparison of Performance Metrics and Computational Complexity of the Models

Models	Accuracy	Precision	Recall	F1-score	Params	GFLOPs
ConvNeXt-Base	0.969	0.945	0.933	0.939	87.57M	30.707
ResNet-50	0.939	0.893	0.854	0.870	23.51M	8.263
EfficientNetV2 Small	0.969	0.957	0.920	0.936	20.18M	5.419
Inception V4	0.988	0.976	0.976	0.976	41.15M	12.245
Xception	0.975	0.980	0.925	0.948	20.81M	9.194

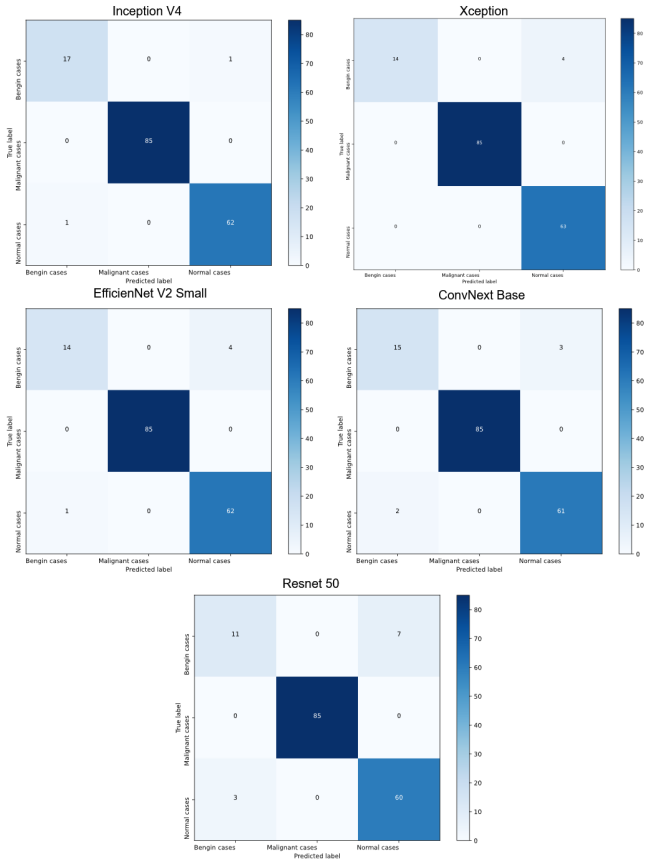

Figure 2 Confusion matrices comparing the class-wise prediction performance of the five DL models (InceptionV4, Xception, EfficientNetV2 Small, ConvNeXt Base, and ResNet-50) on the test dataset. The matrices highlight the number of True Positives (diagonal) and misclassifications (off-diagonal) for Benign, Malignant, and Normal classes.

For correctly classified cases, particularly the malignant ones where the model achieved a perfect recall rate of 1.00, the heatmaps demonstrate precise localization on the actual lesion or nodule. This localized attention is a direct result of InceptionV4's multi-scale architectural design, which utilizes parallel convolutional branches with varying kernel sizes (1×1, 3×3, and 5×5) to simultaneously capture both fine-grained textural primitives and broader morphological distortions. The saliency maps in Figure 3 confirm that the network successfully ignores non-informative anatomical structures, such as the chest wall or vascular segments, and instead prioritizes the subtle morphological cues that distinguish benign lesions from healthy tissue. This visual validation reinforces the quantitative results, confirming that InceptionV4 functions as a robust decision support tool by focusing on the same pathological regions a radiologist would examine.

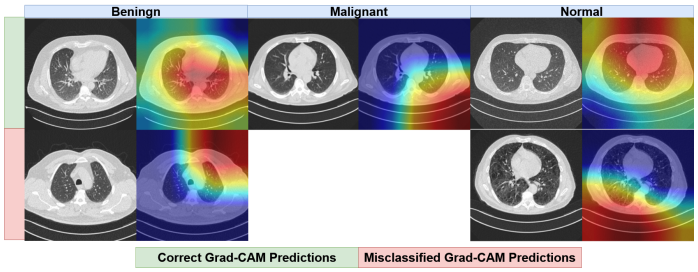

Figure 3 Visual validation of diagnostic focus using Grad-CAM++ saliency maps for the InceptionV4 architecture across Benign, Malignant, and Normal lung CT categories, illustrating both correct and misclassified instances.

DISCUSSION

The accurate characterization of pulmonary nodules represents a pivotal challenge in modern oncology where the distinction between benign lesions and malignant tumors directly dictates patient survival. While DL has emerged as a transformative force in this domain, the clinical adoption of these systems hinges not on marginal improvements in accuracy but on their reliability in preventing missed diagnoses. Within this context, our study reveals a critical insight: while overall accuracy is a standard benchmark in machine learning, the true utility of an AI system in medical imaging is defined by its safety profile. Among the diverse architectures analyzed, InceptionV4 emerged not merely as a statistical leader but as the most clinically robust candidate. It achieved an overall accuracy of 0.988 and a macro-average F1-score of 0.976. However, the defining characteristic of this performance, and the primary contribution of this work, is the model's perfect sensitivity as evidenced by a 1.00 recall rate for malignant cases. In the high-stakes domain of lung cancer screening where a missed diagnosis can drastically alter patient prognosis, the elimination of false negatives is paramount. This capability positions the proposed framework as a reliable safety net for radiologists since it prioritizes patient survival over marginal gains in general classification metrics.

This superior sensitivity is not accidental but stems from the specific inductive biases inherent in the InceptionV4 architecture.

Unlike serial backbones such as ResNet-50 which rely on fixed receptive fields, InceptionV4 utilizes parallel convolutional branches with varying kernel sizes. This multi-scale feature extraction allows the network to simultaneously resolve the fine-grained textures of small benign nodules and the gross morphological distortions typical of malignant masses. This architectural advantage effectively addresses the challenge of distinguishing subtle benign lesions from normal tissue, a task where single-scale models often falter.

We acknowledge that recent benchmarks on the IQ-OTH/NCCD dataset have reported marginally higher numerical accuracies, such as those achieved by Chaddad et al. using attention-enhanced ResNet+, or Sheikh Akbari et al. via ViT. However, the slight performance gap in our results reflects a deliberate methodological trade-off. Unlike recent studies that focus solely on maximizing accuracy through complex hybrid models, our work prioritizes architectural explainability and clinical safety. We demonstrate that the multi-scale processing of InceptionV4 effectively eliminates false negatives without the need for aggressive synthetic data generation. Consequently, we consciously excluded label-altering augmentation techniques like Mixup or Cutmix to preserve the strict anatomical fidelity of the CT images. While such techniques might artificially boost validation metrics, they risk introducing artifacts that are not clinically representative. Therefore, the perfect malignant recall achieved by InceptionV4 without synthetic pixel interpolation confirms its practical utility as a robust decision support tool.

CONCLUSION

The findings of this study highlight the necessity of rethinking conventional model evaluation practices by moving beyond isolated accuracy metrics toward a more comprehensive assessment of diagnostic safety and reliability. The demonstrated robustness and reproducibility of the proposed transfer learning framework underscore its practicality and suitability for integration into standard medical imaging workflows. By complementing radiological expertise and mitigating inter-observer variability, such automated systems have the potential to function as effective clinical decision support tools. Looking ahead, future research will focus on validating the proposed approach across multi-center datasets and incorporating explainable artificial intelligence techniques to enhance clinical trust, transparency, and interpretability.

Despite the promising results, we must acknowledge some limitations to ensure a balanced scientific interpretation of this study. A primary limitation is that the results are from a single data source, the IQ-OTH/NCCD dataset. While this dataset serves as a standard benchmark, evaluating models on a single cohort is not fully objective, as differences in CT scanner protocols, reconstruction kernels, and patient demographics across institutions can significantly impact model performance. Furthermore, while a test set size of 166 images is sufficient for statistical indices, it is not an effective test data set. This limited sample size creates the risk of statistical variance, and the observed performance differences should be tested with larger, multicenter, and diverse datasets to verify their robustness across various clinical settings. Unfortunately, due to the lack of publicly available datasets, we must accept these limitations.

Additionally, the dataset exhibits a critical class imbalance, with the "Benign" class being significantly underrepresented compared to "Malignant" and "Normal" cases. Although we employed a robust data augmentation pipeline to mitigate this issue, the confusion matrices reveal that the majority of misclassifications occurred within the benign class. While InceptionV4 handled this imbalance effectively, other models like ResNet-50 struggled to distinguish benign nodules from normal tissue, highlighting that algorithmic bias toward the majority class remains a challenge. Furthermore, this study's scope was intentionally limited to the CT imaging modality. We acknowledge that a multimodal approach, integrating data from other sources such as Positron Emission Tomography (PET) or histopathological slides, was not explored but presents a valuable direction for future research. Another limitation is the lack of explainability; as DL models function as "black boxes," high accuracy does not guarantee that the model is focusing on clinically relevant pathological features. Future research will aim to address these shortcomings by validating the top-performing InceptionV4 model on external, large-scale datasets such as LIDC-IDRI to ensure cross-center generalizability. We also plan to integrate XAI modules, such as Grad-CAM, to visualize the decision-making process and ensure alignment with radiological expertise, alongside exploring ensemble methods that combine the high sensitivity of InceptionV4 with the efficiency of lightweight models.

Ethical standard

Ethical approval was not required for this study as it relied exclusively on the publicly available 'IQ-OTH/NCCD Lung Cancer Dataset'. Since the data consists of pre-existing, anonymized CT images and does not involve direct interaction with human subjects or animals, institutional review board (IRB) certification is not applicable.

Availability of data and materials

The "IQ-OTH/NCCD Lung Cancer Dataset" used for this study is publicly available and accessible, as cited in reference (32).

Conflicts of interest

The authors declare that there is no conflict of interest regarding the publication of this paper.

LITERATURE CITED

Akbari, A. S., A. Kumar, B. R. Reddy, K. K. Singh, and M. Takei, 2024 Vision transformer based automated model for enhancing lung cancer classification. In *2024 IEEE International Conference on Imaging Systems and Techniques (IST)*, pp. 1–6, IEEE.

Attallah, O. and I. Pacal, 2026 Impact of magnification on deep learning approaches through comprehensive comparative study of histopathological breast cancer classification. Biomedical Signal Processing and Control **113**: 108973.

Ayesha, N., I. H. Hassan, A. R. Mirdad, and A. R. Khan, 2025 Efficientnet deep learning model for lung cancer early diagnosis from computed tomography scan images with transfer learning. Journal of Advances in Information Technology **16**.

Baji, S. R., S. B. Bagal, S. V. Chaudhari, and B. S. Agarkar, 2025 Effective diagnosis of lung cancer using pyramid quantum convolutional neural network with migrating walrus algorithm on ct scan images. Biomedical Materials & Devices pp. 1–26.

Çakmak, Y., 2025 Machine learning approaches for enhanced diagnosis of hematological disorders. Computational Systems and Artificial Intelligence **1**: 8–14.

Çakmak, Y. and A. Maman, 2025 Deep learning for early diagnosis of lung cancer. Computational Systems and Artificial Intelligence **1**: 20–25.

Çakmak, Y. and N. Pacal, 2025 Deep learning for automated breast cancer detection in ultrasound: A comparative study of four cnn architectures. Artificial Intelligence in Applied Sciences **1**: 13–19.

Çakmak, Y. and J. Zeynalov, 2025 A comparative analysis of convolutional neural network architectures for breast cancer classification from mammograms. Artificial Intelligence in Applied Sciences **1**: 28–34.

Chaddad, A., J. Peng, and Y. Wu, 2025 Classification based deep learning models for lung cancer and disease using medical images. IEEE Transactions on Radiation and Plasma Medical Sciences .

Chowdhury, A., T. Moni, A. A. N. Tushar, M. P. Hossain, and M. A. Rahaman, 2024 An improved deep learning model for early stage lung cancer detection from ct scan images. In *2024 6th International Conference on Sustainable Technologies for Industry 5.0 (STI)*, pp. 1–6, IEEE.

Deepa, V. *et al.*, 2024 Fossil_net lung cancer prediction and classification from ct images using convolution neural networks. In *2024 2nd International Conference on Computing and Data Analytics (ICCDA)*, pp. 1–5, IEEE.

Deepika, R., P. Shanmugam, K. Moorthi, P. M. Kumar, S. Swarna, *et al.*, 2024 Optimized transfer learning model for lung cancer stage classification using computed tomography images. In *2024 International Conference on IoT Based Control Networks and Intelligent Systems (ICICNIS)*, pp. 912–917, IEEE.

Dev, S., P. S. Roy, N. Chakraborty, and R. Sarkar, 2025 Lung cancer identification from ct scans using a soft-attention enabled deep transfer learning model. In *2025 3rd International Conference on Intelligent Systems, Advanced Computing and Communication (ISACC)*, pp. 254–259, IEEE.

hamdalla alyasriy, 2020 The iq-othnccd lung cancer dataset **1**.

Ince, S., I. Kunduracioglu, A. Algarni, B. Bayram, and I. Pacal, 2025 Deep learning for cerebral vascular occlusion segmentation: a novel convnextv2 and grn-integrated u-net framework for diffusion-weighted imaging. Neuroscience **574**: 42–53.

Jozi, N. S. and G. A. Al-Suhail, 2024 Lung cancer detection: The role of transfer learning in medical imaging. In *2024 International Conference on Future Telecommunications and Artificial Intelligence (IC-FTAI)*, pp. 1–6, IEEE.

Lad, S., B. Chafekar, and P. Bide, 2024 Lung cancer classification using deep learning: A comprehensive approach with modified convolutional neural networks. In *2024 International Conference on Computational Intelligence and Network Systems (CINS)*, pp. 1–6, IEEE.

Lavanya, G., M. Muthulakshmi, M. Latha, A. Keerthinathan, P. V. Krishh, *et al.*, 2024 Deep learning for enhanced detection and characterization of pulmonary nodules. In *2023 4th International Conference on Intelligent Technologies (CONIT)*, pp. 1–7, IEEE.

Mahmud, M. R., H. Fardin, M. I. H. Siddiqui, A. H. Sakib, and A. Al Sakib, 2025 Hybrid deep learning for interpretable lung cancer recognition across computed tomography and histopathological imaging modalities. International Journal of Science and Research Archive [Internet] pp. 1798–810.

Moldovanu, S., G. Tăbăcaru, and M. Barbu, 2024 Convolutional neural network–machine learning model: hybrid model for meningioma tumour and healthy brain classification. Journal of Imaging **10**: 235.

Mumuni, A., F. Mumuni, and N. K. Gerrar, 2024 A survey of synthetic data augmentation methods in machine vision. Machine Intelligence Research 2024 21:5 **21**: 831–869.

Munteanu, D., S. Moldovanu, G. Tăbăcaru, and M. Barbu, 2025 Influence of symmetric and asymmetric cae-cnn on colon cancer histopathological images classification. In *2025 33rd Mediterranean Conference on Control and Automation (MED)*, pp. 203–208, IEEE.

Muqeet, M. S. *et al.*, 2025 Enhancing early detection of chronic obstructive pulmonary disease using high-resolution mri and advanced deep learning techniques. In *2025 Global Conference in Emerging Technology (GINOTECH)*, pp. 1–8, IEEE.

Pacal, I. and O. Attallah, 2025 Inceptionnext-transformer: A novel multi-scale deep feature learning architecture for multimodal breast cancer diagnosis. Biomedical Signal Processing and Control **110**: 108116.

Rai, N., S. Khatri, and D. Risal, 2025 Explainable ai technique in lung cancer detection using convolutional neural networks. arXiv preprint arXiv:2508.10196 .

Ruprah, T. S., B. Regmi, S. B. Jadhav, and S. Singh, 2024 Early stage lung cancer detection using deep learning. In *2024 MIT Art, Design and Technology School of Computing International Conference (MITADTSoCiCon)*, pp. 1–6, IEEE.

Shakya, S. R., E. Ceh-Varela, and I. Sanjaya, 2025 Lung cancer classification using deep learning models for edge computing. a comparative analysis. In *2025 IEEE International Conference on AI and Data Analytics (ICAD)*, pp. 1–6, IEEE.

Siegel, R. L., T. B. Kratzer, A. N. Giaquinto, H. Sung, and A. Jemal, 2025 Cancer statistics, 2025. Ca **75**: 10.

Tătaru, I., S. Moldovanu, O.-M. Dragostin, C. L. Chiţescu, A.-S. Zamfir, *et al.*, 2025 Auto machine learning and convolutional neural network in diabetes mellitus research—the role of histopathological images in designing and exploring experimental models. Biomedicines **13**: 1494.

Venkatraman, K. and S. N. P. S. Reddy, 2024 Augmenting clinical decisions with deep learning lung cancer image abnormality segmentation. In *2024 14th International Conference on Cloud Computing, Data Science & Engineering (Confluence)*, pp. 674–678, IEEE.

Wang, Z., P. Wang, K. Liu, P. Wang, Y. Fu, *et al.*, 2024 A comprehensive survey on data augmentation .

Zafar, S., J. Ahmad, Z. Mubeen, and G. Mumtaz, 2024 Enhanced lung cancer detection and classification with mrmr-based hybrid deep learning model. Journal of Computing & Biomedical Informatics **7**.

How to cite this article: Guven, U. B., Cakmak, Y., and Pacal, I. Evaluation of Deep Learning Architectures for Pulmonary CT Lesion Classification Highlighting Diagnostic Performance. *Chaos and Fractals*, 3(1), 47-53, 2026.

Licensing Policy: The published articles in CHF are licensed under a Creative Commons Attribution-NonCommercial 4.0 International License.

ADBA Chaos and Fractals
Cutting-Edge Scientific Solutions

e-ISSN: 3023-8951
RESEARCH ARTICLE
Vol.3 / No.1 / 2026 / pp.54-60
https://doi.org/10.69882/adba.chf.2026018

Nonlinear Effects of Zero-Crossing Detection Based Firing Angle Power Control on Lighting Performance

Dursun Kerem Karaduman [α,1], **Kenan Gençol** [β,2] **and Serkan Dişlitaş** [γ,3]

[α]Hitit University, Graduate School, Department of Interdisciplinary Energy Systems Engineering,19030, Corum, Türkiye, [β]Hitit University, Faculty of Engineering and Natural Sciences, Department of Electrical and Electronics Engineering,19030, Corum, Türkiye, [γ]Hitit University, Faculty of Engineering and Natural Sciences, Department of Computer Engineering,19030, Corum, Turkiye.

ABSTRACT This paper presents the design, development, and performance evaluation of a single-phase microcontroller-based SCR (Silicon Controlled Rectifier) power control system employing a Zero-Crossing Detection (ZCD) technique for precise AC power regulation. The proposed embedded hardware architecture integrates a ZCD-based control unit, a bidirectional SCR driver circuit, and an SCR module with a power conditioning unit. The control algorithm, implemented on a microcontroller platform, performs precise zero-cross detection via hardware interrupts, computes the firing angle (), and generates synchronized triggering pulses through optically isolated driver circuits. The system supports multiple operational modes, firing angle control, integral cycle control, and on/off control,enabling flexible load management. Experimental validation was performed using resistive loads and a 220 V, 42 W incandescent bulb. The results demonstrate accurate bidirectional triggering and stable load voltage control across firing angles from 0° to 180°, corresponding to delay times (td) of 0–10 ms. Notably, the measured RMS voltage, apparent power and perceived illumination reached their peak at = 45°, confirming a nonlinear relationship between the firing angle and output characteristics. The developed prototype provides rapid and stable power regulation between 0% and 100%, making it suitable for industrial heating and lighting systems. Future research will incorporate adaptive and soft-start control strategies to enhance operational efficiency and compatibility with resistive–inductive loads.

KEYWORDS
Zero crossing detection
Firing angle control
Nonlinearity
Embedded system

INTRODUCTION

With the use of electrical energy, rapid and widespread technological advancements have emerged that facilitate our lives in every field, primarily in industry, healthcare, and education (Rashid 2014). The rapid increase in the global demand for electrical energy necessitates extensive research into the generation, transmission, distribution, utilization, and management of electrical energy in terms of efficiency, cost, and reliability (International Energy Agency 2023). The accurate control of the electrical power required in industrial and consumer electronics applications is a crucial subject that must first be investigated and developed (Bose 2020).

In this context, in industrial applications involving lighting, heating, and asynchronous motors, areas that constitute the main fields of electrical energy consumption, power control systems play a significant role in ensuring the smooth delivery of the required power to the load, the efficient and reliable use of energy, and overall energy savings. For this purpose, extensive theoretical and practical studies have been conducted on power control systems. Fundamentally, power electronic circuits form the basis of power control systems. A power electronic circuit essentially consists of two main parts: the power section and the control section. In sectoral applications, various methods are employed to regulate the power supplied to the system through control circuits, which adjust it according to the requirements of the load (Bose 2020; Hart 2011; Rashid 2014).

Efficiency is a key issue in power control; however, preventing the occurrence of harmonic disturbances is also a critical problem that must be addressed. The use of mechanical relays in switching operations can cause arcing at peak voltage and lead to various related issues. Due to their advantages, such as the absence of moving parts, fast switching capability, and noiseless operation, semiconductor chips are preferred for power control and switching. In this regard, thyristor-based AC power control systems are widely used in industrial applications (Mauriac *et al.* 2004; Texas Instruments 2022).

In the literature, there are numerous studies focusing on the design, manufacturing, and performance enhancement of solid-state power control devices that employ methods such as Zero Crossing Detection (ZCD), phase control, and integral cycle control (Ashraf *et al.* 2020). Additionally, several studies have been conducted on ZCD-based approaches related to power control, management, and safety. For example, Al-Baihani *et al.* (2021) conducted a simulation and experimental modeling study on inverter triggering circuits using a microcontroller-based ZCD method. Kurak and Erdemir (2013) designed and simulated a triggering circuit based on the phase control principle of a PIC microcontroller-driven

Manuscript received: 28 November 2025,
Revised: 11 January 2026,
Accepted: 12 January 2026.

[1]dursunkaraduman05@gmail.com
[2]kenangencol@hitit.edu.tr(**Corresponding author**).
[3]serkandislitas@hitit.edu.tr

thyristor (SCR – Silicon-Controlled Rectifier). In a recent study, Yurtcu (2021) developed a fast and cost-effective hybrid system consisting of an electronic switch and a residual current circuit breaker, both operating on the principle of zero-cross detection, suitable for high-power applications. Rustemli and Agrali (2023) implemented a microcontroller-based application for the precise and practical speed control of AC universal motors via a computer interface using the firing angle control method to regulate motor power.

In thyristor-based power control circuits, performing zero-cross detection, adjusting necessary timing parameters, and driving operations complicate the design of the required electronic circuits. Therefore, using microcontroller-based zero-cross detection methods to drive SCRs simplifies the overall system structure. For this goal, in this study, a hardware and software-based embedded system design of a single-phase SCR-based power control device employing the ZCD method has been developed to achieve fast and efficient power control for industrial applications. The electrical performance characteristics of the developed prototype were obtained and analyzed.

The rest of the paper is organized as follows. The second section focuses on the basic principles and control methods of ZCD-based power control. The third section presents the hardware and software aspects of the designed and implemented microcontroller-based single-phase power control device operating on the ZCD method using SCRs. The fourth section analyzes the experimental performance of the developed system and presents the results. Finally, the paper is concluded by providing a general evaluation of the designed system and offering insights into its applicability and potential for further improvement.

POWER CONTROL WITH ZERO CROSSING DETECTION (ZCD)

In this section, we describe the basic principles of ZCD and the power control methods employing ZCD. In particular, we focus on the firing angle control method which also forms the theoretical basis of the designed system in this study.

Zero Crossing Detection

Zero Crossing Detection (ZCD) is the process of determining the precise instant at which the voltage of an AC sinusoidal signal crosses zero, either from the positive to the negative alternation or vice versa from the negative to the positive alternation. It is a method widely used in electronic power applications to synchronize control signals with the AC mains. In a sinusoidal waveform, zero crossing normally occurs twice during each cycle, once while the waveform rises and once while it falls (Hart 2011; Zheng and Zhang 2012).

Figure 1 illustrates the firing-angle-based triggering operation using the ZCD method. With the ZCD technique, both the falling (positive-to-negative) and rising (negative-to-positive) zero-crossing points of the supply signal within a period T are detected. According to the determined firing angle (α), a triggering signal is generated at the end of a corresponding firing delay (t_d), allowing the SCRs to conduct in both the positive and negative triggering regions (Hart 2011).

Various solutions exist for performing ZCD and output triggering, including transistor-based, optocoupler-based, operational amplifier (OP-AMP)–based and microcontroller-based designs. Among them, microcontroller-based systems enable faster, more efficient, and more user-friendly control of the output power applied to the load through software-driven ZCD operation, ensuring

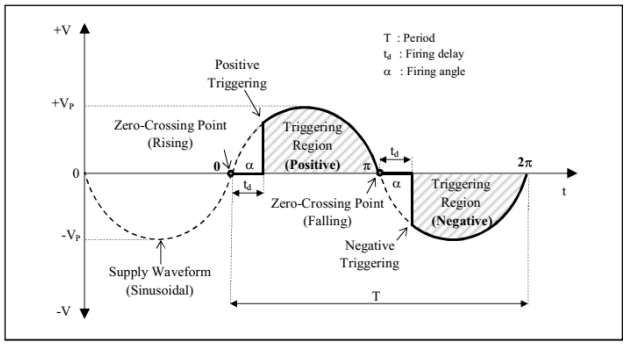

Figure 1 Firing-angle triggering based on the ZCD method

that the desired power level is delivered more precisely (Akyasan and Hasirci 2016; Bose 2020).

In power control applications, various methods such as firing angle control, integral cycle control, and on/off control are employed based on the principle of thyristor triggering using the Zero Crossing Detection (ZCD) technique.

Firing Angle Control Method

The fundamental principle of the firing angle control is that the triggering signal is applied after a predetermined delay time, corresponding to a specific firing angle (α) measured from the zero-crossing point of the AC supply that is determined by the ZCD method. This allows the output voltage to be applied to the load in proportion to the desired average power to be delivered. According to the method, the load voltage (V_L) at the output, as a function of the supply peak voltage (V_P) and the firing angle (α), can be expressed as in Eq. (1) (Al-Mawsawi *et al.* 2012):

$$V_{\text{rms}} = V_m \sqrt{\frac{1}{2\pi}\left(\pi - \alpha + \frac{1}{2}\sin(2\alpha)\right)} \tag{1}$$

This method enables precise regulation of the power delivered to the load, providing energy savings since only the required amount of current is utilized. It is primarily employed in inductive load applications, such as motors and transformers, but it can also be used with certain resistive loads where soft-start operation is desired to limit sudden inrush currents.However, due to the nature of phase control, the power factor is typically less than unity (Cos < 1), and the method tends to generate a relatively high level of harmonic noise in the system (Hart 2011; Rashid 2014; Texas Instruments 2022).

Phase-angle control is widely used in heating, lighting, and similar AC load control applications because of its flexibility and responsiveness in adjusting power delivery. In general, this method is particularly advantageous in energy-saving applications, in systems that operate continuously for long durations, and in processes requiring stable operation. It is also suitable for environments where frequent ON/OFF switching of the system places stress on the power lines, where the supply voltage is unstable, or where a long operational lifetime of heating elements is desired Rashid (2014). Figure 2 illustrates the output waveforms for different firing angles.

THE DESIGNED SYSTEM

In this section, we present the hardware and software aspects of the designed and implemented microcontroller-based single-phase power control device operating upon the ZCD method using SCRs.

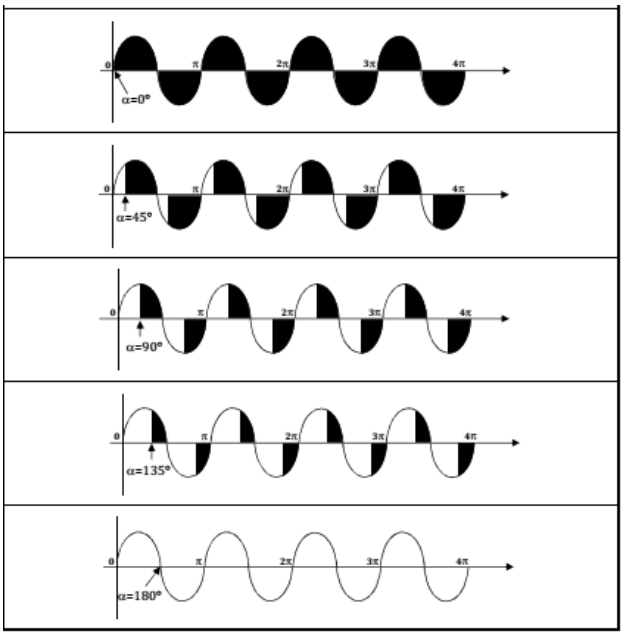

Figure 2 Output waveforms of the supply signal under firing angle control

System Hardware

The general block diagram of the designed system is shown in Figure 3. The system consists of a ZCD-based control unit, an SCR driver unit, an SCR module, and a power unit.

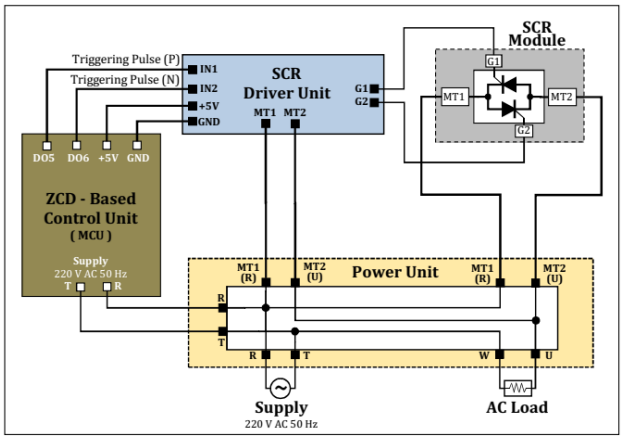

Figure 3 General block diagram of the designed system

The ZCD-based control unit includes circuits responsible for generating rectified and ZCD signals from the mains voltage, as well as for receiving reference input values from the user, displaying them on the screen, and performing system control via a microcontroller-based platform as shown in Figure 4.

For AC power control, a dual-SCR module (IXYS MCC26-12io8B) with a current rating of 27 A and a voltage rating of 1.2 kV was employed in the designed system, as shown in Figure 5. In this SCR module, the G1 and G2 gate terminals (pins 5 and 6) are used for triggering the positive (+) and negative (–) alternations of the AC supply signal, respectively. Terminals 2 and 3 are connected together and used as MT1, while terminal 1 serves as MT2. With this configuration, the SCR module operates as two

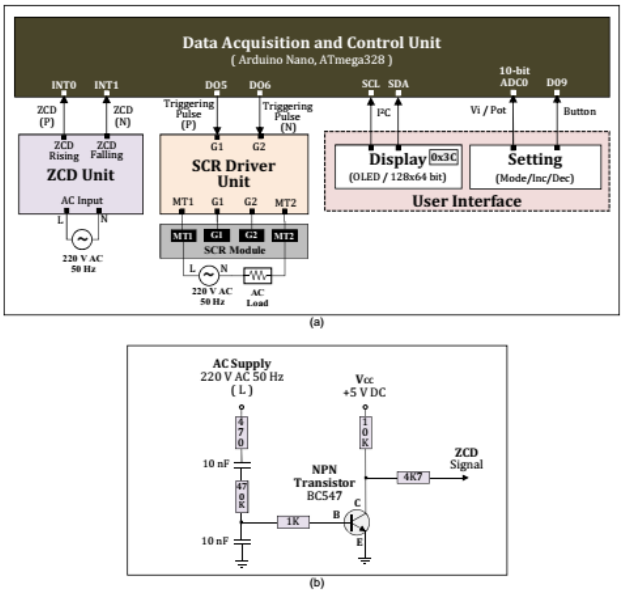

Figure 4 ZCD based control unit (a) Block diagram (b) ZCD circuit

thyristors connected in anti-parallel, allowing bidirectional control of AC power.

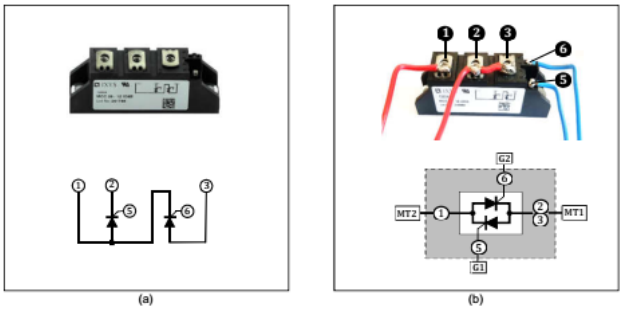

Figure 5 Connection principles of the SCR module: (a) Standard module (b) Back-to-back connected module

To achieve power control on the load side, a microcontroller-based bidirectional SCR driver circuit was designed based on the Zero Crossing Detection (ZCD) method as shown in Figure 6. For each alternation (positive and negative) of the supply signal, the corresponding ZCD signals are detected through the INT0 and INT1 interrupt inputs of the microcontroller, triggered respectively by rising and falling edges. Based on the desired firing angle (), the microcontroller calculates a delay time (td), after which triggering pulses generated from digital output pins D5 and D6 are amplified through NPN transistors and applied to the G1 and G2 gate terminals of the two anti-parallel SCRs to initiate conduction. For galvanic isolation between the control and power circuits, optocoupler ICs with triac-triggered outputs were used. Diodes at the optocoupler outputs ensure unidirectional current flow, thus enabling single-direction triggering for each SCR. In the driver circuit, the AC supply and load are connected in series between the MT1 and MT2 main terminals of the SCRs.For proper operation, the L-phase of the mains source must be connected to the MT1 terminal, while the N-neutral line is connected to the MT2 terminal through the AC load.

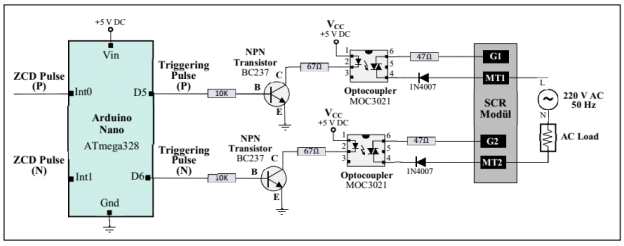

Figure 6 Microcontroller based bidirectional SCR driver circuit employing the ZCD principle

System Software

An embedded system software was developed for the SCR-based microcontroller power control system to perform data acquisition, system control, and the generation of triggering pulses according to the desired output power level or ratio determined from detected ZCD points. Figure 7 shows the flowchart of the embedded software algorithm designed to generate SCR triggering pulses using the ZCD method. At the start of execution, the algorithm receives reference configuration values such as power control mode, firing angle, and power ratio.

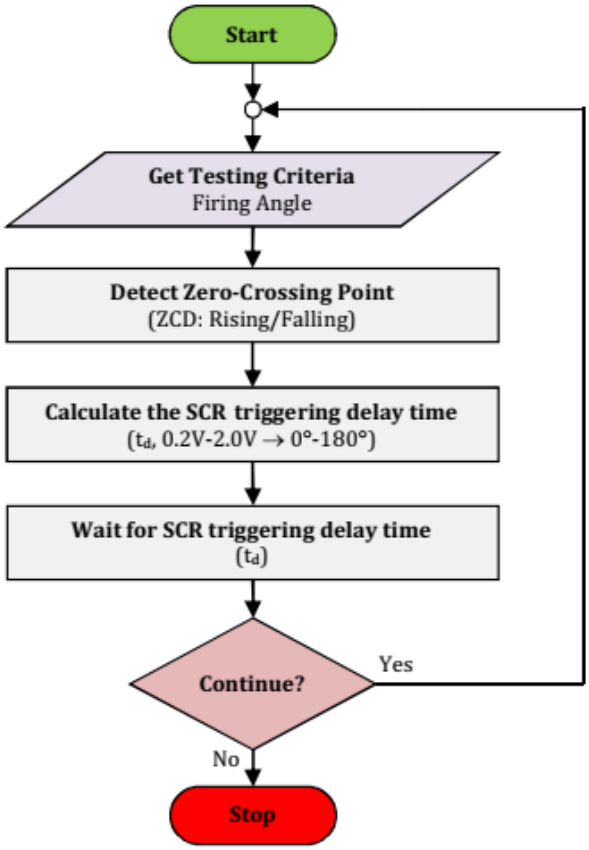

Figure 7 General flowchart of the embedded system software

After initialization, the system identifies the zero-crossing points of the supply signal through rising and falling edge interrupts on the microcontroller's ZCD input pins.Depending on the selected power control mode, the system operates in firing angle control, integral cycle control, or on/off control.

In firing angle control mode, the microcontroller computes the delay time (td) corresponding to the desired firing angle between 0°–180°. After this delay, triggering pulses are generated at the output pins, turning on the SCRs. In integral cycle control mode, the microcontroller determines a cycle pattern according to the desired output power ratio (0–100%) and delivers triggering pulses for the selected cycles, ensuring conduction only during those intervals. In on/off control mode, the output is either enabled or disabled at the zero-crossing point depending on the state of the on/off control signal. The system operates continuously in this cyclic manner, updating its output according to user-defined control parameters.

User Interface

In the designed system, an OLED LCD display was used for visualization purposes, a push-button was included to change the control mode, and a potentiometer was used to adjust the reference variable. Additionally, the required reference input voltage (V_i) for adjustment can also be applied externally and directly to the analog input. To control the output according to the firing angle, the ADC0 analog input of the microcontroller with 10-bit resolution was utilized. Figure 8 (a) shows the variation in firing angle depending on the voltage V_i applied to the analog input. To prevent noise interference on the analog input, a lower threshold voltage of 0.2 V was implemented. For input voltages between 0.2 V and 2.0 V, the firing angle was adjusted within the range of 0° to 180°, with a sensitivity of 10 mV. Similarly, an upper threshold voltage of 2.0 V was defined to ensure that the firing angle could not exceed 180°.

Figure 8 (b) zooms in the OLED screen. The screen provides real-time information on the active power control mode (firing angle or integral cycle), the set firing angle, trigger delay time, desired output voltage (Vout), and number of cycles applied to the load. According to the illustrated screen, the system is set to Firing angle Control mode, the firing angle is configured at 90°, the corresponding trigger delay time is 5000 s, thus, 50% of the supply signal is applied to the output. This user interface allows real-time monitoring and configuration of the system's power control parameters, providing both flexibility and operational transparency.

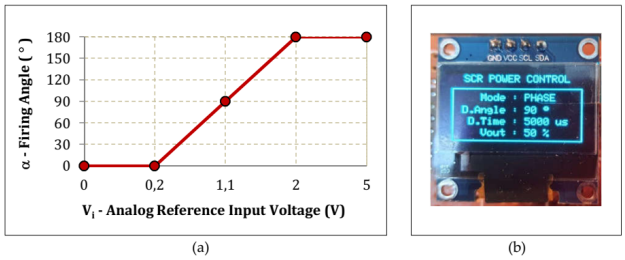

Figure 8 (a) Firing angle variation relative to the Vi analog reference input voltage (b) Zoomed user screen

EXPERIMENTAL RESULTS AND DISCUSSION

For the purpose of evaluating the performance of the designed system, the experimental setup shown in Figure 9 was constructed. In the setup, a Fluke 199C digital oscilloscope with a 200 MHz bandwidth and 2.5 GS/s sampling rate was used for signal measurements and waveform acquisitions. In addition, a True RMS digital multimeter was utilized to measure current and voltage values in order to determine the power delivered to the load. During the experimental studies, resistive loads of 60 Ω, 120 Ω, 180 Ω,

and 240 Ω (each rated at 700 W) were employed. Furthermore, a 220 V, 42 W incandescent bulb was used as an application-specific load to demonstrate the system's operational characteristics.

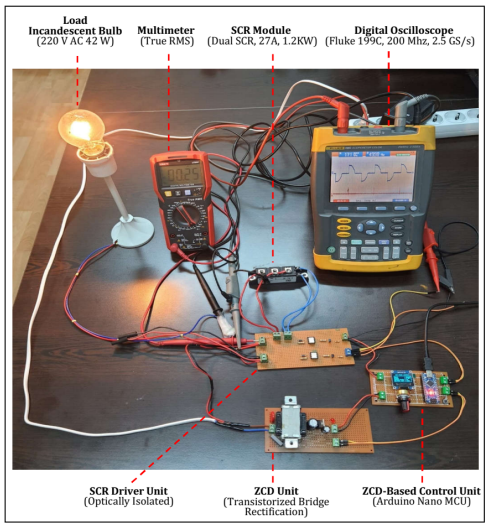

Figure 9 Experimental setup

In the experimental study, the ZCD and SCR triggering signals were first examined. Figure 10 shows the ZCD signal and the corresponding SCR triggering signals obtained from the system in relation to the supply signal. In the microcontroller-based system, both the rising zero-crossing point and the falling zero-crossing point of the supply signal can be accurately detected using the ZCD signal. Depending on the system configuration, triggering pulses can be generated either simultaneously or independently for the rising and falling zero-crossing points. This allows the system to perform triggering selectively for only the positive alternation, only the negative alternation, or both positive and negative alternations of the AC supply signal, depending on the desired operation mode.

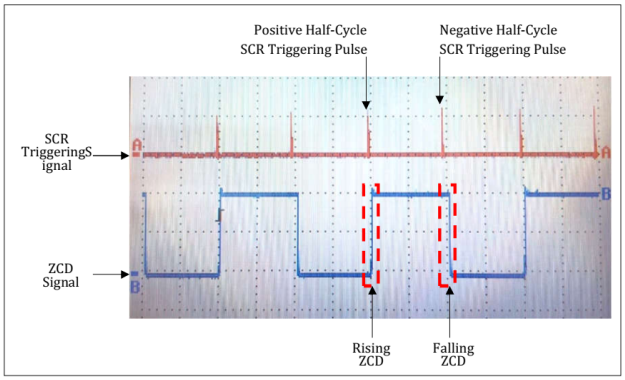

Figure 10 ZCD and SCR triggering signals relative to the supply signal

Figure 11 illustrates the positive and negative triggering regions on the output signal obtained using the SCR triggering signals when the firing angle is set to 90°.Since the firing angle is 90°, the SCR triggering for both alternations is performed after a delay time (td) of 5 ms for each half-cycle.

At the next stage of the experimental study, the triggering behavior of the SCR module was analyzed with respect to variations in the firing angle (). For this purpose, resistive loads ranging from

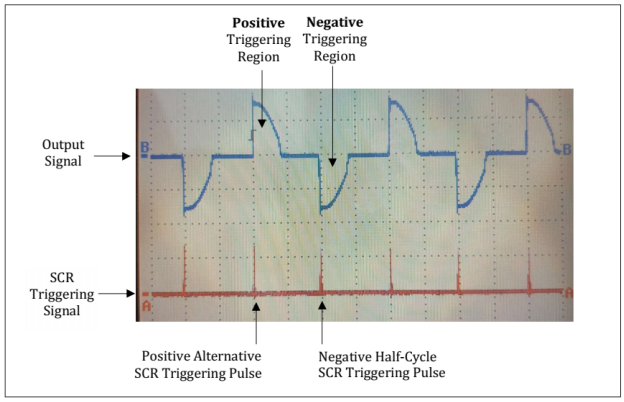

Figure 11 Positive and negative triggering regions on the output signal at the firing angle 90°

60 Ω to 240 Ω, each rated at 700 W, were connected to the SCR module. Depending on the firing angle variation between 0° and 180°, the SCR module was triggered after the corresponding delay times (td) for both alternations of the supply signal. Consequently, the AC voltage (V_{rms}) and current (I_{rms}) values across the load were measured and recorded, as presented in Table 1. Figure 12 shows that as the firing angle increases, the voltage applied to the load decreases. When = 0°, the source current is directly transferred to the output, whereas at = 180°, the output voltage drops to 0 V. Figure 13 presents the variation of the apparent power (S) calculated from the measured voltage and current values across the load. It is observed that as the firing angle increases, the apparent power on the load gradually decreases, reaching 0 VA when = 180°.

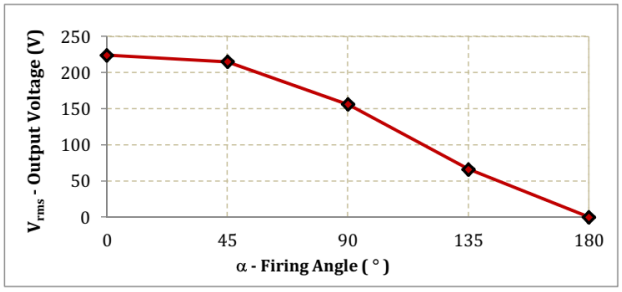

Figure 12 Variation of Vrms output voltage with respect to firing angle

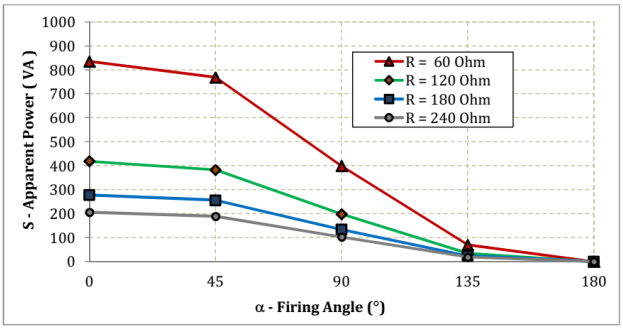

Figure 13 Variation of apparent power delivered to different loads with respect to firing angle

Table 1 Variation of electrical parameters for different resistive loads under SCR triggering

α (°)	t_d (μs)	$R_L = 60\,\Omega$			$R_L = 120\,\Omega$			$R_L = 180\,\Omega$			$R_L = 240\,\Omega$		
		V_{rms} (V)	I_{rms} (A)	S (VA)	V_{rms}	I_{rms}	S	V_{rms}	I_{rms}	S	V_{rms}	I_{rms}	S
0	0	224	3.73	835.52	224	1.87	418.88	224	1.24	277.76	224	0.92	206.08
45	2500	215	3.58	769.70	215	1.78	382.70	215	1.19	255.85	215	0.88	189.20
90	5000	156	2.56	399.36	156	1.27	198.12	156	0.86	134.16	156	0.66	102.96
135	7500	66	1.06	69.96	66	0.53	34.98	66	0.36	23.76	66	0.29	19.14
180	10000	0	0	0	0	0	0	0	0	0	0	0	0

In the last stage of the experimental study, which focuses on the practical application of the system, the triggering of the SCR module and the performance of an incandescent bulb were analyzed in relation to changes in the firing angle (). For this purpose, a 220 V, 42 W AC incandescent bulb was used as the load in the system. Accordingly, depending on the firing angle variation between 0° and 180°, the SCR module was triggered following the corresponding delay time (td), and the resulting V_{rms} and I_{rms} values across the lamp were measured and given in Table 2. Figure 14 shows that as the firing angle increases, the voltage applied to the load decreases. When = 0°, the source voltage is directly transferred to the output, whereas at = 180°, the source voltage becomes 0 V. Figure 15 presents the variation of the apparent power (S) calculated from the measured current and voltage values as a function of the firing angle. It is observed that the maximum apparent power on the load occurs at = 45°, at which point the incandescent bulb produces its maximum illumination, which is also clearly visible during the experiment.

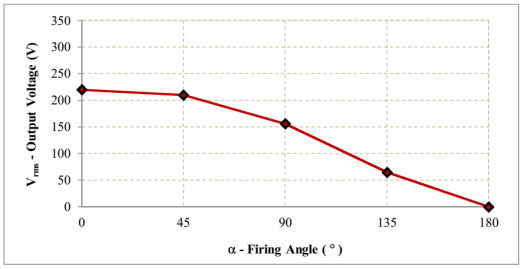

Figure 14 Variation of output RMS voltage (Vrms) applied to the incandescent bulb with respect to firing angle

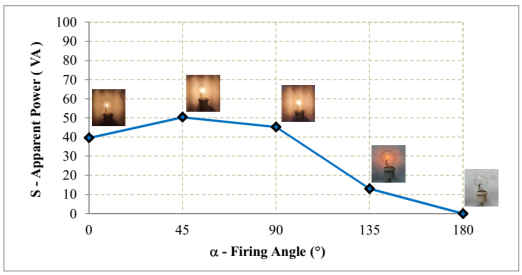

Figure 15 Variation of apparent power delivered to the incandescent bulb with respect to firing angle

For different firing angle () values of 0°, 45°, 90°, 135°, and 180°, the corresponding SCR triggering signals, output waveforms, control unit display screenshots, and the illumination levels of the incandescent bulb used as the load are shown in Figure 16 (a) through (d), respectively. According to these firing angle values, the corresponding triggering delay times (td) are 0 s, 2500 s, 5000 s, 7500 s, and 10000 s, respectively.

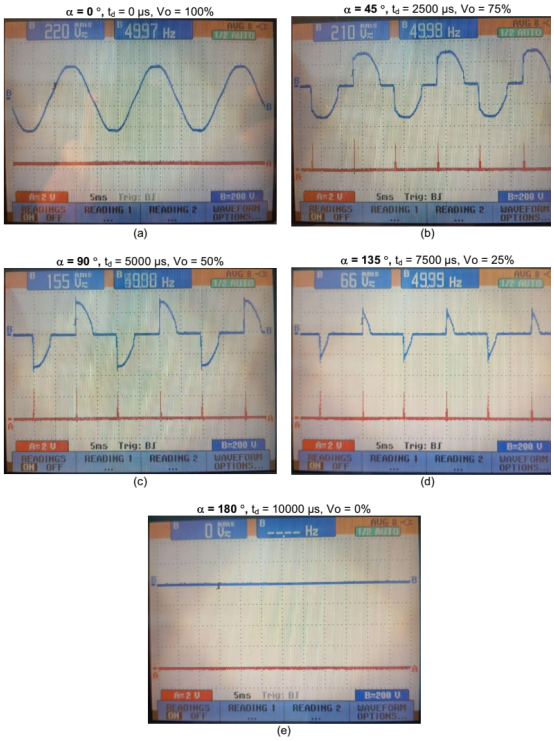

Figure 16 SCR triggering and output signals as a function of various firing angle values between 0° and 180°

Table 2 Electrical parameters of the incandescent bulb (220 V, 42 W) under SCR firing angle control

α (°)	t_d (μs)	V_{rms} (V)	I_{rms} (A)	S (VA)
0	0	220	0.18	39.60
45	2500	210	0.24	50.40
90	5000	156	0.29	45.24
135	7500	65	0.20	13.00
180	10000	0	0	0

CONCLUSION

In this study, the hardware and software of an embedded system of a single-phase microcontroller-based SCR power control device was developed to achieve fast and efficient power control for industrial applications. Using the ZCD method, the system enables bidirectional triggering of two anti-parallel connected SCRs after a delay time corresponding to the desired firing angle, thereby controlling the power applied to the load. In the designed system, firing angle control of the load is performed through the microcontroller's analog input via the SCR module. To prevent noise interference on the analog input, lower and upper threshold voltages were defined for the 10-bit resolution analog input of the microcontroller. By applying an input voltage between 0.2 V and 2.0 V, the corresponding firing angle () is adjusted within the range of 0° to 180°, with a precision of 10 mV.

To evaluate the performance of the designed system, an experimental setup was established in which the current and voltage measurements of the control and power circuits, as well as the corresponding signal waveforms, could be analyzed. In the experimental study, for a mains frequency of 50 Hz, the SCR triggering delay time (td) was adjusted between 0 and 10 ms corresponding to firing angle () variations from 0° to 180°, thereby enabling control of the power applied to the load between 0% and 100%. Within the scope of the application, a 220 V, 42 W AC incandescent bulb was employed as the load. By driving the lamp according to the firing angle control based on the ZCD method, different power levels were delivered to the load.

It was observed that although the firing angle varied linearly between 0° and 180°, the applied power did not change linearly, resulting in a nonlinear relationship between the firing angle and the illumination level of the incandescent bulb. Notably, the maximum perceived illumination on the lamp was observed at a firing angle of 45°. Unlike theoretical models that predict a monotonic decrease in power and illumination, these experimental findings highlight the importance of empirical validation. Whether this observed peak at intermediate angles originates from the inherent dynamic nature of the load, the impact of high-order harmonic distortion on measurement instrumentation, or potential measurement limitations remains a subject for further investigation. Future studies should aim to clarify these factors to enhance the precision of diagnostic accuracy in phase-controlled systems.

As a result, it has been demonstrated that the developed power control device can achieve fast and stable power regulation between 0% and 100% in industrial applications such as lighting and heating. In future, the functionality of the system can be further expanded by implementing additional software modules such as integral cycle control, on/off control, and soft-start operation, in addition to the existing firing angle control. These enhancements would significantly broaden the applicability of the device to a wide range of industrial environments involving resistive, inductive, and capacitive loads, thereby improving its adaptability, energy efficiency, and operational flexibility.

Ethical standard

The authors have no relevant financial or non-financial interests to disclose.

Availability of data and material

The data that support the findings of this study are available from the corresponding author upon reasonable request.

Conflicts of interest

The authors declare that there is no conflict of interest regarding the publication of this paper.

LITERATURE CITED

Akyasan, M. and U. Hasirci, 2016 Farkli sifir gecis algilama devrelerinin deneysel performansinin incelenmesi. Ileri Teknoloji Bilimleri Dergisi **5**.

Al-Baihani, H. H., S. Eskander, M. A. Elsayess, E. Gouda, M. Ammar, *et al.*, 2021 Simulation and experimental modeling of inverter triggering circuits using zero-crossing detector (zcd) based on microcontroller. Mansoura Engineering Journal **46**: 1–10.

Al-Mawsawi, S. A., N. Allaith, H. Qassim, and S. Dhiya, 2012 An accurate formula for the firing angle of the phase angle control in terms of the duty cycle of the integral cycle control. Journal of Automation and Systems Engineering .

Ashraf, N., T. Izhar, G. Abbas, A. B. Awan, A. S. Alghamdi, *et al.*, 2020 A new single-phase direct frequency controller having reduced switching count without zero-crossing detector for induction heating system. Electronics **9**: 430.

Bose, B. K., 2020 *Power Electronics and Motor Drives: Advances and Trends*. Academic Press, second edition.

Hart, D. W., 2011 *Power Electronics*. McGraw-Hill Education.

International Energy Agency, 2023 World energy outlook 2023.

Kurak, E. and V. Erdemir, 2013 Design and implementation of scr trigger circuit using microcontrollers. Electronic Journal of Vocational Colleges **3**: 104–109.

Mauriac, C., Y. Raingeaud, J. Baillou, L. Gonthier, and R. Pezzani, 2004 Thyristors and triacs control by a high frequency sine signal. In *IEEE International Symposium on Industrial Electronics*, volume 2, pp. 1029–1033, IEEE.

Rashid, M. H., 2014 *Power Electronics: Devices, Circuits, and Applications*. Pearson, fourth edition.

Rustemli, S. and E. Agrali, 2023 Computer based speed control application for universal motor. MANAS Journal of Engineering **11**: 112–118.

Texas Instruments, 2022 Zero-cross switching for solid-state relays reference design. Technical Report TIDA-050058, Texas Instruments.

Yurtcu, A., 2021 *Sifir Gecis Tabanli Elektronik Salter ve Kacak Akim Roleli Hibrit Bir Sistemin Gelistirilmesi*. Ph.D. thesis, Istanbul Gedik University.

Zheng, G. L. and Z. F. Zhang, 2012 A novel intelligent load control switch based on dynamic compensation method for current zero-crossing point. Advanced Materials Research **433**: 4717–4724.

How to cite this article: Karaduman, D. K., Gencol, K., and Dislitas, S. Nonlinear Effects of Zero-Crossing Detection Based Firing Angle Power Control on Lighting Performance. *Chaos and Fractals*, 3(1), 54-60, 2026.

Licensing Policy: The published articles in CHF are licensed under a Creative Commons Attribution-NonCommercial 4.0 International License.

ADBA Chaos and Fractals
Cutting-Edge Scientific Solutions

e-ISSN: 3023-8951
RESEARCH ARTICLE
Vol.3 / No.1 / 2026 / pp.61-64
https://doi.org/10.69882/adba.chf.2026019

An Investigation into the Interpretation of Pi (π) as the Arithmetic Mean of the Golden Ratio (ϕ) and the Feigenbaum Constant (δ)

İhsan Pehlivan[*,1], **Selahattin Bulut**[*,α,2] **and Emin Güney**[β,3]

[*]Sakarya University of Applied Sciences, Faculty of Technology, Deparment of Electrical and Electronics Engineering, Sakarya, Türkiye, [α]Sakarya University of Applied Sciences Graduate Education Institute, Sakarya, Türkiye, [β]Sakarya University of Applied Sciences, Faculty of Technology, Department of Computer Engineering, Sakarya, Türkiye.

ABSTRACT This study comprehensively examines the numerical proximity of the arithmetic mean of the golden ratio (ϕ) and the Feigenbaum constant (δ) to the number π, the theoretical mechanisms underlying this relationship, and its epistemological value. Although these three fundamental constants, situated at the intersection of mathematics and theoretical physics, are generally treated as elements of independent disciplines, this research unearths a unique structural bridge expressed through the formulation $\pi = (\phi + \delta)/2$. Numerical analyses prove that the relationship in question can be evaluated within the class of high-precision mathematical approximations, with a notably low relative error margin of approximately $\%0.064$. Within the scope of the study, the fact that the arithmetic balance between the "most irrational number" ϕ, representing maximum dynamic stability, and the universal scaling factor δ, defining the critical threshold at which systems drift into chaos, corresponds to the number π the foundation of periodic cycles is discussed within the framework of the "geometric balance between chaos and order" hypothesis. Whether this numerical pattern is a coincidental numerological coincidence or a yet to be discovered deep topological necessity is analyzed in the context of dynamical systems theory and Euler's identity. In conclusion, by presenting a simple and elegant equation that has gone unnoticed in the half century since the discovery of the Feigenbaum constant, this article raises new epistemological questions regarding the nature of fundamental constants and offers an interdisciplinary perspective on understanding the hidden geometry of nature.

KEYWORDS
Chaos
Mathematical constants
Transcendental numbers
Pi (π)
Golden ratio (ϕ)
Feigenbaum constant (δ)

INTRODUCTION

The mathematical and physical constants that define the fundamental workings of the universe point toward a hidden geometry lying deep within nature and the dynamic order beneath chaotic systems. Fundamental constants, situated at the intersection of mathematics and theoretical physics, are considered numerical signatures representing deep structural rules in the fabric of the universe. The number π, the cornerstone of Euclidean geometry; the golden ratio (ϕ), at the heart of growth dynamics and aesthetics; and the Feigenbaum constant (δ), which defines universal scaling in the processes of transition to chaos in non-linear systems despite being discovered in different periods of history converge unexpectedly within modern dynamical systems theory (Smith 2013; Freinacht 2022).

The Number Pi (π): The Constant of Periodicity and Rotational Symmetry

The number π, defined as the ratio of a circle's circumference to its diameter, is one of the oldest and most well-known mathematical constants in history. With a numerical value of 3.1415926535..., this constant is a transcendental and irrational number, serving as a fundamental determinant of periodic processes not only in circular geometry but also in wave mechanics, quantum physics, and probability theory (Borwein 2000; Agarwal et al. 2013; Eymard and Lafon 2004). Also referred to as "Archimedes' constant" in the literature, π plays a central role in the mathematical expression of harmonic oscillations (for example, the sine and cosine functions). In modern physical theories, π is viewed as a reflection of the isotropic nature of space and rotational symmetry (Singh 2008). Its transcendental and irrational nature causes the decimal digits

Manuscript received: 12 November 2025,
Revised: 25 January 2026,
Accepted: 25 January 2026.

[1]ipehlivan@subu.edu.tr (**Corresponding author**)
[2]selahattinbulut@subu.edu.tr
[3]eminguney@subu.edu.tr

of Pi to extend infinitely without ever repeating. From geometry to trigonometry, and from cosmology to statistics, Pi is the fundamental key that expresses the symmetry and periodicity of the universe.

The Golden Ratio (ϕ): Recursive Growth and Dynamic Balance

The golden ratio is an algebraic irrational number expressed by the value:

$$\phi = \frac{1+\sqrt{5}}{2} \approx 1.6180339887...$$

Emerging as the limit of the ratio of successive terms in the Fibonacci sequence, this number is observed in spiral structures in nature, plant phyllotaxis, and the geometry of galactic arms.From the perspective of dynamical systems, ϕ is considered the "least rational" or "most irrational" number (Kak 2010; Ho et al. 2015; Akhtaruzzaman and Shafie 2011; Dunlap 1997). This definition stems from the fact that the continued fraction expansion of the golden ratio consists solely of ones:

$$\phi = 1 + \frac{1}{1 + \frac{1}{1 + \frac{1}{1+...}}}$$

By virtue of this property, ϕ represents the state in which a dynamical system is most resistant to chaotic resonances; for it is the value that is most difficult to approximate with rational numbers (Dunlap 1997). The Golden Ratio is an algebraic irrational mathematical constant accepted as an indicator of aesthetic and functional perfection in nature, art, and architecture. From biological growth to crystallography, the golden ratio serves as the coefficient of "optimal balance" across many fields. Defined algebraically as the positive root of the equation $x^2 - x - 1 = 0$, ϕ also emerges as the limit of the ratio of successive numbers in the Fibonacci sequence. The universality of the Golden Ratio has been documented in a vast literature ranging from biology to astrophysics.

The Feigenbaum Constant (δ): The Universal Law of Transition to Chaos

Discovered by Mitchell Feigenbaum in 1975, the mathematical irrational constant $\delta \approx 4.6692016091...$ defines the ratio of intervals in the period doubling bifurcations of non-linear chaotic systems (Smith 2013; Freinacht 2022). In his studies on quadratic maps (for example, the logistic map), Feigenbaum demonstrated that the ratio of the difference between parameter values where a system's stable cycle doubles to the next doubling interval approaches a constant value (δ) (Smith 2013). The truly revolutionary aspect of this discovery is that this ratio remains the same regardless of the system's details (whether the map is a sine function or a polynomial) (Smith 2013). The Feigenbaum constant expresses the "scaling law" in the transition from a regular structure to a chaotic structure in complex processes in the physical world, such as turbulence, cardiac arrhythmias, and population dynamics (Freinacht 2022).

NEW HIDDEN GEOMETRY BETWEEN THE GOLDEN RATIO(ϕ), FEIGENBAUM CONSTANT(δ), AND π

In this section, a hidden geometry discovered between the golden ratio, the Feigenbaum constant, and the number pi, which is not found in the literature, is presented. The fundamental claim is the surprising degree of proximity of the arithmetic mean of the golden ratio (ϕ) and the Feigenbaum constant (δ) to the number (π). The geometry discovered between the golden ratio, the Feigenbaum constant, and the number pi is formulated as shown in Table 1 and Equation 1;

Table 1 The geometry discovered between the golden ratio(ϕ), the Feigenbaum constant(δ), and the number pi(π)

π	$\frac{\phi+\delta}{2}$
3.14159265	3.14**361779**

$$\pi \approx \frac{\phi+\delta}{2} \tag{1}$$

Table 2 Numerical Values and Definitions of the Constants

Variable	Numerical Value	Formula / Definition
Golden Ratio (ϕ)	1.61803398	$\frac{1+\sqrt{5}}{2}$
Feigenbaum Constant (δ)	4.66920160	$\lim_{n\to\infty} \frac{\mu_{n+2}-\mu_{n+1}}{\mu_{n+1}-\mu_n}$
Number π	3.14159265	$\frac{\text{Circle's Circumference}}{\text{Circle's Diameter}}$
$(\phi+\delta)/2$	3.14361779	Arithmetic Mean
Absolute Difference	0.00202514	Quality of convergence

If a numerical comparison and error margin analysis are performed based on Table 2, it is observed from the results of calculations carried out to 8 decimal places that the absolute difference is at the level of 0.002025. This difference corresponds to a relative error of approximately %0.064. In scientific literature, proximity at this level is generally classified as "high precision". The numerical accuracy and theoretical validity of this correlation should be examined through the mathematical concept of "approximation" (Lange 2010). Is this high-precision numerical proximity merely a "numerological coincidence" with no meaningful connection, or is it a reflection of a yet to be discovered deep mathematical or physical principle? Determining the mathematical nature and the place in science of these three universal constants is critically important for understanding whether the relationship between them is accidental or structural. Each of these constants is defined as an "invariant" within its own discipline and persists regardless of the scale of the system.In the history of physics, the search for numerical relationships such as Bode's Law that are seemingly meaningful but lack a fundamental theoretical basis has a long history. Given the countless existing mathematical and physical constants, the probability of finding such proximities by bringing these constants together in an infinite number of algebraic combinations is statistically expected. This argument suggests that the presented relationship might be nothing more than a random pattern extracted from a vast sea of probabilities.

On the other hand, considering how fundamental and universal each of these three constants is in their respective fields (geometry, growth/ratio, and chaos/universality), the probability that

this simple and elegant relationship between them is a mere coincidence diminishes significantly. Perhaps these constants are different faces of a more fundamental mathematical structure that unifies them under a single umbrella. This unexpected bridge between geometry, algebra, and dynamical systems may serve as a vital clue regarding the fundamental workings of nature at its most basic level. Some studies in the literature investigating the relationships between transcendental numbers and mathematical constants argue that a deeper topological reason may underlie such relationships, given that the constants under examination are the limit values of recursive processes (Smith 2013). Similarly, this study evaluates the possibility that a profound topological connection exists behind the striking numerical proximity of the arithmetic mean of the golden ratio (ϕ) and the Feigenbaum constant (δ) to the number π.

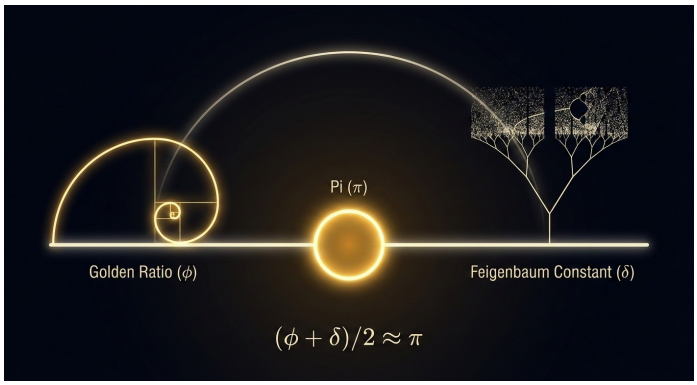

Figure 1 The bridge at the intersection of order (ϕ) and chaos (δ): π.

Figure 1 symbolizes π as the geometric equilibrium between the order of the Golden Ratio (ϕ) and the chaos of the Feigenbaum constant (δ). It illustrates π as a structural bridge unifying these two fundamental dynamics of nature.

It can be argued that these three numbers did not come together by chance, but rather represent a geometry of the transition between chaos and order. The golden ratio is the most irrational number. In dynamical systems (for example, in planetary orbits or KAM theory), it represents the point where a system is most resistant to chaos, that is, where it remains most orderly. The Feigenbaum constant is the universal scaling factor at the point where order completely breaks down and transitions into chaos ("period doubling"). The number π is the foundation of periodic cycles, namely circular motion. The equality Equation 1 may be whispering the following: "The balance point between maximum order (ϕ) and the onset of complete chaos (δ) is the fundamental periodic cycle (π)". By utilizing the equation, the existence of the relationship shown in Table 3 can also be demonstrated.

Table 3 Proximity in the complex plane

$e^{i \cdot 2\pi}$	$e^{i(\phi+\delta)}$
$1.0 + 0.0i$	$0.999991 + 0.00405i$

As can be seen from Table 3, due to the fact that the sum of two very special numbers, such as the golden ratio and the Feigenbaum constant, is nearly equal to the universal value of 2π, it is observed to satisfy Euler's identity in a surprising manner (with an error on the order of approximately 10^{-6}). This new correlation, which extracts order out of chaos, has revealed that the value 2π the key to circular geometry can be approximately derived from the sum of δ, the universal constant of chaos, and ϕ, the constant of growth.

RESULTS AND DISCUSSION

In this article, an attempt has been made to establish a theoretical bridge concerning how a connection can be formed between π, ϕ, and δ. At the focal point of the study lies the approximate numerical correlation Equation 1, which unifies three fundamental mathematical constants. The high numerical accuracy of this observation has been demonstrated, while the inherent probability of coincidence in such relationships has also been emphasized. It is considered that this numerical relationship, bringing together three constants from seemingly unrelated branches of mathematics, such as geometry (π), universal growth dynamics and aesthetics (ϕ), and the processes of transition to chaos (δ), possesses significant potential for investigation in terms of nature, physics, and mathematics. Such research supports the idea that fundamental constants are not independent but may be interconnected by a deeper mathematical logic. This article has investigated the deep and unexpected connections that may exist between fundamental constants from different fields of mathematics through a critical perspective. Although the Feigenbaum constant has been known for 50 years, the fact that the approximate value of π can be obtained by taking its arithmetic mean with the golden ratio has not been identified by any researcher until now.

CONCLUSION

Some significant contributions of this study include: establishing a bridge between seemingly independent mathematical constants, demonstrating a simple methodology for investigating such apparent patterns, and highlighting the profound epistemological challenges of distinguishing pattern from coincidence. It is evaluated that the hypothesis presented by this simple, elegant, and conspicuous equation may serve as a tool for "intellectual provocation" in terms of raising new research questions regarding the nature of fundamental constants. Systematically examining whether other simple and elegant relationships, like the one proposed in this study, exist between other mathematical and physical constants and discovering potential connections will reduce the probability of the presented hypothesis being a coincidence. While the speculative nature of the ideas presented in the article is acknowledged, it is believed that such interdisciplinary and bold explorations are an absolute necessity for pushing the boundaries of science and understanding the fundamental workings of the universe at its most basic level. It is further evaluated that other correlations to be discovered among universal constants in different disciplines of mathematics and physics may serve as the key to future major scientific breakthroughs.

Ethical standard

The authors have no relevant financial or non-financial interests to disclose.

Availability of data and material

Not applicable.

Conflicts of interest

The authors declare that there is no conflict of interest regarding the publication of this paper.

LITERATURE CITED

Agarwal, R. P., H. Agarwal and S. K. Sen, 2013 Birth, growth and computation of pi to ten trillion digits. Advances in difference equations **2013**: 100.

Akhtaruzzaman, M. and A. A. Shafie, 2011 Geometrical substantiation of Phi, the golden ratio and the baroque of nature, architecture, design and engineering. International Journal of Arts **1**: 1–22.

Borwein, P., 2000 The amazing number Pi. Nieuw Archief Voor Wiskunde **1**: 254–258.

Dunlap, R. A., 1997 The golden ratio and Fibonacci numbers. World Scientific.

Eymard, P. and J. P. Lafon, 2004 The Number π. American Mathematical Soc.

Freinacht, H. (2022). Is Metamodernism the Last Stage of Development? Chaos Theory Might Hold the Answer. *Metamoderna*. https://metamoderna.org/is-metamodernism-the-last-stage-of-development-chaos-theory-might-hold-the-answer/

Ho, M.-W., M. El Naschie and G. Vitiello, 2015 Is spacetime fractal and quantum coherent in the golden mean. Global Journal of Science Frontier Research **15**: 61–80.

Kak, S., 2010 The golden mean and the physics of aesthetics. Ancient Indian leaps into mathematics, Springer: 111–119.

Lange, M., 2010 What are mathematical coincidences (and why does it matter)?. Mind **119**: 307–340.

Singh, R. B., 2008 Introduction to modern physics. New Age International.

Smith, R. D., 2013 Period doubling, information entropy, and estimates for Feigenbaum's constants. International Journal of Bifurcation and Chaos **23**: 1350190.

How to cite this article: Pehlivan, İ., Bulut , S., and Güney, E. An Investigation into the Interpretation of Pi (π) as the Arithmetic Mean of the Golden Ratio (ϕ) and the Feigenbaum Constant (δ). *Chaos and Fractals*, 3(1), 61-64, 2026.

Licensing Policy: The published articles in CHF are licensed under a Creative Commons Attribution-NonCommercial 4.0 International License.